UNIVERSIDAD DE CHILE
FACULTAD DE CIENCIAS FÍSICAS Y MATEMÁTICAS
DEPARTAMENTO DE INGENIERÍA ELÉCTRICA

# SOLID PROPELLANT ENGINE ARRANGEMENT FOR THE MOON SOFT LANDING PROBLEM: STUDY OF ATTITUDE REQUIREMENTS AND DESIGN OF THE TRAJECTORY CONTROL SYSTEM

TESIS PARA OPTAR AL GRADO DE DOCTOR EN INGENIERÍA ELÉCTRICA

ELÍAS ALBERTO OBREQUE SEPÚLVEDA

PROFESOR GUÍA:
MARCOS ANDRÉS DÍAZ QUEZADA

MIEMBROS DE LA COMISIÓN:
SHINICHI NAKASUKA
RODRIGO CASSINELI PALHARINI
JORGE SILVA SÁNCHEZ

Este trabajo ha sido parcialmente financiado por CONICYT-PFCHA/Doctorado Nacional/2019-21190990

SANTIAGO DE CHILE
2024

RESUMEN DE LA TESIS PARA OPTAR AL GRADO DE
DOCTOR EN INGENIERÍA ELÉCTRICA
AUTOR: ELÍAS ALBERTO OBREQUE SEPÚLVEDA
FECHA: 2024
PROFESOR GUÍA: DR. MARCOS ANDRÉS DÍAZ QUEZADA

# ARREGLO DE MOTORES DE PROPELENTE SÓLIDO PARA EL PROBLEMA DE ATERRIZAJE SUAVE EN LA LUNA: ESTUDIO DE LOS REQUISITOS DE ACTITUD Y DISEÑO DEL SISTEMA DE CONTROL DE TRAYECTORIA

Este trabajo presenta el diseño de un sistema inteligente de control para el problema del aterrizaje suave en la Luna utilizando motores de propulsión sólida (SPM). Aunque los SPM tienen problemas de controlabilidad y el hecho de que no se pueden apagar, se caracterizan por su confiabilidad, simplicidad y rentabilidad. En consecuencia, nuestra principal contribución es abordar estos inconvenientes mediante la formulación de un problema de optimización de aterrizaje bidimensional utilizando un arreglo de SPM. El arreglo se estudia sobre una plataforma CubeSat con diferentes números de motores y para tres tipos de sección transversal del grano propulsor (PGCS). Los parámetros de los motores y control fueron optimizados inicialmente mediante un algoritmo genético (GA) debido a la no linealidad del problema y las incertidumbres de las variables de estado. Se analizan dos enfoques de diseño para el control, donde el diseño robusto basado en las incertidumbres de las variables muestra el mejor desempeño. Se utilizaron simulaciones de Monte Carlo para demostrar la eficacia del diseño robusto. Esto disminuye la velocidad de impacto (IV) a medida que aumenta el número de motores, aterrizando a 2,97 m/s utilizando una disposición de 10 motores con un PGCS regresivo. Finalmente, se presentan los requisitos del sistema de control de actitud para mantener la estabilidad direccional del empuje.

ABSTRACT OF THE THESIS FOR THE DEGREE OF
DOCTOR IN ELECTRICAL ENGINEERING
AUTHOR: ELÍAS ALBERTO OBREQUE SEPÚLVEDA
DATE: 2024
ADVISOR: DR. MARCOS ANDRÉS DÍAZ QUEZADA

# SOLID PROPELLANT ENGINE ARRANGEMENT FOR THE MOON SOFT LANDING PROBLEM: STUDY OF ATTITUDE REQUIREMENTS AND DESIGN OF THE TRAJECTORY CONTROL SYSTEM

This work presents the design of an intelligent control system for the problem of soft landing on the Moon using solid propellant engines (SPE). Although SPEs have controllability problems and the fact that they cannot be turned off, they are characterized by their reliability, simplicity, and cost-effectiveness. Consequently, our main contribution is to address these drawbacks by formulating a two-dimensional landing optimization problem using an array of SPEs. The arrangement is studied on a CubeSat platform with different numbers of engines and for three types of propellant grain cross-section (PGCS). The engine and control parameters were initially optimized by a genetic algorithm (GA) due to the non-linearity of the problem and the uncertainties of the state variables. Two design approaches for control are analyzed, where the robust design based on the uncertainties of the variables shows the best performance. Monte Carlo simulations were used to demonstrate the effectiveness of the robust design. This decreases the impact velocity (IV) as the number of engines increases, landing at 2.97 m/s using an arrangement of 10 engines with a regressive PGCS. Finally, the requirements of the attitude control system to maintain the directional stability of the thrust are presented.

*A Jesucristo, por enseñarme un universo lleno de misterios.*
*A mi esposa Victoria, por su incondicional ayuda y paciencia.*
*A mi hijo Daniel, por hacerme sentir como un niño otra vez.*
*A mi padre, por acompañarme en los momentos importantes de mi vida.*
*A mi madre, por enseñarme a soñar,*
*y a mi familia y amigos.*

# Acknowledgments

First, I want to thank Dr. Marcos Díaz for his advice and encouragement to think outside of traditional frameworks, and the Space and Planetary Exploration Laboratory (SPEL) that he directs. Having actively participated in the SUCHAI 2&3 and PlantSat projects, I was able to carry out this research thanks to the opportunities, tools and knowledge provided in spatial matters.

I also want to thank ANID for funding my Thesis under the grant CONICYT-PFCHA/ Doctorado Nacional/2019-21190990. On the other hand, this work has been funded by the grants: FONDECYT Regular 1221907, FONDECYT Regular 1211695, the Air Force Office of Scientific Research (AFOSR) under award number FA9550-18-1-0249.

I am thankful for the SEELA students exchange program, which allowed me to do an internship at the University of Tokyo. Through Professor Shinichi Nakasuka, and the diligence of the team at the Intelligent Space Systems Laboratory (ISSL), I was able to learn about dynamic simulations and attitude estimation & control systems.

I want to thank Professor Aroh Barjatya, who received me at his laboratory at the Embry-Riddle Aeronautical University to do an internship. During the stay, and as a member of the SPEL commission, we finished the final details of CubeSat integration, magnetometer calibration, and testing for software initialization for the satellites SUCHAI 2, SUCHAI 3, and PlantSat.

Finally, to Jesus Christ and his salvation, to my wife Victoria and my son Daniel for their love, to my family and my friends. A special mention to Sofía Saldias,who kindly took care of my son Daniel so that I could advance my research; to Eliecer Leiva, for helping me get out of the routine by traveling to adventure; and to Carlos González and Camilo Rojas, who taught me the programming tools that today allow me to develop this work.

# Table of content

# List of Tables

# List of Figures

# Nomenclature

- **ACF**: Average Cost Function
- **ADCS**: Attitude Determination and Control System
- **ANN**: Artificial Neural Network
- **CDS**: CubeSat Design Specification
- **COTS**: Commercial off-the-shelf components
- **DCF**: Direct Cost Function
- **EA**: Evolutionary Algorithms
- **EC**: Evolutionary Computational
- **EDL**: Entry, Descent, and Landing
- **ESA**: European Space Agency
- **GA**: Genetic algorithm
- **HJB**: Hamilton-Jacobi-Bellman
- **JAXA**: Japan Aerospace Exploration Agency
- **JPL**: NASA Jet Propulsion Laboratory
- **NASA**: National Aeronautics and Space Administration
- **NLP**: Non-linear Programming
- **NRHO**: Near-Rectilinear Halo Orbit
- **OGC**: Optimal Guidance Calculation
- **PGCS**: Propellant Grain Cross Section
- **PMP**: Pontryagin's Minimum Principle

- **PSO**: Particle Swarm Optimization
- **PWM**: Pulse-Width Modulation
- **SPE**: Solid Propellant Engine
- **TPBVP**: Two-Point Boundary Value Problem

# 1. Introduction

## 1.1 Motivation

Throughout history, landing on a different celestial body than our planet has captured our imagination. The first to accomplish this feat was the lander of the Soviet Union's Luna program on February 3, 1966, named Luna 9. Luna 9 was the twelfth soft landing attempt by the Soviets; it was also the first to transmit photographs from the lunar surface. Subsequently, the lunar surface was reached by Surveyor-I, which was built by the National Aeronautics and Space Administration (NASA) and the Jet Propulsion Laboratory (JPL) on May 30, 1966. Unlike the modules of Soviet lunar landers, Surveyor was a lander with a large solid-propellant retro-rocket engine (comprising over 60% of the spacecraft's total mass) at the center [1]. Solid propellant engines (SPE) were used on many early exploration missions for landing and orbital maneuvers. However, the maneuvers began to require more precision and control for the new landing missions, which increased the challenges and control requirements. Under this scenario, the SPEs presented flight controllability issues, since they are not re-ignitable and have a thrust defined by the geometry of the propellant grain cross-section (PGCS) [2]. Consequently, in later space missions liquid fuels began to be used, which increased the costs of the mission and the technological requirements to be applied. To mitigate the costs of new missions, miniaturization has brought about the creation of small modules, which are taking a relevant role in exploration. And with the increase in computing power of new controllers, it creates the opportunity and need to revisit the use of solid propellants in space exploration.

Currently, the large-scale space exploration that is projected for the coming years makes us rethink the use of SPE in space missions. Maggi et al. [3] examine the opportunities that might arise using SPEs in future space activities, which can reduce its cost with a simple propulsion system that is characterized by reliable operation, easy handling, safe storability, and simplicity of design and development. In this context, SPEs should have a central role in space exploration in the short and medium-term future. Additionally, as mentioned by Okninski A. [4], the SPEs reduce the number of mechanical parts, such as valves, tanks, and electrical components for control, decreasing the complexity of operation required by the propulsion system (See Figure 1.1). Figure 1.1 presents results of a dedicated ESA study comparing liquid and solid propulsion for de-orbit-relative costs, mass budget differences due to required spacecraft velocity increase (delta-V) and expected reliability have been computed for different spacecraft sizes. As summarize on [5] and in Figure 1.1, Solid propellant is a promising technology to space development.

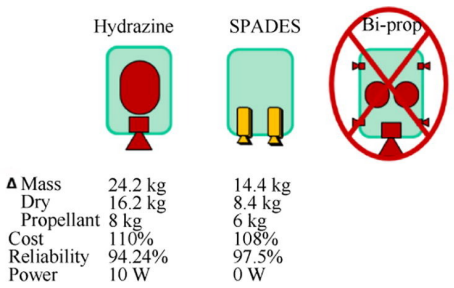


| | Hydrazine | SPADES |
|---|---|---|
| Δ Mass | 24.2 kg | 14.4 kg |
| Dry | 16.2 kg | 8.4 kg |
| Propellant | 8 kg | 6 kg |
| Cost | 110% | 108% |
| Reliability | 94.24% | 97.5% |
| Power | 10 W | 0 W |

(a) Results for LEO satellites below 200 kg of mass

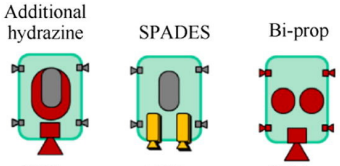


| | Additional hydrazine | SPADES | Bi-prop |
|---|---|---|---|
| Δ Mass | 328 kg | 165 kg | 272 kg |
| Dry | 168 kg | 59 kg | 196.6 kg |
| Propellant | 160 kg | 106 kg | 75.4 kg |
| Cost | 107% | 103% | 109% |
| Reliability | 94.24% | 97.5% | 97.49% |
| Power | 15 W | 0 W | 15 W |

(b) Results for LEO satellites between 1000 and 2000 kg of mass

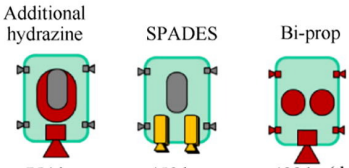


| | Additional hydrazine | SPADES | Bi-prop |
|---|---|---|---|
| Δ Mass | 754 kg | 450 kg | 488 kg (tbc) |
| Dry | 246 kg | 115 kg | 255 kg |
| Propellant | 508 kg | 335 kg | 233 kg |
| Cost | 107% | 106% | 112% |
| Reliability | 94.24% | 96.28% | 97.49% |
| Power | 60 W | 0 W | 30 W |

(b) Results for LEO satellites exceeding 2000 kg of mass

Figure 1.1: ESA Solid Propellant Autonomous DE-Orbit System (SPADES) study comparison regarding use of different chemical propulsion systems. For satellites of different mass scales, the required propellant mass, percentage cost, reliability and electrical power required are shown. Extracted from [4].

Chavers et al. [6] explain that every effort must be made to reduce the mass needed for the spacecraft in future exploration missions, and a low-weight module with solid-state propulsion could contribute to this reduction if the propulsion technology is small. Accompanied by the **technology miniaturization** and **advanced additive manufacturing**, this allows for the consideration of small rovers and landers (<100 kg), where each component must use a reduced amount of volume. This consideration returns to the initial philosophy presented by the Mars Pathfinder (MPF) mission: an economic small lander that used three SPEs simultaneously to generate braking thrust on Mars [7]. By then, the landing of the MPF module was not smooth, and it needed an airbag system for the small rover inside to survive the impact on the surface, which was to a velocity between 12.5 and 25 m/s.

Small landers and rovers present a different opportunity than the large spacecraft philosophy for exploration. The small spacecraft philosophy focuses on having many low-cost systems **A** rather than one expensive single system **B**. While System **B** exhibits

better performance, autonomy, and precision than small systems **A**, as demonstrated by the Mars Science Laboratory (MSL) and Phoenix missions [8], the low-cost systems **A** allows larger areas to be explored simultaneously. Otherwise, the simultaneous exploration is one of the focuses of recent space projects such as the Heracles mission by the European Space Agency (ESA) and the Artemis project by NASA. One of ESA's priorities is the *Deployment of geophysical instruments and the build-up a global geophysical network* [9]. In parallel, Artemis is prioritizing capabilities that support lunar resource analysis and prospecting to inform future human spaceflight objectives and includes activities for Commercial Lunar Payload Services [10]. On the other hand, Jamanca-Lino et al. [11] present the importance of exploring Ilmenite deposits to produce oxygen on the moon, which is crucial to obtaining water, and rocket fuel, and promoting commercial activities between the Earth and the Moon. Commercial activities, geophysical instrument networks, and research on space mining presented by the Chinese Lunar Exploration Program (CLEP), need to reduce the costs of the mission, presenting the motivation to investigate the effectiveness of using a small lander with SPEs for the soft-landing problem.

### 1.1.1 Challenge of SPEs in soft control

Despite the advantages mentioned above, SPEs have control problems to perform smooth movements during flight derived from uncertainties. Maggi et al. describes that the specific impulse of the solid propellant can vary by 10% of the estimated nominal value, without considering the uncertainties of the engine that add a transient noise. This value can be affected too by environmental conditions, corrosion, and burn erosion. But even having a smaller uncertainty in the specific impulse, the altitude and velocity of the lander also have uncertainties that affect the control of the ignition point in this type of engine. The uncertainties in these parameters are one of the main reasons (along with the fact that the propellant is not re-ignitable) why SPEs are not currently used for soft-landing.

Okninski A. [4] mentions some challenges for de-orbit control and which in this work are considered relevant for a soft landing process. The key points are:

- Limiting the inert mass of the system and minimising the necessary SPE size. Effect: use of high performance propellant and a high propellant mass fraction SPEs (efficient material selection - in particular **low-regression-rate** ablative insulation).

- Limitar el nivel de empuje para limitar las aceleraciones de la nave espacial durante el disparo del SRM; las aceleraciones máximas dependen del diseño de la nave espacial. Aceleraciones superiores a 1 g son aceptables para los CubeSats típicos y para muchos otros satélites pequeños sin paneles solares ni antenas plegables. Effect: very **low-burn-rate** propellant and an **end-burning** configuration of the SPE (especially for spacecraft with appendages), use of clusters of SPEs in case of high total impulse requirements.

Low burn rate and low thrust propellants should be sought, which is achieved with an End-Burning type configuration. Furthermore, the use of arrays or clusters reappears again, showing an increase in total impulse. However, little or no documentation exists on the control problems associated with thrusts applied outside the center of mass, a problem that appears with SPE arrangements. Therefore, to improve the use of SPE

in space maneuvers, this work propose that all the thrust required in the mission can be separated into a series of **independent** engines (clusters). Each engine in the array must have a lower thrust and active time than the complete engine, and is controlled by an independent control function. This property makes the propulsion system more controllable. However, the arrangement generates forces that are not collinear with the center of mass of the module, generating residual torques. These torques, which are not exactly predictable in direction and magnitude, must be counteracted by an internal control torque. On the other hand, the use of a CubeSat-type platform as a small lander is present as constraint, which are standardized satellites of low mass and small size [12]. To solve this nonlinearity problem, the use of a control system trained by evolutionary algorithms is proposed.

## 1.2 Hypothesis

This research is within the framework of resuming the use of SPEs in space missions in which soft controls are required. In particular, the work focuses on a promising use of SPEs with respect to soft landings of small modules. An ideal optimization case only requires a single motor to begin braking the module from a single position in space. But real life is not ideal. In this situation, a control function must be designed in a way that optimizes the landing trajectory including the main engine problems: Non-reignitable, specific impulse variation, ignition dead times, among others; and uncertainties in state parameters such as position and velocity.Therefore, the hypotheses that give rise to this research are the following.

**H1** The total thrust of a single SPE can be divided into multiple smaller and independent thrusts generated by an array of SPEs, increasing control system flexibility and accuracy for a landing scenario.

**H2** There is a control system capable of solving the soft landing problem with an SPE arrangement, and at the same time controlling the attitude of the module optimally with a rotational actuator such as reaction wheels (based on the ranges of the residual torques and the agility of the dynamic response).

**H3** Using the proposed control system and a CubeSat mass reference, it is possible to implement the SPE arrangement as a solution for modules based on 12U CubeSat platforms using a reaction wheel as the rotation actuator.

**H4** Using an evolutionary algorithm to optimize the robust control design, the SPE geometry can also be optimized based on references from a 12U Cubesat.

## 1.3 Objectives

### 1.3.1 General objectives

The general objective is to design a robust control system to use an SPE arrangement in the moon soft landing problem, considering the uncertainties of the environment and the

perturbations induced by each engine on attitude and orbital dynamics. The strategy seeks to provide a new alternative to the CubeSat-based soft landing problem, reducing barriers to entry in space exploration.

### 1.3.2 Specific objectives

The specific objectives required to fulfill the work are:

**SO1** Design a simulator to propagate the dynamic response of the lander to thrust in a 1-dimensional scenario.

**SO2** Design and evaluate a robust control function to demonstrate the effectiveness of soft-landing in a 1-dimensional scenario and for three types of PGCS: Regressive, Neutral, and Progressive.

**SO3** Model the problem in 2-dimensions to include effects of orbit energy, Delta velocity requirements, module orientation and characterize worst-case residual torque scenarios. With these results, the mechanical requirements for some actuator (such as reaction wheels) are presented together with the dynamic requirements in relation to the minimum response time of the module rotation.

**SO4** Collect and document data about the uncertainties of the attitude state parameters based on the available sensors in lunar missions or similar parameters.

**SO5** Design a robust control system for trajectory, merging with an attitude control to work simultaneously. This control system considers the uncertainties of the state variables as prior control information and uses the information from the state variables as updated information. Monte Carlo simulations are used to validate the control system in the evaluation stage.

**SO6** Design the engines and propose a rotation hardware system (such as reaction wheel, or monopropellant thrust) based on the optimized results obtained and the available space in the structure of a CubeSat 12U.

## 1.4 Organization

To develop the work of this Thesis, a description of each chapter and its relevance is broken down. **Chapter 2** presents a description of the opportunities for small modules, the advantages of using engine arrangements in solid and liquid state fuels, a description of the reported methods to solve the landing problem, control methods for solid fuels, and optimization approaches for the landing problem. A description of the SPE control issues is present with an example in 2.5. **Chapter 3** presents a description of the problem with a mathematical formulation. This contemplates the dynamics formulation in one dimension and in higher dimensions for both orbit (trajectory) and attitude. In addition, the mathematical model of the solid-state motor is presented, as are the parameters that present uncertainties within the simulation. In this chapter, some methods are mentioned to solve optimization problems and how evolutionary algorithms are used to solve com-

plex problems. The solution is used to design the control such as a linear function. To improve the result of linear function, it is proposed to use a neural networks as control functions, and the optimization results are used as input data in the training of the artificial neural network (ANN), but the development of this work is not solve. **Chapter 4** regroups the relevant points from chapter 3 for the development of this work. Consequently, Monte Carlos simulation cases used to test the proposed hypotheses are proposed. On the other hand, attitude control algorithms are used to counteract the residual torques of the engines. The optimization method is described by one and two dimensional dynamics. **Chapter 5** presents the results of the trajectory simulation cases to one and two dimensional dynamic. Preliminary results raise attitude and control requirements to counteract residual torques. Then, the performance of the SPEs on landing is shown. Finally, **Chapter 6** summarizes the findings presented in Chapters 4 and 5 and offers conclusions on the performance of SPEs, and the quantification of uncertainty in reentry prediction. Opportunities for improvement and future research are presented. The summary of this development is presented in Figure 1.2.

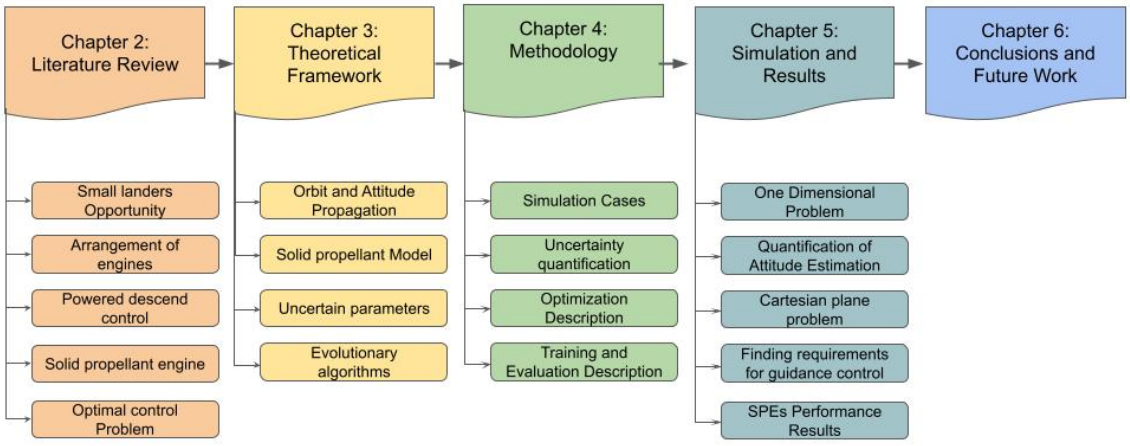


Figure 1.2: Thesis organization diagram

## 1.5 Contributions

### 1.5.1 National

The construction of any space module entails costs in the process of design, manufacturing, and development of human capital that are relatively more expensive compared to other areas of engineering. From the experience learned in the SPEL laboratory, it is observed that the most crucial factor is human capital and, therefore, good personnel management must be carried out to exploit the resources. In this sense, the design and construction of SPEs has proven to be more agile, requiring fewer initial resources compared to liquid fuel engines. This has been demonstrated in university developments by the University of Concepción, the University of Chile and the Pontifical Catholic University of Chile. However, SPEs have other problems related to control flexibility during flight and the fact that once turned on they cannot be turned off or on again, in short, the advantages of

agility are outweighed by the fact that they are hardly controllable.

Dividing the thrusts into more individual engines (increasing controllability, as shown by E. Obreque et al. [13]) allows us to continue working along the lines of SPE but thinking about more complex missions, for example, controlling the orbit of a CubeSat, performing a reentry, changing from low to high orbits, or landing on other celestial bodies. To achieve this, it is necessary to have an understanding of the limits of the engine and to know as much information as possible regarding the uncertainties, since these will be used to create a controller capable of controlling a space module based on an array of SPEs. The design of an intelligent controller capable of reducing the risk of the mission and meeting the objective will contribute to the development of SPEs in Chile.

### 1.5.2 International

At an international level, there are works done to automate space control processes, and for spacecraft to "learn" about their dynamics in space. In this sense, this work aims to initiate the development of a new mission strategy based on an array of SPEs. On the other hand, the proposed control design will not only deliver the control order or action, but it will also deliver the probability of success of the mission if that action is generated. This is crucial for systems where the actuator is limited to a finite number of actions and must be used accurately and reliably.

# 2. State of the art

This chapter presents a review of space exploration missions and the potential of small modules. The need to approach the optimization problem from another perspective is shown due to the difficulties of solid propellant engines. Given that the result is susceptible to uncertainties, a robust design must be thought of that uses the available information on uncertainties. Finally, since the location of the SPEs in the module is not precisely known and the timing of any ignition is not perfect, orientation effects must be considered. Therefore, the methods used to estimate the attitude of the module and the control method are mentioned.

## 2.1 Literature review

### 2.1.1 New opportunity for landing

Recent projects have found an attractive research point in the unexplored areas of the Moon. One of the explorations is led by the CLEP with the Chang'e landers series. The lander called Chang'e 4 was the first space mission to soft-land on the far side of the Moon On 3 January 2019 [14, 15, 16, 17]. A summary of this mission is shown in Table 2.1 along with other lander and small lander missions, which have prompted new missions such as Chang'e 5 [18], Luna 25 [19], Smart Lander for Investigation Moon (SLIM) [20], the Altair lunar lander [21], and XL-1 [6]. The XL-1 is a small, single-use lander capable of placing a 100-kg payload on the lunar surface. XL-1 is sized for launch as a secondary or ride-share payload on Falcon 9, Atlas V, or Delta IV launch vehicles. These launch vehicles have standardized spaces available for spacecraft, and the most recently known dimensions are those based on CubeSat Design Specification (CDS).

Based on the standardization of CubeSat, new studies and opportunities for lunar exploration have arisen. Astrobotic Technology presents a project called CubeRover to send one kilogram of payload per $4.5 M, which focuses on planetary exploration using a CubeSat 2U as rover [25]. Himangshu Kalita et al. [26] introduce a new lander perspective with a 27U lunar module with stored dimensions of 34 x 35 x 36 cm and a mass of 54 kg. The main components used in this module are commercial and among them is the ecological High-Performance Green Propellant (HPGP), which provides a higher specific thrust and a higher density of propellant. On the other hand, the architecture of HPGP propulsion systems consists of commercial off-the-shelf (COTS) components, enabling a simplified transition away from hydrazine and allowing the overall mission cost to be reduced.

Table 2.1: Lander mission summary [7, 22, 23, 24].

| Landing year: | 1966 | 1976-77 | 1997 | 2004 | 2019 | 2020 | 2022 |
|---|---|---|---|---|---|---|---|
| Mission: | Luna 9 | Viking 1&2 | MPF | MER-A MER-B | Chang'e-4 | Chang'e-5 | Luna 25 |
| CBT | Moon | Mars | Mars | Mars | Moon | Moon | Moon |
| IEV [km/s] | 2.6 | 4.7 | 7.26 | 5.4 - 5.5 | 1.7 | 1.7 | ~ |
| Entry mass [kg] | 1584 | 992 | 584 | 827 – 832 | 3780 | 3735.4 | 1750 |
| Entry attitude control | - | 3-axis RCS | 2 rpm spin - passive | 2 rpm spin- passive | - | | - |
| TDD | Amine-based and nitric acid | Monoprop. N2H4 | Solid rockets | Solid rockets | Unified-bipropellant system | Unified-bipropellant system | - |
| TDVC | unknown | throttled | sep. cutoff | sep. cutoff | pintle-type flowrate regulating | pintle-type flowrate regulating - throttled | throttled |
| TVV, m/s | | 2.4 | 12.5 | 5.5 - 8 | 1.5 | 1.99 | 1.5 - 3 |
| TDM, kg | ~780 | 590 | 360 | 539 | 1080 | 1837.4 | |
| ULM, kg | 99 | 244 | 92 | 173 | 140 | ~300 | ~30 |
| 3-sigma LEMaA km | NA | 280 | 200 | 80 | 26.7 | - | - |
| 3-sigma LEMiA km | NA | 100 | 100 | 12 | 13.5 | - | - |

- CBT: Celestial Body target
- IEV: Inertial entry velocity
- LEMaA: Landed ellipse major axis
- LEMiA: Landed ellipse minor axis
- RCS: Reaction control system
- rpm: Revolution per minutes
- TDD: Terminal descent decelerator
- TDVC: Terminal descent velocity control
- TVV: Touchdown vertical velocity
- TDM: Touchdown mass
- ULM: Useful landed mass

However, this propellant still has low levels of methane toxicity, requiring a specialized laboratory with experts in these technologies. Furthermore, they require additional elements such as tanks and valves to work, which take up extra volume in the lander [27]. Other works by Himangshu Kalita et al. [28, 26] present some opportunities for CubeSat science missions, such as visual navigation, environmental sampling, geographic and geophysical surveys, and performing in situ analysis and instrument configuration. Another

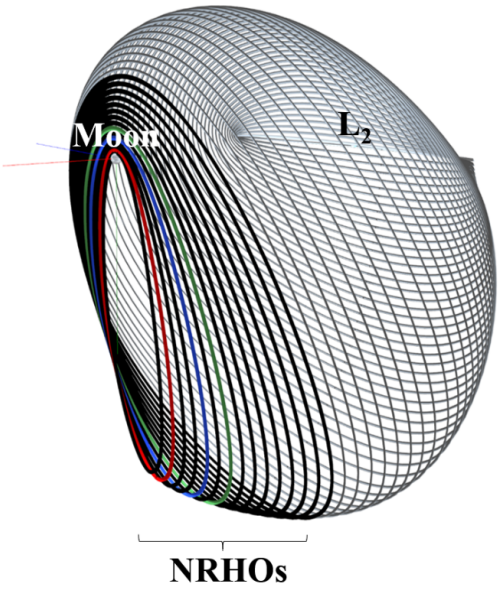


Figure 2.1: NRHO family for the Lunar Gateway station. Extracted from [30].

important advance in this matter is presented by the Japan Aerospace Exploration Agency (JAXA) with its 6U CubeSat lander called OMOTENASHI [29]. They propose to transport the module as a secondary payload in NASA's Space Launch System (SLS) Exploration Mission 1 (EM-1) launch, launch that has been postponed until August 2022. OMOTENASHI consists of scientific instrumentation with an SPE in the propulsion system, which is used to slow down the module in orbit and start descending. Then the speed of the module decreases to a speed close to 50 m/s. As the SPE cannot be controlled and there are uncertainties in the position and ignition point, a shock absorption mechanisms are needed, for which they employ three types of technology, namely, an airbag, a crushable material, and epoxy filling. On the other hand, it has 2 commercial gaseous propulsion systems (MiPS-VACCO) to control the attitude of the module in flight and correct SPE errors. This shows that there are two possible ways to get to the moon, one with NASA's SLS, and one as a Lunar Gateway payload.

Accompanying the mentioned new opportunities in lunar exploration, the Lunar Gateway is expected to operate in the future like a space station. The Lunar Gateway will be a station orbiting the Moon in an expected position of Near Halo Rectilinear Orbit (NHRO) as shown in Figure 2.1. NHRO provides vital support for a sustainable, long-term human return to the lunar surface, which is a critical component of NASA's Artemis program [10]. According to the Artemis program, the colonization of the Moon requires a better understanding of the lunar surface that needs to be explored. In this sense, this exploration can be done with multi-rovers that present a simultaneous sample of the lunar environment, such as geographic information and magnetic fields. For example, the moon's magnetic field does not have a magnetic dipole like Earth's, and it has magnetic fields with high transients in some regions [31]. This information is critical to the Lunar Gateway's navigation systems, which require an accurate model of the magnetic field based on simultaneous data collection from multiple landers and multiple rovers. However, to land a larger number of rovers in different locations, it is necessary to reduce the costs, mass of the module, volume of the components, and dimensions of the landers and rovers. That is

why CubeSat-based landers could play a fundamental role in the future. And to reduce costs and technological complexities, the use of SPE arrays in CubeSat is explored.

### 2.1.2 Arrangement of engines

Past missions have generated a set of propulsion system improvements that can now be applied to solid propellants. The Viking module featured a propulsion system based on a multi-nozzle engine arrangement, called the VLC-REA, or Viking Lander Capsule Rocket Engine Assembly [32, 1]. The VLC-REA used liquid propellant in a complex nozzle configuration that demonstrated higher performance by replacing the operation of a single nozzle with an arrangement of nozzles. Then, the arrangement reduced the temperature reached in the structural walls and **reduced the mass** of the engines [33]. However, the MPF mission first investigated this feature in 1967 with a simplified model in order to improve the lander's performance and reduce the total mass required. MPF used three SPEs as retro-rocket engines, which ignited simultaneously to decelerate. Then, an airbag system was used to prevent damage when impacting the surface of Mars at 12.5 $m/s$ (as shown in Table 2.1). As the firing of the engines was simultaneous, an energy damping system was necessary to avoid impact damage, since the SPEs cannot land smoothly if used in the traditional way. However, benefiting from the physical advantages of using an array of engines such as the VLC-REA and the MPF, it is proposed to independently control the ignition of each engine in the array, allowing greater control flexibility. Recent examples of the use of an array of micro-SPEs can be seen in orbital and attitude control systems for CubeSat satellites [34, 35, 36], but not for soft-landing problem.

### 2.1.3 Powered descend control

Previous work and analysis were made on the landing problem. The use of Pontryagin's principle to find the optimal control on the Moon landing is presented by [37, 38]. They present a simple way to design a switching function for optimal ignition control with constant thrust in one degree of freedom. Recently, the optimal pinpoint and soft-landing problem have been solved and reported by [39, 40, 41, 42, 43, 44, 45], but they assume the use of a propulsion system with a controllable thrust profile. The thrust profile can be controlled using liquid propellants such as hydrazine, which has been used with different actuation technologies: the Throttlable method and Pulse Width Modulation (PWM) where the flow is controlled by valves [46]. Either requires sophisticated technologies and expensive, which are other important challenges to be solved in future space exploration missions. Guidance and control systems using solid propellant are reported by Xiaohua Zhang et al. [47], where a piece-wise affine MPC-based attitude control for a CubeSat during orbital maneuver is presented. But the focus of that work is on external control rather than propellant. They consider the uncertainties of the residual force and torque that the engine generates and design an attitude control to counteract them in an orbital maneuver. Limited documentation and technological development exist regarding soft control with SPEs, because traditional SPEs have a predefined thrust profile that depends on Propelling Grain Cross-Sections (PGCS) and cannot be controlled in flight (traditional SPE). The next subsection explains what the PGCS is and how it is involved in the landing problem. Then, in section 2.2, the general optimization concept is developed to be formalized in this work.

Generally, to solve the soft-landing problem on the Moon, the final position of the module with respect to the target location and the mass of the propellant used are optimized. What is sought in the optimization is to minimize the error with respect to the target and minimize the propellant used by the SPEs. Additionally, aspects related to the attitude of the module must be considered, since its rotational dynamics should respond to the residual torques in a certain period of time. Starting with the control of trajectories, conceptual examples can be taken of Meditch [37], Apollo guidance [48], and Change's 5. Regarding the attitude and trajectory control and its optimization in the pointing process, the reference [45] presents a fusion of optimization methods. It uses Pontryagin's Maximum Principle (PMP) to obtain the optimal control law that minimizes the action time of control. Then, Sánchez-Sánchez and Izzo present the training of an artificial neural network (ANN) based on the results of the PMP for a given number of trajectories and simulations. With the ANN, the chattering presented by the PMP is improved, and the convergence of the results is ensured by becoming the system controller. Other work in control matter with ANN is present in [49, 50]. They show that the design of the control begins with the identification of the plant system, which is done through the ANN. For identification, a Reinforcement ANN can be used with data obtained in real time, or a network architecture of the Multilayer Perceptron type with previously obtained data, then the ANN associated with the control system is derived.

As an example, Chang'E 5 module show a guidance flow of the estimation and control system separated into 3 main blocks: Optimal guidance calculation (OGC), Optimal guidance assessment (OGA), and Environmental uncertainty learning (EUL). In the EUL part, the engine-specific impulse and constant maximum thrust are estimated using online acceleration measurements with the least square method. In the OGC part, a linear tangent thrust parameters for the guidance is determined from a target delta velocity $V_{go}$ and adaptive parameters. With guidance parameters, the direction command of the constant thrust is determined online. Regarding the sensors available in the Chinese module for the ADCS, there are accelerometers, start tracker (STT), Inertial measurement unit (IMU), laser altimeter, Radar velocimeter, and gamma sensor for the last 30 meters. These sensors will be used to estimate state variables such as position, velocity, orientation and angular velocity. A description of the proposed module is detailed in the following subsection, which incorporate the main component needed for the mission.

The drawback of these methods with respect to the presented problem is that there is only one ignition per motor, we can learn something after pushing the motor, but we cannot apply this knowledge in the next step, because the state of the module, its properties and the new engine to burn are different. That is why it is more important to use these tools in a robust design approach, so that the control does not need updating during descent. For this to work, the control design must consider the problems of the SPEs and how they are affected by uncertainties. A description of SPEs is presented in the next section.

### 2.1.4 SPEs and PGCS

In a SPE, the PGCS is the transverse geometry of a propellant grain that best represents the progression of burning area $A_b$, some of these geometries are shown in the 2D examples in Figure 2.3. PGCS can be modeled mathematically according to D. P. Mishra [51] and other

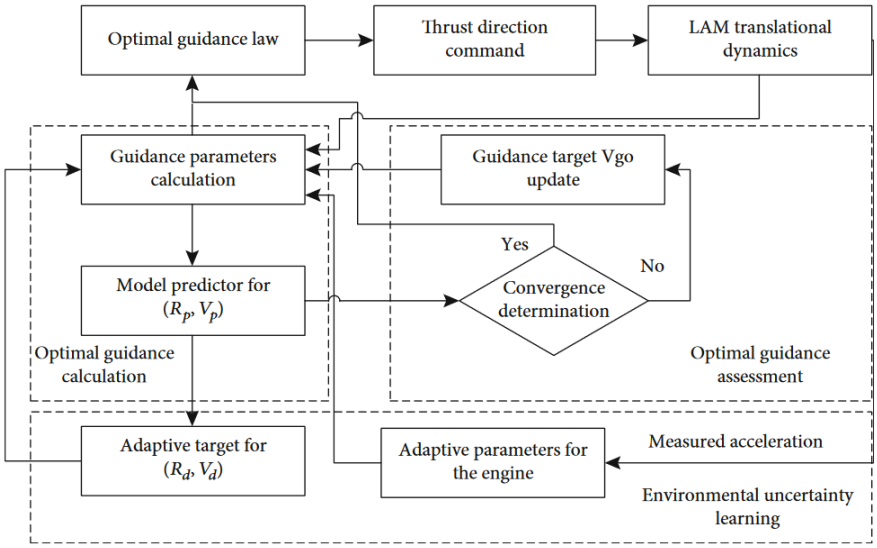


Figure 2.2: Diagram of Chang'E-5 LAM intelligent guidance. Extracted from [23].

advanced research presented by [52], where a three-dimensional grain burn is modeled and simulated. Knowing the model is important to capture important engine phenomena such as axial pressure drop, shock wave propagation, and erosive burning effects. Among these engine features is the model of the engine's thrust with relation to time, a key feature known as the **thrust profile**. This thrust profile model is required for the development of this study and the control system design, and some free software such as OpenMotor may be utilized to simulate the thrust. More detail will be discussed in the subsection 3.1.3.

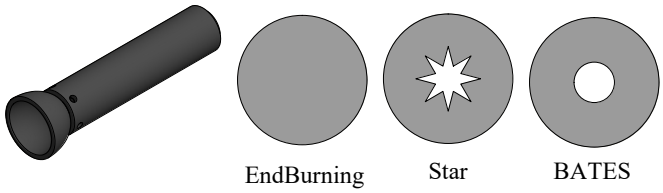


Figure 2.3: Example of solid propellant engine with EndBurning, Star and BATES PGCS.

The analytical methods present in the literature are generally based on static assumptions oriented to engine design, that is, the combustion temperature is constant, and the pressure does not change explicitly in time, but rather varies as a function of the rate of change of the burning area (see equation (3.16)). These approximations can be improved by introducing explicitly time-dependent pressure variations, as shown by Pasquale M Sforza [53] in chapter 12, but it is an approximation for the engine design stage and not for the full transition stage. Despite this, for this work a detailed model of the thrust and the PGCS profile is not required to find a control function. However, approximations that represent the types of burning are required, such as regressive, neutral and progressive (see Figure 2.4); and the characteristics of the propellant, such as delay times, action times, combustion time and dead times. Considering all these variations present in an SPE, it is necessary to explore new approaches to solve the landing problem. Some of these tools must be flexible to the variations and uncertainties of the states, allowing robustness in the

control design. Consequently, the following section delves into the concept of optimization applied to spatial dynamics concepts.

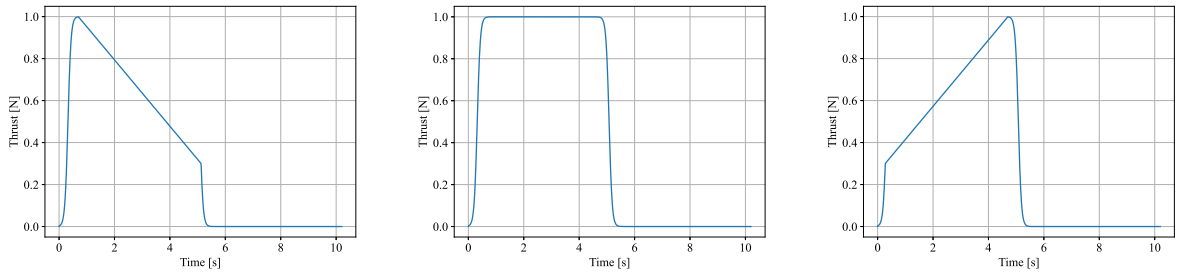


Figure 2.4: Example of Regressive, Neutral, and Progressive thrust, respectively.

Since the methods present in the literature are not designed for the soft landing problem with SPEs, it is necessary to reformulate the optimization problem to find a solution. This solution must be robust to the uncertainties of the thrust states and variables so that they do not greatly affect the control performance. The main problem is shown in Figure 2.5, showing that theoretically there is only one ignition point, and if this is not satisfied, soft landing is not feasible. For this reason, an optimization that designs a **robust control** to uncertainties should be considered [54].

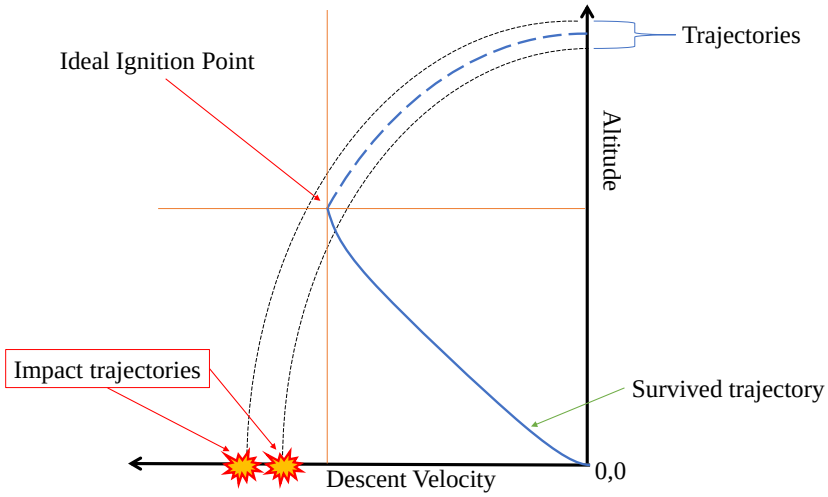


Figure 2.5: Optimal ignition point, if this is not satisfied the module will impact the surface.

## 2.2 Optimal Control Problem

### 2.2.1 General Definition

Optimal control theory has become an important field in aerospace engineering and provides indispensable tools for all types of missions. In space engineering it is important that each action consumes the least amount of energy, or fuel, or generates the least impact on the dynamics of the system, and mathematics helps us face these challenges. However, none of these processes are trivial and require extensive analysis that sometimes ends up becoming an iterative process of trial and error. Fortunately, control theory presents us with an elegant way to solve nominal type problems (without uncertainties or noise), so that the solution guarantees strong local optimization. There is a wide variety of reports in this area focused on the space sector [55, 56, 57], and to understand the basic concepts that give rise to this principle, the general formulation of an optimization problem is presented.

The general optimal control problem in *Bolza* [57] form is considered as

$$\begin{cases} \min\limits_{\boldsymbol{u}(.),\boldsymbol{x}(.)} J = \phi(\boldsymbol{x}_f, t_f) + \displaystyle\int_{t_0}^{t_f} L(\boldsymbol{x}(t), \boldsymbol{u}(t))\mathrm{d}t \\ s.t. \\ \dot{\boldsymbol{x}} = f(\boldsymbol{x}(t), \boldsymbol{u}(t), t), \\ \\ \boldsymbol{x}(t_0) = \boldsymbol{x}_0, \quad t \in [t_0, t_f], \\ \\ \boldsymbol{u}(t) \in \mathbb{U}, \\ \\ \boldsymbol{\Psi}(\boldsymbol{x}_f, t_f) = \boldsymbol{0}, \end{cases} \tag{2.1}$$

with *bold* variables as vector. The nomenclature used is listed below.

- $J \in \mathbb{R}$: Scalar cost to be minimized.
- $\phi : \mathbb{R}^n \times \mathbb{R} \to \mathbb{R}$: Terminal cost evaluation that is assumed to be continuously differentiable.
- $L : \mathbb{R}^n \times \mathbb{R} \to \mathbb{R}$: Integrative evaluation cost function.
- $\boldsymbol{f} : \mathbb{R}^n \times \mathbb{R}^m \times \mathbb{R} \to \mathbb{R}$ : Equality constraints of the state rates.
- $\boldsymbol{x} \in \mathbb{R}^n$: State variables of $n$ dimension.
- $\boldsymbol{u} \in \mathbb{R}^m$: Control variable of $m$ dimension in the set of admissible controls $\mathbb{U}$.
- $t \in \mathbb{R}$: Time.
- $\boldsymbol{\Psi} : \mathbb{R}^n \times \mathbb{R} \to \mathbb{R}^n$: Terminal manifolds

### 2.2.2 Numerical Techniques

To solve optimization problems, a series of numerical tools have been developed, which can be grouped into four categories called Direct Method, Indirect Method, Dynamic Programming and Deep Learning or simply Learning, as shown in Figure 2.6 [58].

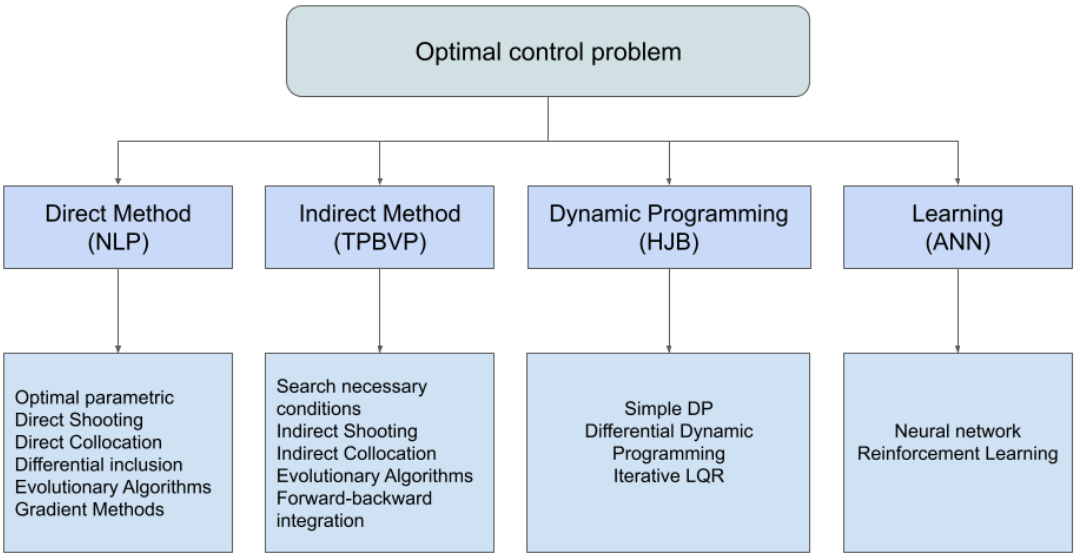


Figure 2.6: Optimal control methods including direct, indirect, dynamic programming and deep learning.

In a **direct method**, the optimal control is parameterized as a finite dimensional problem, that is, transform the problem in a Nonlinear Programming problem (NLP). Then, it is solved numerically by well-developed algorithms for constrained parameter optimization. Some numerical method are: Direct shooting method, Collocation Method, Differential inclusion method, Gradient Methods, and method based on Evolutionary Computation [59]. A method belonging to the gradient family in the adjoint method, which has proven to be a powerful tool in optimization. However, preliminary analyzes showed little robustness when adding all the variables, uncertainties and noises to the optimization. It is proposed to revisit this method in the future, considering keeping the uncertainties and noises constant throughout a simulation, and repeating the same exercise a considerable number of times until the greatest number of possible combinations are represented [60]. In an **indirect method**, the problem is transformed into a boundary condition problem and necessary optimization conditions are satisfied. Some well-known tools are indirect shooting, indirect collocation, Evolutionary Computation, forward-backward integration, among others. **Dynamic programming method** was developed in the fifties and sixties of the 19th century, most prominently by Bellman [61], and now it attracts much attention due to the popularity of Reinforcement Learning. Thanks to the Bellman principle, optimal control problem can be transformed into the Hamilton–Jacobi–Bellman (HJB) equation. Solving HJB equation is not an easy task and faces the well-known Bellman curse of dimensionality. Some tools focus on discretizing the state space in a simple way, using Differential Dynamic Programming, or iterative LQR. **Learning-based methods** are recent

and make use of artificial neural networks (ANN) to find the solution to the optimization problem, in particular, the Bolza formulation problem [58].

The main advantages of indirect methods are the high accuracy of the solution and the guarantee that the solution satisfies the optimization conditions. However, they are frequently subject to serious convergence problems that depend on the estimated initial conditions. Direct methods are less susceptible to convergence problems than indirect methods but are less precise. They do not directly satisfy the necessary conditions, and their accompanying estimate is sometimes deficient. Dynamic programming methods are less numerically robust and less suitable for handling nonlinearity in state and constraints. On the other hand, they are still sensitive to the increase in the dimension of the state. Finally, according to [58], ANN-based learning methods are more robust and deliver better results than the methods already presented. However, they require relatively large structures (32 to 64 internal nodes) for the capabilities of a computer on board a satellite or lander. In any case, the continuous increase in technological capabilities gives us the opportunity to explore these methods in the future. For the moment, this work seeks a control law that does not contain matrices with dimensions greater than 10x10.

The Bolza problem is an ideal form for studying space trajectory optimization in which a function (such as the steering law for the thrust vector) is used to control a launch vehicle into orbit using the least amount of propellant. Of the methods presented, the best known and most used in aerospace matters belongs to the indirect methods, that is, it transforms the problem into a two-point boundary value problem (TPBVP) and which must satisfy optimization conditions. There are different approaches to transform the optimization problem that derive from the works of Euler-Lagrange, Legendre, Jacobi, Weierstrass, and Bliss [56]. These approaches seek to define necessary conditions for the solution to exist and be locally weak or strong. Euler-Lagrange, Legendre, and Jacobi define necessary conditions for the optimal solution to be a weak local minimum (necessary to find a strong local minimum). On the other hand, Weierstrass's work defines the necessary conditions for a strong local optimum. However, as mentioned in [57], "the Weierstrass condition's "set of all admissible controls" is limited to continuously differentiable, unbounded functions, which are by no means the only feasible controls in practice or in principle".

In this way, a more general theorem emerges, which includes boundary conditions in the control, and which depends on measurable or estimable variables. This theorem is known as the Minimum Principle, and was developed by Pontryagin et al. [62]. Pontryagin's Minimum Principle is a much stronger statement than the Weierstrass condition because it provides the most general continuity restrictions on the control and on the functions of the Bolza problem. On the other hand, the solution explicitly defines an **activation function** that is, in essence, a control law.

### 2.2.3 Pontryagin's Minimum Principle

For the development of this principle, the Hamiltonian of Euler-Lagrange's work is defined as

$$\mathcal{H}(t, \boldsymbol{x}, \boldsymbol{u}, \boldsymbol{\lambda}) = \lambda_0 L(\boldsymbol{x}, \boldsymbol{u}) + \boldsymbol{\lambda}^T \boldsymbol{f}(t, \boldsymbol{x}, \boldsymbol{u}), \tag{2.2}$$

where $\boldsymbol{\lambda}$ is a time-varying multiplier vector know as *Lagrange multipliers*, co-state or the vector of adjoint variables. In this work, $\boldsymbol{\lambda}$ is called co-state. The arguments for time-dependent variables are omitted for simplicity. The following formulation derives from the first differential condition [63].

According to the multiplier rule [63, 64], there exist continuous co-state functions $\boldsymbol{\lambda} \in [t_0, t_f]$ such that:

$$\dot{\boldsymbol{\lambda}} = -\frac{\partial \mathcal{H}}{\partial \boldsymbol{x}} \tag{2.3}$$

at each $t \in [t_0, t_f]$ on arcs where $\boldsymbol{u}$ is continuous (piecewise continuous: PWC), and $\lambda_0$ is a constant such that:

$$[\lambda_0, \lambda_1(t), \cdots, \lambda_n(t)] \neq \mathbf{0} \tag{2.4}$$

at each $t \in [t_0, t_f]$. Nevertheless, some components may be zero.

Then, if $\boldsymbol{x}^*$, $\boldsymbol{u}^*$ provide a strong local minimum to the equation (2.1), the following condition is necessary

$$\boldsymbol{u}^*(t) = arg \min_{\tilde{\boldsymbol{u}} \in \mathbb{U}} \mathcal{H}(t, \boldsymbol{x}^*, \boldsymbol{u}, \boldsymbol{\lambda}). \tag{2.5}$$

The terminal constraints for optimal trajectories are of the form

$$\boldsymbol{\Psi}(\boldsymbol{x}_f, t_f) = \mathbf{0}, \tag{2.6}$$

which for aerospace application may describe an orbital intercept, rendezvous, etc. Then, the boundary conditions are given in terms of

$$\boldsymbol{\Phi} = \lambda_0 \phi(\boldsymbol{x}_f, t_f) + \boldsymbol{\nu}^T \boldsymbol{\Psi}(\boldsymbol{x}_f, t_f), \tag{2.7}$$

where $\boldsymbol{\nu}$ is a constant Lagrange multiplier vector. Using the definition of equation (2.1), the transversality conditions are defined as

$$\begin{cases} \boldsymbol{\lambda}(t_f) = \left( \lambda_0 \frac{\partial \phi}{\partial \boldsymbol{x}_f} + \boldsymbol{\nu}^T \frac{\partial \boldsymbol{\Psi}}{\partial \boldsymbol{x}_f} \right) \\ \\ \mathcal{H}(\boldsymbol{x}_f, \boldsymbol{u}_f, t_f, \boldsymbol{\lambda}_f) = -\left( \lambda_0 \frac{\partial \phi}{\partial t_f} + \boldsymbol{\nu}^T \frac{\partial \boldsymbol{\Psi}}{\partial t_f} \right), \text{ if } t_f \text{ is undefined.} \end{cases} \tag{2.8}$$

To solve the TPBVP problem, any of the methods mentioned in Figure 2.6 can be used. However, as will be seen later, some deterministic methods require changes in the definition of the problem to stabilize the numerical solution.

### 2.2.4 Evolutionary Computation

These types of techniques are based on the iterative evolution of initial candidate solutions, through the application of algorithms disturbed by random and deterministic signals. Depending on the technique, each algorithm has its own operators, schemes and strategies. Given the diversity of techniques within evolutionary computing, two main families used in these types of problems are presented: (i) Evolutionary Algorithms (EA), and (ii) Swarm Intelligence (SI). In EAs, there is the best-known algorithm called Genetic Algorithm (GA). And in SI, the best known is Particle Swarm Optimization (PSO).

The GA has already proven to be an important tool for optimizing a robust control design [65, 66]. Gao et al. [67] present an optimization formulated as a minimax problem so that system performance is optimized in the worst-case of uncertainty. Their strategies integrate the objective functions of the subsystems to obtain a systematic optimization using a set of weights. However, in the landing problem, worst-case uncertainties do not necessarily lead to worst-case landings. The landing process is a non-linear process that must be considered as a set of cases within the uncertainties. In this context, a second approach is presented by Sekaj [68]. In his work, the cost function used in the robust design is the sum of all the sub-cost functions of population simulations carried out, where the populations differed by the standard deviation of the initial state uncertainties. This robust design philosophy is implemented in this work. However, due to the large number of variables to be optimized and explored, the genetic algorithm may be inefficient with respect to work time due to the number of operations required in the optimization. On the other hand, according to [69] the Particle Swarm Optimization (PSO) algorithm is a better tool for optimizing large numbers of variables and for continuous problems.

**Genetic Algorithm**

A genetic algorithm (GA) is a search and optimization technique inspired by the process of natural selection. It is used to find approximate solutions to complex problems where an optimal solution is not known in advance. Genetic algorithms are commonly employed in various fields, including computer science, engineering, and biology.

A GA consists of the following key components:

1. **Population**: A collection of potential solutions to the problem, represented as individuals or chromosomes.

2. **Fitness Function**: A function that quantifies the quality or suitability of each individual within the population. It guides the search for the optimal solution.

3. **Selection**: The process of choosing individuals from the current population to create a new generation. It favors individuals with higher fitness.

4. **Crossover (Recombination)**: The process of combining genetic information from two or more individuals to create new individuals. It introduces diversity into the population.

5. **Mutation**: A small random perturbation applied to some individuals to introduce novel genetic material and maintain diversity.

6. **Termination Condition**: A stopping criterion, such as a maximum number of generations or reaching a desired fitness level.

The GA proceeds in the following manner:

1. Initialize a random population of individuals.

2. Evaluate the fitness of each individual using the fitness function.

3. Select individuals from the current population to form the next generation, favoring those with higher fitness.

4. Apply crossover and mutation operators to create new individuals.

5. Replace the current population with the new generation.

6. Repeat steps 2-5 for a specified number of generations or until a termination condition is met.

7. The best individual in the final population is the approximate solution to the problem.

For more information about GAs used in the design of robust controllers, the reader is referred to [67, 68]

**Particle Swarm Optimization**

The Particle Swarm Optimization (PSO) algorithm is an optimization technique inspired by the social behavior of birds and fish in search of resources. It is used to find approximate solutions to optimization problems in multidimensional spaces. In PSO, the solution is represented as a "swarm" of particles, where each particle represents a possible solution to the problem. Each particle moves through the search space following two main influences: its personal experience and the collective experience of the swarm. The PSO proceeds in the following manner:

1. Initialize swarm by given position and velocity to each particle.

2. Evaluate the fitness of each individual using the fitness function.

3. Update local Best and Update global Best

4. Update particle velocity

5. Update Particle position

6. Repeat steps 2-5 for a specified number of generations or until a termination condition is met.

7. The best individual in the final population is the approximate solution to the problem.

In PSO the solution is modelled in the form of particles which can move throughout the search space. Particles position can be find out by its position vector and its movement by its velocity [70].

$$p_{\mathrm{id}}(k+1) = p_{\mathrm{id}}(k) + v_{\mathrm{id}}, \tag{2.9}$$

where $p_{\mathrm{id}}$ is the local position of the particle id, $k$ is the current step, $v_{\mathrm{id}}$ is the velocity of the particle id. The $v_{\mathrm{id}}$ is defined as

$$v_{\mathrm{id}}(k+1) = w \cdot v_{\mathrm{id}}(k) + c_1 R_1 (p^L_{\mathrm{id}} - p_{\mathrm{id}}(k)) + c_2 R_2 (p^G - p_{\mathrm{id}}(k)), \tag{2.10}$$

where $p^G$ is the global best position of the particles, $p^L_{\mathrm{id}}$ is the best local position of the

particle, $c_1$ and $c_2$ are two positive acceleration constants numbers, and $R_1$ with $R_2$ are two random numbers with uniform distribution such as $R_1, R_2 \in [0, 1]$.

In improved versions of PSO, the inertial weight decreases linearly from the current iteration to the next. For this, two different parameters are required: $w_{max}$ and $w_{min}$. The following relationship is used to control inertial weight [71]:

$$w(k+1) = w_{max} - \frac{(w_{max} - w_{min})}{MaxIter} \cdot k. \tag{2.11}$$

The values of the PSO parameters are listed below, and they are constants in this work.

- $w_{max} = 0.8$
- $w_{min} = 0.01$
- $c_1 = 1.2$
- $c_2 = 1.5$.

.

# 3. Theoretical framework

## 3.1 Problem definition

To access the opportunities to reach the moon, we must go through three processes separated by the following stages: Entry, Descent, and Landing (EDL). The entry is the stage where the lander leaves its orbit. The descent is the stage where the parachute slows down the fall (not used for moon landings). Third, the landing, which is the stage where the module is controlled by the propulsion system to land. The full process is illustrated in Figure 3.1, where it is shown the orbit, landing, and the touch-down at a velocity close to zero on the target location. Landing at a location with precision close to a prescribed target is one of the main research challenges in the new generation of expensive exploration missions. Because these missions, such as InSight and Mars Science Laboratory (MSL), have unique and expensive landers and rovers, they reduce risk by calculating the trajectory with the greatest precision. On the other hand, great precision allows for exploring Martian caves and valleys, returning samples from other planets, and setting up permanent outposts throughout the Solar System, as mentioned by [72]. For lunar applications, accuracy is important to get close to interesting craters from a mining point of view or in the study of oxygen formation. In this sense, the focus of this research is not to improve the precision with respect to the state of the art but to present the effectiveness of using SPEs in the EDL process and to quantify the performance of the best precision achieved in soft-landing. On the other hand, it seeks to identify parameters that help us identify the engine's design, its dimensions, and if it can be integrated into a CubeSat platform. In addition to this, the technical requirements must be studied from the point of view of trajectory and attitude problems.

### 3.1.1 Trajectory and Attitude problem

In order for the lander to start "slowing down", the SPEs must start their ignition at a certain value of position and velocity to generate the correct thrust. Each thrust pulse resulting from the engine array is generated with at least two individual engines, used to cancel the torque generated by each individual engine. But due to uncertainties in the parameters of the engines and the position with respect to the center of mass, the torque is not completely removed, leaving residual torques that must be removed. Elimination of this residual torque is accomplished by the lander's attitude control system, which must adapt to changes in mass, inertia, and residual torque direction uncertainties. For this, the attitude determination and control systems (ADCS) must be created together, as can be

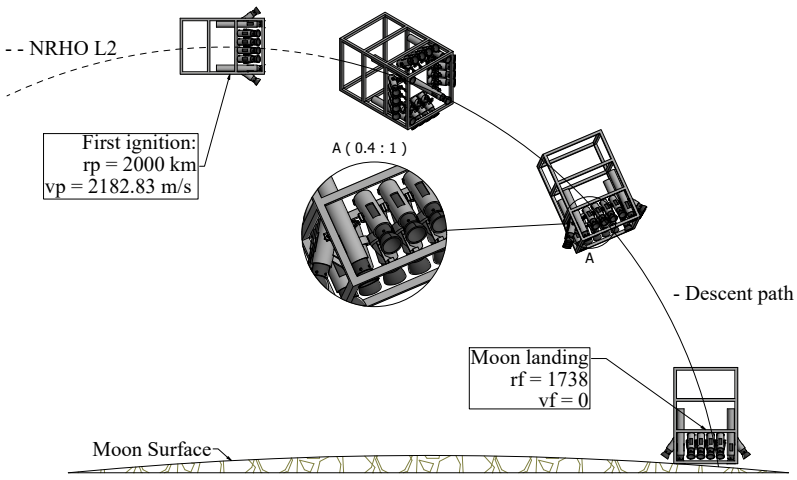


Figure 3.1: The dashed line represents the principal NRHO, and the continuous line represents the EDL process.

seen in the example of the Chang'E 5 module [23] as shown in Figure 2.2. This diagram will be used as a reference, but with radical changes in the braking process, mainly due to differences in the controllability of SPEs in contrast to liquid propellants. Without proper attitude control, the thrust generated by the SPEs will throw the module off its correct trajectory, for this reason, they must work together.

### 3.1.2 Landing module description

The lander is a 12U CubeSat structure dedicate to be the landing module, which has a square engine arrangement. The engines are limited to the maximum use of the last 8 units (8U) of the structure, but at least a space equivalent to 1U must be left for scientific instrumentation. Figure 3.2 shows the engine array into the 12U structure. The available space and mass on the 12U structure is 20 x 20 x 30 cm and 24 kg respectively as shown in the Figure 3.3. The main components that are needed during the flight are shown in the Table 3.1.

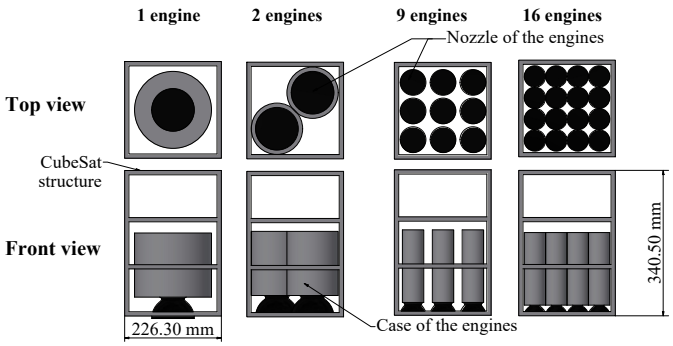


Figure 3.2: Example of 12U landers with engine arrangements. From left to right, 4 examples are shown: For a configuration of one, two, nine and sixteen engines.

Table 3.1: Basic components summary

| Component | Specification | Mass (kg) | Used space |
|---|---|---|---|
| Main structure | Aluminum | 2.0 | 12U (available) |
| On board computer (OBC) | Embedded system. Telemetry and command handling | 0.1 | 0.125U |
| Battery | Gomspace ref. Li-Ion battery pack x8, 77 Wh | 0.5 | 0.5U |
| EPS | Gomspace ref. (Photovoltaic power conversion up to 30 W) | 0.15 | 0.25U |
| Solar Panel | Gomspace ref. Body mounted, output ~40W | 1.8 | External |
| Avionic | Basic sensor and actuator. The final mass of the reaction wheels must be determined. | 1.0 | 2U |
| Telecommunication (COM) | X-Band, P-band, S-Band | 0.5 | 0.5U |
| **Total basic** | | **6.05** | 3.875U |
| | Availability for instrumentation and SPE array | ~17.9 | 8.125U |

### 3.1.3 Dynamic model

The dimensions will be analyzed under 2 approaches to demonstrate the effectiveness of soft landing in steps. The first consideration will be in 1-dimension, which is used to obtain preliminary results and demonstrate that the robust design satisfies the control requirements with an SPE array. The second stage uses 2-dimensional dynamics and attitude. The latter are used to analyze the aforementioned attitude problem.

#### 1-Dimension

According to the reference frames in Figure 3.3, the 1-dimensional (1D) model during the landing process is defined as

$$\ddot{y} = g_m + \frac{F}{m} \tag{3.1}$$

$$\dot{m} = -\frac{F}{I_{sp} \cdot g_{\mathrm{e}}}, \tag{3.2}$$

where $y$ is the altitude, $g_m$ is the Moon gravitational acceleration, and $m$ is the mass module. $g_{\mathrm{e}}$ is the earth gravity acceleration at zero altitude, respectively.

#### 2-Dimension and attitude

The 2-dimensional (2D) model is based on the orbital trajectory by the Two Body Problem similar to Chang'E 3 analysis [73], which is shown in Figure 3.4. The inertial reference frame $O$ is in 2D dynamic model, which is fixed on the lunar center of mass. The moving frame of reference $\mathcal{R}$ has the same orientation as the frame $O$, but it moves together with the center of mass of the body. On the other hand, the reference frame $\mathcal{B}$ is also in the center of mass, but it can rotate with respect to $\mathcal{R}$. Then, the equations that define the behavior of the dynamics are presented below.

$$\ddot{\mathbf{R}}^{\mathrm{i}} = \frac{F}{m}\mathbf{u}_F^{\mathrm{i}} - \frac{\mu_m}{R^3}\mathbf{R}^{\mathrm{i}} \tag{3.3}$$

$$\dot{m} = -\frac{F}{I_{sp} \cdot g_{\mathrm{e}}}. \tag{3.4}$$

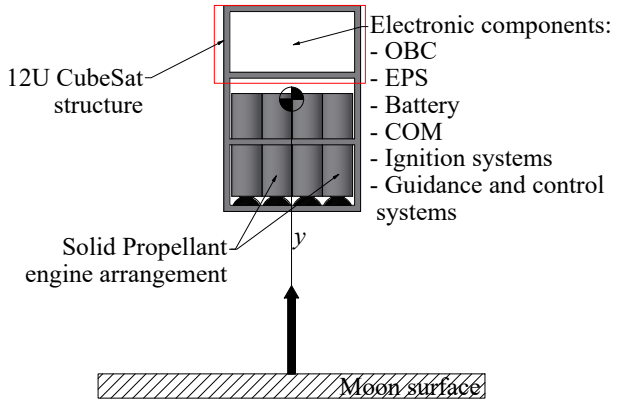


Figure 3.3: Example of a lander with 10 thrusters in the engine array in a 1-dimensional dynamic model. The inertial reference frame is fixed on the lunar surface, and is perpendicular and positive to it. This configuration frees up space equivalent to 4U for electronic components.

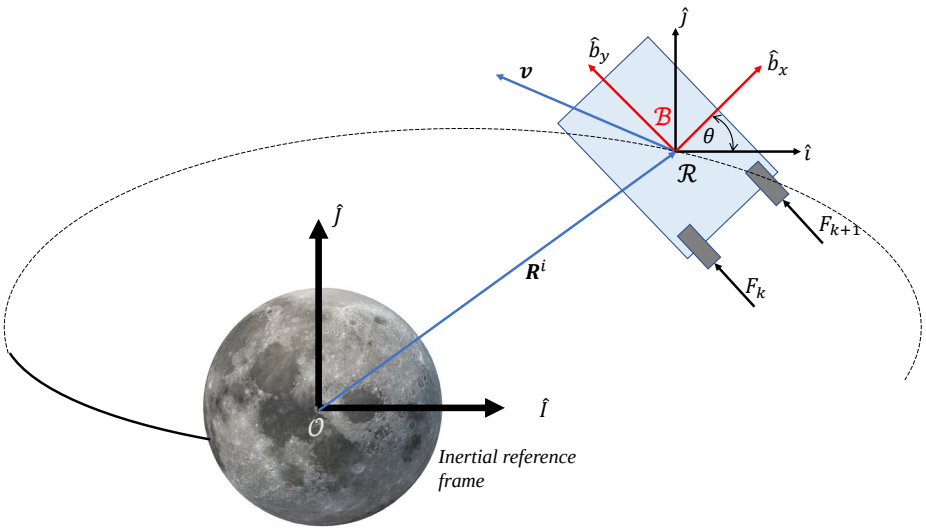


Figure 3.4: Relation between the inertial reference frame $\mathcal{O}$, moving reference frame $\mathcal{R}$, and body-fixed frame $\mathcal{B}$ in the landing process.

Here, $\mathbf{R}^{\mathrm{i}} = (x^{\mathrm{i}}, y^{\mathrm{i}})$ is the position vector from center of mass of the moon interpreted in the inertial frame, $\mu_m$ is the standard gravitational parameter of the moon, and $\mathbf{u}_F^{\mathrm{i}}$ is the unit vector of thrust represented in the $\mathcal{R}$ reference frame (the subscript i is preserved since it is inertial with respect to rotation). The propulsion system is fixed on the body-fixed frame $\mathcal{B}$, therefore the thrust unit vector $\mathbf{u}_F^{\mathrm{i}}$ is given by the orientation of the $\mathcal{B}$ with respect to $\mathcal{R}$, i.e,

$$\mathbf{u}_F^{\mathrm{i}} = \begin{bmatrix} \cos\theta & -\sin\theta \\ \sin\theta & \cos\theta \end{bmatrix} \mathbf{u}_F^b. \tag{3.5}$$

Here $\theta$ is the angle of $\mathcal{B}$ with respect to $\mathcal{R}$, which is obtained by attitude dynamics.

The **attitude** dynamics of the module is derived for the total angular moment conservation, where the angular moment is defined as $H = J\omega$ with $J$ and $\omega$ are the inertial matrix and angular velocity, respectively. The total angular moment conservation for lander with reaction wheel is $H_T = H_L + H_{RW}$, where $H_L$ and $H_{RW}$ are the angular moment of lander and reaction wheel, respectively. Then, using the Euler equation for rigid bodies interpreted in $\mathcal{B}$, $H_T$ becomes

$$\dot{H}_T^b = J_L^b \dot{\omega}_b^{\mathrm{i}} + J_{RW}^b (\dot{\omega}_b^{\mathrm{i}} + \dot{\omega_{RW}^b}) = \tau^b, \tag{3.6}$$

where $\omega_b^{\mathrm{i}}$ is the absolute angular velocity of $\mathcal{B}$ with respect to $\mathcal{R}$, $J_L^b$ and $J_{RW}^b$ is the inertia of lander and reaction wheel in $\mathcal{B}$, respectively. $\omega_{RW}^b$ is the angular velocity of the reaction wheel with respect to $\mathcal{B}$. $\boldsymbol{\tau}^b$ is the total **external** torque interpreted in $\mathcal{B}$. Solving for the angular acceleration of the module, equation (3.6) gives

$$\ddot{\theta} = \dot{\omega}_b^{\mathrm{i}} = -\frac{J_{RW}^b \dot{\omega_{RW}^b} - \tau^b}{J_T^b}, \tag{3.7}$$

with $J_T^b = J_L^b + J_{RW}^b$ as total inertial matrix.

**Thrust description**

The thrust $F$ is defined by the summation of all solid propellants during flight. Each engine has a predefined thrust profile that is derived from the PGCS. As part of the SPE array, these engines can be activated at different times, influencing the total thrust of the array. Then, the total thrust is defined as the sum of all engine thrust profiles working at a determinate time, and it has the ability to generate multi-level thrust magnitude $F(t)$. The total thrust generated by the arrangement with a number of $N_{\mathrm{e}}$ engines is

$$F(t) = \sum_{k=1}^{N_{\mathrm{e}}} F_k(t_k^*), \tag{3.8}$$

where $F_k(t_k^*)$ is the thrust profile of each $k$-engine defined by the solid propellant burn area, and $t_k^* = t - t_{\mathrm{i}g,k}$ is the current action time that start at the ignition time $t_{\mathrm{i}g,k}$ for a given time $t$ in the simulation.

To find the best performance of the thrust profile of each engine, we compared three different PGCS: Regressive, Neutral, and Progressive. These are related to star-regressive burning, tubes with rod-neutral burning, and star-progressive or tubular burning (BATES), respectively [51, 74]. In each type of PGCS, we assume that the engines have the same

Table 3.2: Advantages and disadvantages of different PGCS

| | Advantages | Disadvantages |
|---|---|---|
| EndBurn | - Neutral burning.<br>- Long action time.<br>- Stable and neutral thrust. | - Low thrust.<br>- The chamber wall must be thick (greater weight) due to direct and long exposure of high-pressure and high-temperature combustion gases. |
| Star | - Neutral, progressive and regressive burning area.<br>- The shape of the star can be modified depending on the thrust requirements.<br>- Low weight. | - Short action time.<br>- The shape is more difficult to manufacture compared to the others. |
| BATES | - Progressive burning.<br>- High final thrust.<br>- Low weight. | - Very low thrust at the start of ignition.<br>- Short action time. |

maximum thrust max($F_k$) and $I_{sp}$ in the arrangement. The mathematical model of the PGCS is based in the equation of the next subsection 3.1.3. However, a lag time $t_l$ must be added with first-order approximations.

**PGCS model**

To simulate the progression of the burning area for a given PGCS, computational tools such as OpenMotor can be used. OpenMotor is a software based on a static theoretical model [75] and the Fast Marching Method (FMM) to propagate the burned area. According to Chen Cheng et al. [76], FMM is a fast solution of the implicit Level Set Method (LSM) on the premise that burning speed is always positive and remains unchanged with respect to time. Then, with the defined PGCS combustion model, the mass flow $\dot{m}$ and thrust are obtained by means of the specific impulse $I_{sp}$ of the propellant mixture, which can be obtained using a chemical reaction model of the stoichiometric equation or experimentally. To complete the thrust profile model, other properties related to the general behavior of the solid propellant in the engine must be known. Some of these important properties of the mixture are the burn rate $\dot{r}$ (linear combustion rate), chamber pressure $P_c$ and temperature $T_c$, characteristic velocity $C^*$, coefficient of thrust $C_F$, the specific heat ratio $\gamma$, and the throat area $A_t$. Below is a summary of the main equations related to SPE, starting with the

properties of the mass, that is,

$$\dot{r} = aP_c^n + b, \qquad (\textit{burn rate}) \tag{3.9}$$

$$\dot{m}_g = \rho_p A_b \dot{r}, \qquad (\textit{propellant mass generation}) \tag{3.10}$$

$$\dot{m}_n = \frac{A_t P_c \Gamma}{\sqrt{\mathbb{R}T_c}}; \Gamma = \sqrt{\gamma}\left(\frac{2}{\gamma+1}\right)^{\frac{\gamma+1}{2(\gamma-1)}}, \qquad (\textit{nozzle mass flow rate}) \tag{3.11}$$

$$\dot{m} = \frac{\mathrm{d}(P_c V_c/\mathbb{R}T_c)}{\mathrm{d}t} = \frac{V_c}{\mathbb{R}T_c}\frac{\mathrm{d}P_c}{\mathrm{d}t} + \frac{P_c}{\mathbb{R}T_c}\frac{\mathrm{d}V_c}{\mathrm{d}t}, \qquad (\textit{total mass flow rate}), \tag{3.12}$$

where $\mathbb{R}$ is the gas constant for the propellant. The total mass flow rate inside the engine is defined as (by assuming that $T_c$ does not vary with time)

$$\dot{m} = \dot{m}_g - \dot{m}_n = \frac{V_c}{\mathbb{R}T_c}\frac{\mathrm{d}P_c}{\mathrm{d}t} + \frac{P_c}{\mathbb{R}T_c}\frac{\mathrm{d}V_c}{\mathrm{d}t} \tag{3.13}$$

$$= \rho_p A_b \dot{r} - \frac{A_t P_c \Gamma}{\sqrt{\mathbb{R}T_c}} = \frac{V_c}{\mathbb{R}T_c}\frac{\mathrm{d}P_c}{\mathrm{d}t} + \frac{P_c}{\mathbb{R}T_c}\frac{\mathrm{d}V_c}{\mathrm{d}t}. \tag{3.14}$$

For ideal gases and considering that the thrust of the combustion chamber changes due to the burning of the propellant, the derivative of the volume is

$$\frac{P_c}{\mathbb{R}T_c}\frac{\mathrm{d}V_c}{\mathrm{d}t} = \rho_g A_b \dot{r} \tag{3.15}$$

with $\rho_g$ as the gas density. Then, the change in pressure with time is

$$\frac{V_c}{\mathbb{R}T_c}\frac{\mathrm{d}P_c}{\mathrm{d}t} = A_b \dot{r}(\rho_p - \rho_g) - \frac{A_t P_c}{C^*}; C^* = \sqrt{\mathbb{R}T_c}/\Gamma. \tag{3.16}$$

Now the thrust profile $F$ can be obtained as

$$F = C_F P_c A_t, \tag{3.17}$$

where $C_F$ is defined as

$$C_F = \sqrt{\frac{2\gamma^2}{\gamma-1}\left(\frac{2}{\gamma+1}\right)^{\frac{\gamma+1}{\gamma-1}}\left[1 - \left(\frac{P_\mathrm{e}}{P_c}\right)^{\frac{\gamma-1}{\gamma}}\right]} + \frac{A_\mathrm{e}}{A_t}\left(\frac{P_\mathrm{e} - P_a}{P_c}\right). \tag{3.18}$$

Here, $P_\mathrm{e}$ is the exit pressure of the engine, $P_a$ is the ambient pressure, and $A_\mathrm{e}$ is the exit area of the engine as show the Figure 3.5.

**Torque description**

The total **external** torque $\tau$ represented in the body frame is defined as follows:

$$\tau^b = \tau_F^b + \tau_D^b, \tag{3.19}$$

with $\tau_F^b$ as the torque of SPE arrangement, and $\tau_D^b$ are the disturbance torques. These are defined as follows:

$$\tau_F^b = \sum_{k=1}^{N_\mathrm{e}} F_k(t_k^*)(\mathbf{d}_k^b \times \mathbf{u}_{F,k}^b) \tag{3.20}$$

$$\tau_D \in [\min \tau_D, \max \tau_D], \tag{3.21}$$

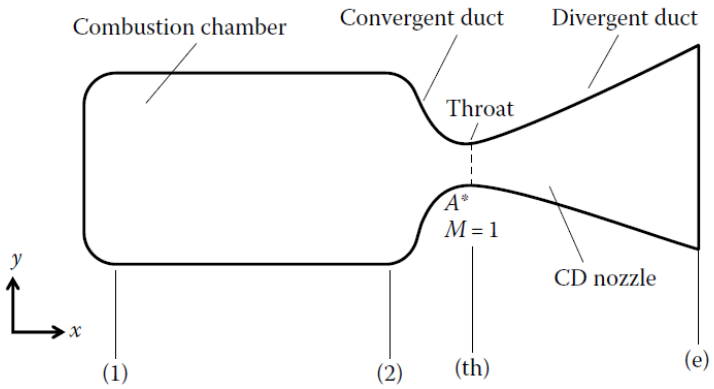


Figure 3.5: Convergent–divergent nozzle. Extracted from [51].

where $\mathbf{u}_{F,k}^b$ should be the same for all engines, but it is separated so that each engine records the random uncertainties of positioning and orientation. The $\min \boldsymbol{\tau}_D$ and $\max \boldsymbol{\tau}_D$ are the minimum and maximum value, respectively, of known uncertainties. The reaction wheel torque is **internal**, and it is explained below.

#### Reaction wheel torque model

Based on an ideal model according to the following references [77, 78], the ideal torque of the reaction wheel (with three degree of freedom) is

$$\tau_{RW}^b = J_{RW}^b \dot{\omega}_{RW}^b. \tag{3.22}$$

If we consider that the angular acceleration response is first order, we have

$$\dot{\omega}_{RW}^b = \frac{\omega_{RW}^* - \omega_{RW}^b}{\kappa_L} \tag{3.23}$$

$$\tau_{RW}^b = J_{RW}^b \frac{\omega_{RW}^* - \omega_{RW}^b}{\kappa_L}, \tag{3.24}$$

where $\omega_{RW}^*$ is the target velocity of control, and $\kappa_L$ is the lag coefficient for the first order model. Then, replacing the equation (3.22) into equation (3.7), becomes in

$$\dot{\omega}_b^{\mathrm{i}} = -\frac{\tau_{RW}^b - \tau^b}{J_T^b}. \tag{3.25}$$

### 3.1.4 Uncertain parameters

There are four categories of groups where unknown parameters are found as disturbances. Each of them is briefly detailed below.

#### Altitude and velocity

The initial altitude and velocity of the system will always have an uncertainty component derived from sensors, mathematical models, and/or estimation filters. This uncertainty

is translated into a range of unknown parameters. That is why, in the initial physical conditions, we will assume Gaussian noises, such that

$$\hat{y}_0 = y_0 + \mathcal{N}(0, \sigma_{alt}), \hat{v}_0 = v_0 + \mathcal{N}(0, \sigma_{vel}). \tag{3.26}$$

Here, $\sigma_{alt}$ and $\sigma_{vel}$ are the standard deviations for altitude and velocity, respectively. For the 2-dimensional problem, the uncertainties in each component of the vector $\mathbf{R}$ are considered.

**Specific impulse with bias and noise**

As mentioned in the first section, the value of the specific impulse of a certain propellant can vary by up to 10% from the theoretical one [3]. Therefore, the $I_{sp,k}$ of each engine will be updated once as expressed below.

$$I_{sp,k} = I_{sp} + \mathcal{N}(0, \sigma_{bias}). \tag{3.27}$$

The standard deviation, $\sigma_{bias}$, is calculated as follows.

$$\sigma_{bias} = \frac{I_{sp} \cdot 10\%}{gf}. \tag{3.28}$$

where $gf$ is a factor which is selected in function of the desired percentage within the distribution, as shown in the Table 3.3. For this analysis, the parameter $gf = 3$ was selected.

Table 3.3: Percentage within the distribution concerning $gf$.

| $gf$ | Confidence interval | Percentage within the distribution |
|---|---|---|
| 1 | +1s | 68.27 % |
| 2 | +2s | 95.45 % |
| 3 | +3s | 99.73 % |

Now, a noise signal corresponding to an erosive burn, humidity condition, and internal burning zone has been added. We assume that the noise has the same Gaussian distribution as before, and its new mean value is the $I_{sp,k}$ calculated by the last subsection. The $\sigma_{noise}$ is represented by the 3% of the theoretical $I_{sp}$ with $gf = 3$. The noise is updated in each iteration of the simulation, such as

$$\hat{I}_{sp,k}(t) = I_{sp,k} + \mathcal{N}(0, \sigma_{noise})(t). \tag{3.29}$$

A comparison of a normalized thrust with and without noise is shown in Figure 3.6.

**Ignition dead time**

It corresponds to the dead time produced in the control signal due to electrical effects, and to the initial response of the igniter. This value is randomly selected in a uniform density in $[0, 2]$ $s$. It is important to note that the dead time is different and independent of the lag time to increase the thrust, an example of ignition with dead time is shown in Figure 3.7. To define the ignition dead time $t_d$ of each engine, the next equation is used

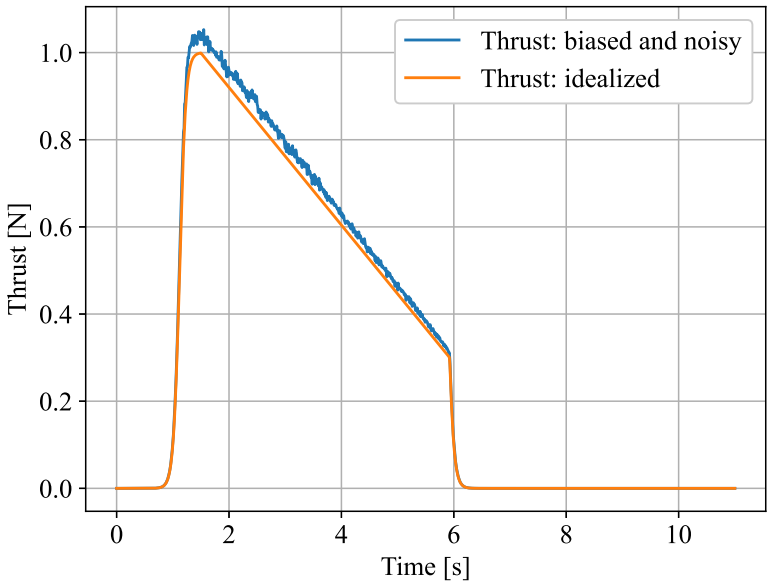


Figure 3.6: Regressive unitary thrust with bias and noise.

$$t_{\mathrm{d}} = \mathrm{Unif}(0, 2). \tag{3.30}$$

This parameter could be decreased depending on the available technology, but decreasing the ignition response is a more difficult task because it depends on the atmospheric condition of the igniter.

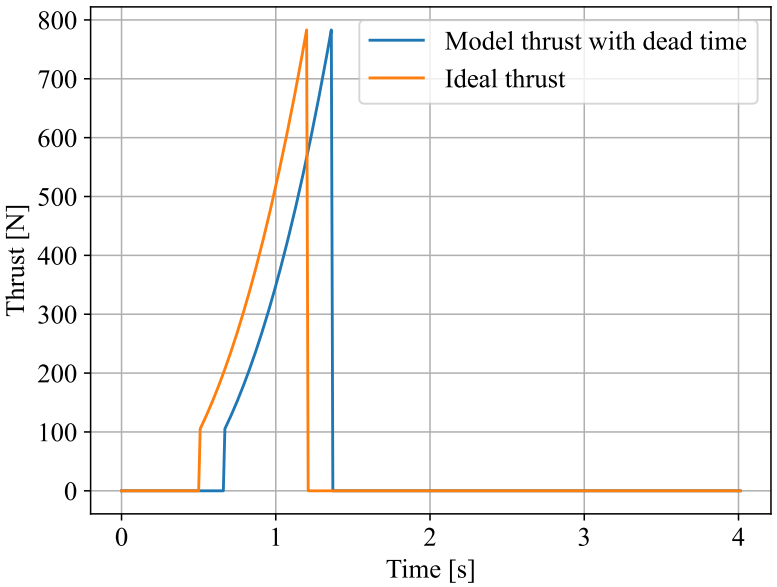


Figure 3.7: Progressive thrust with dead time.

**SPE arrangement distribution**

The distribution of the engines is assumed to be known and symmetrical to simplify the calculations. In Figure 3.8 you can see the example of an arrangement of two engines, but the number of engines still needs to be worked out for landing from orbit. The uncertainties are in the position of each engine with respect to the center of mass and the orientation of each engine with respect to the body-fixed frame.

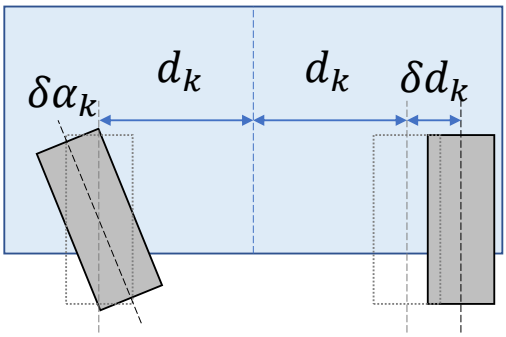


Figure 3.8: Example of SPE arrangement distribution with 2 engines. The distance of each engine from the center of mass is $\mathrm{d}_k$ and has a position uncertainty of $\delta\mathrm{d}_k$. On the other hand, the pointing of each has a deviation of $\delta\alpha_k$ with respect to the vector $u_F^b$.

Both uncertainties are considered to have a Gaussian distribution, where $\sigma_\alpha$ is the standard deviation of the angle $\alpha$ and $\sigma_\mathrm{d}$ is the standard deviation of the position. Then, the final position $\hat{\mathrm{d}}_k$ in $\mathcal{B}$ and the final orientation $\hat{\mathbf{u}}_{F,k}^{\mathrm{i}}$ in $\mathcal{R}$ for the $k$-th engine are defined as

$$\hat{\mathrm{d}}_k^b = \mathrm{d}_k^b + \delta\mathrm{d}_k; \qquad \delta\mathrm{d}_k = \mathcal{N}(0, \sigma_\mathrm{d}) \tag{3.31}$$

$$\hat{\mathbf{u}}_{F,k}^{\mathrm{i}} = \begin{bmatrix} \cos\theta & -\sin\theta \\ \sin\theta & \cos\theta \end{bmatrix} \begin{bmatrix} \cos\delta\alpha_k & -\sin\delta\alpha_k \\ \sin\delta\alpha_k & \cos\delta\alpha_k \end{bmatrix} \mathbf{u}_F^b; \qquad \delta\alpha_k = \mathcal{N}(0, \sigma_\alpha). \tag{3.32}$$

By trigonometric property and considering that for the ideal case $u_k^b = (0, 1)$, equation (3.32) becomes

$$\begin{aligned} \hat{\mathbf{u}}_k^{\mathrm{i}} &= \begin{bmatrix} \cos(\theta + \delta\alpha_k) & -\sin(\theta + \delta\alpha_k) \\ \sin(\theta + \delta\alpha_k) & \cos(\theta + \delta\alpha_k) \end{bmatrix} \mathbf{u}_F^b \\ &= (-\sin(\theta + \delta\alpha_k),\ \cos(\theta + \delta\alpha_k)). \end{aligned} \tag{3.33}$$

Finally, equations (3.20) and (3.3) become

$$\ddot{\mathbf{R}}^{\mathrm{i}} = \frac{1}{m} \sum_{k=1}^{N_\mathrm{e}} F_k(t_k^*) \hat{\mathbf{u}}_F^{\mathrm{i}} - \frac{\mu_m}{R^3} \mathbf{R}^{\mathrm{i}}, \tag{3.34}$$

$$\tau_F^b = \sum_{k=1}^{N_\mathrm{e}} F_k(t_k^*) (\hat{\mathbf{d}}_k^b \times \hat{\mathbf{u}}_{F,k}^b). \tag{3.35}$$

# 4. Methodology

This chapter presents the methodology proposed to tackle the soft landing problem using SPEs. From the previous chapters, we know that an ideal nonlinear optimization problem can be solved by PMP. The PMP method transforms the optimization problem into a TPBVP that satisfies the necessary condition of optimality. Meditch et al. [37] applied the PMP in a simplified example, showing that thrust ignition can be solved by a linear function of states. However, solutions to TPBVP are not robust to the dimensions of the states, and conditional controls like SPE, on the other hand, have chattering problems in control. To tackle this problem, I propose using evolutionary computational (EC) tools to solve the TPBVP using the boundary condition in a cost function. The solution to the optimal control problem transformed in TPBVP by PMP and solved by EC is used to design and train a robust control.

The first exploration is done based on studying the use of EC in the search for locally strong optimal solutions. Therefore, it is proposed to study a simplified one-dimensional case, as shown by the equation (3.1), and the complexity is in the activation of different numbers of thrusters independently. The advantage of this is that it will allow us to demonstrate the optimization method from the point of view of evolutionary algorithms, which do not always give local optimization results. However, using the TPBVP conditions ensures local optimization only by reducing the errors of the boundary conditions. As mentioned by Meditch et al. The approximate solution of the simplified problem is a linear function that depends on the height and the speed of descent. Therefore, the exploration shows that the evolutionary algorithms achieve similar results when solving the TPBVP directly, as when solving only the linear function.

The second part of the exploration is done based on studying the theoretical feasibility of landing with SPEs. From the previous result, the use of EC for the optimization problem is demonstrated, ensuring the boundary conditions and the linear control function. Therefore, the next step is to face the challenge of SPE with uncertainties. This control proposal should be explored by designing through two approaches: a **Classic** design and a **Robust** design, both solved through an evolutionary algorithm. The exploration is carried out for the simplified case of the equation (3.1), and its importance lies in demonstrating the theoretical feasibility of dividing the total thrust required into subthrusts. Furthermore, this validates the robust design method through a random path evaluation. To avoid adding noise to the methodology of this second exploration, the robust design technique mentioned by Sekaj [68] is used, which uses GA.

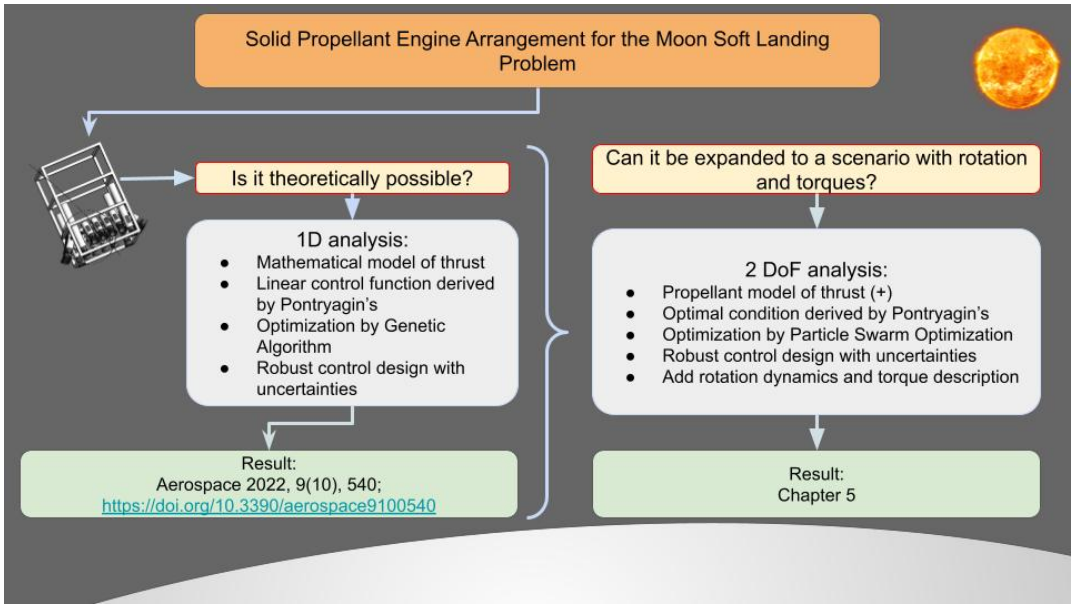


Figure 4.1: Summary of Methodology.

.

## 4.1 Task

This thesis proposal focuses on relatively low-cost small landers in the context of recent lunar exploration projects that propose to pave the way for future colonies, scientific research, and commercial activities. To achieve the proposed objectives, a series of tasks and processes must be followed that will allow us to learn from the problem and record intermediate results. Each of the actors mentioned above proposed a design strategy to land on the Moon or Mars, but this research differs in the propulsion system [39, 40, 41, 42, 43, 44, 45]. As the SPE-based propulsion system cannot be controlled, only analyzes for a single ignition point were found in the literature, and then they used gas micro-propulsion systems to correct uncertainties and an airbag system to cushion the fall. No references were found for designing system controllers with SPE arrays. For that reason, I propose a plan that divide the main problem into smaller subproblems that allow me to advance step by step towards the final goal. Some of these milestones are listed below. Then, in the Advanced Work section, preliminary results are shown in order to satisfy parts of these problems. Much of this progress was achieved in recent years of research, culminating in a study of the state of the art, design of a work methodology, and the publication of an article [13].

1. Design a landing scenario in one dimension.

2. Incorporate uncertainties and boundary conditions.

3. Design a robust controller for an array of SPEs to improve landing accuracy over the accuracy achieved by a simple SPE.

4. Analyze different types of PGCS.
5. Design a landing scenario in two dimensions.
6. Collect and document data for orientation and guidance uncertainties in lunar missions.
7. Quantify the maximum residual torque generated by the arrangement of motors.
8. Design an orientation controller to eliminate residual torques.
9. Design a landing control for the stage in two dimensions based on PSO and ANNs.
10. Integrate the two controllers: orientation and trajectory.
11. Perform sensitivity analysis of the relevant variables involved.

## 4.2 Preliminary analysis

### 4.2.1 Optimal problem - PMP

Assuming a nominal case, this problem can be solved with Pontryagin's minimal principle. For this, the following optimization problem is defined based on [37]

$$\min_{F} J_c = t_f, \tag{4.1}$$

which minimize the final time $t_f$ subject to the dynamics of the equation (3.1). According with [37, 79], minimizing the final time is analogous to maximizing the final mass of the module. The terminal constrain of equation (2.6) required that $y(t_f) = y_f = 0, v(t_f) = v_f = 0$, and $\lambda_m(t_f) = (\lambda_m)_f = 0$.

Using the Pontryagin's principle [80] we define the state $\mathbf{x} = (x_1, x_2, x_3) = (y, v, m)$ such that the Hamiltonian is,

$$\begin{aligned} H(t) &= \lambda_y \dot{x}_1 + \lambda_v \dot{x}_2 + \lambda_m \dot{x}_3 \\ &= \lambda_y v + \lambda_v \left( \frac{F}{m} - g \right) + \lambda_m \frac{-F}{v_e}. \end{aligned} \tag{4.2}$$

Now, we can rewrite the equation (4.2) with (3.8) as,

$$\begin{aligned} H(t) &= H_0 + \sum_{k=1}^{N_e} F_k(t_k^*) \left( \frac{\lambda_v}{m} - \frac{\lambda_m}{v_e} \right) \\ &= H_0 + \sum_{k=1}^{N_e} F_k(t_k^*) \Phi, \end{aligned} \tag{4.3}$$

where $H_0 = \lambda_y v - \lambda_v g$ is the part of the Hamiltonian that does not explicitly depend on thrust, and $\Phi$ is the switching function (sf) defined as,

$$\Phi = \left( \frac{\lambda_v}{m} - \frac{\lambda_m}{v_e} \right). \tag{4.4}$$

Using the condition of equation (2.5), $\Phi$ can be used as the ignition signal, which is obtained such that,

$$F_k(t_k^*) = \begin{cases} F_k(t_k^*), & \text{if } \Phi < 1 \\ 0, & \text{otherwise} \end{cases}. \tag{4.5}$$

The co-state differential equations are,

$$\begin{aligned} \dot{\lambda}_y &= -\frac{\partial H}{\partial y} = 0 \\ \dot{\lambda}_v &= -\frac{\partial H}{\partial v} = -\lambda_y \\ \dot{\lambda}_m &= -\frac{\partial H}{\partial m} = \frac{\lambda_v}{m^2} \sum_{k=1}^{N_e} F_k(t_k^*). \end{aligned} \tag{4.6}$$

If $N_e = 1$, and $F_{k=1}$ is constant, [37] gives an approximate and analytical solution. The results of this simulation can be seen in Figures 4.2 and 4.3, where different values of mass flow and burn time are used.

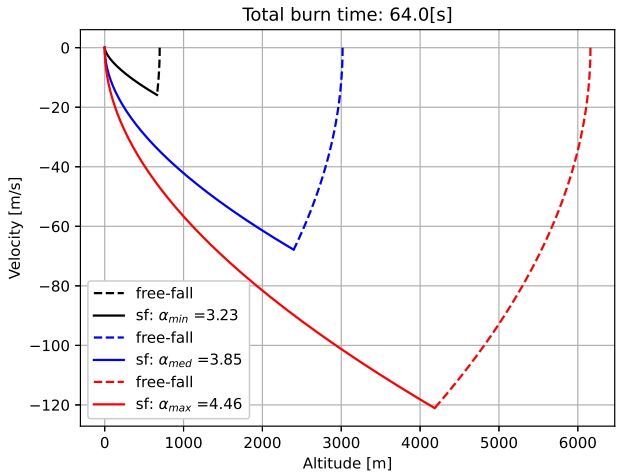


Figure 4.2: State response for different mass flow $\alpha$ with $t_b = 64$.

The Figures show examples with 3 different initial heights, where the dotted lines represent the free fall, and the solid line the trajectory after activating a constant thrust. When the burn time is constant, different descent trajectories are generated. The opposite is true when the mass flow is constant (constant thrust), where changing the burning time only affects the entry point to the main descent trajectory.

### 4.2.2 TPBVP solved by EC

The above solution can be solved with traditional and deterministic methods, as presented in Figure 2.6. However, for problems with conditioned forces and independent actuators,

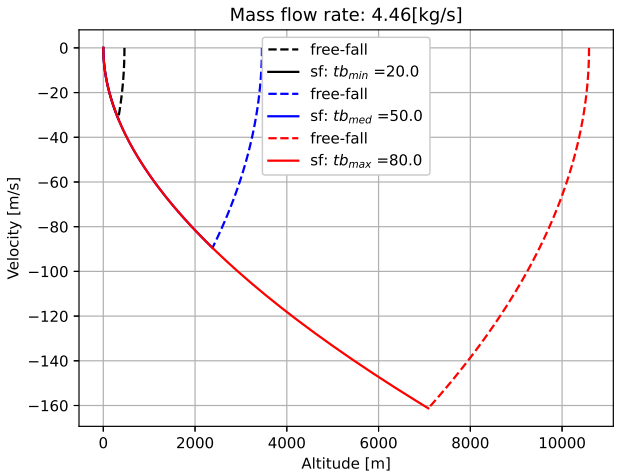


Figure 4.3: State response for different burn time $t_b$ with $\alpha = 4.46[kg/s]$.

traditional methods diverge. To solve this, it is proposed to use evolutionary methods, initially to solve the TPBVP derived from the PMP method, and subsequently show independence of the evolutionary method with respect to the PMP. To increase the degree of difficulty, the constant thrust was changed to a regressive one, whose burning time is limited to 5 seconds.

The key to this problem is to find the correct cost function associated with the boundary conditions and the ignition control function. For this, the problem is broken down step by step until the optimization is independent of the PMP method.

### TPBVP solved by EC and PMP conditions

To solve this problem we must consider the transversality condition of the Euler-Lagrange theorem, which adds a boundary condition for the co-state $\lambda_m$. Therefore, the cost function for an evolutionary optimization is,

$$J = \sqrt{(y(t_f) - y_f)^2 + (v(t_f) - v_f)^2 + (\lambda_m(t_f) - (\lambda_m)_f)^2}. \tag{4.7}$$

Using an evolutionary method, such as GA, the results in Figures 4.4 are obtained. The initial use of GA is based only on the state of the art, with more reports of it as a robust control design method [68, 81]. However, PSO is more efficient for continuous and higher dimensional problems and will therefore be used in the ultimate multidimensional exploration of this Thesis.

As can be seen, the optimization of a simplified scenario manages to satisfy the optimization conditions of the PMP using the co-states as the ignition activation function. In addition, the regressive thrust with burn time equal to 5 seconds can be observed. The objective now is to make the search for ignition points independent of the PMP using EC.

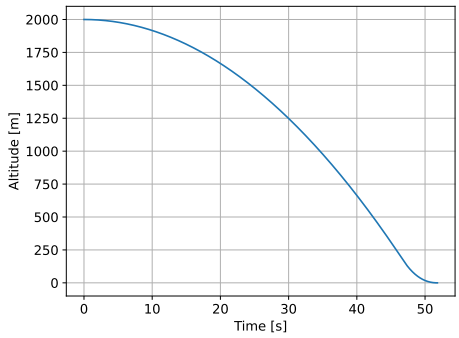


(a) Altitude

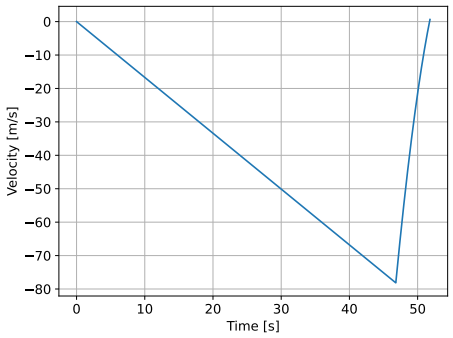


(b) Velocity

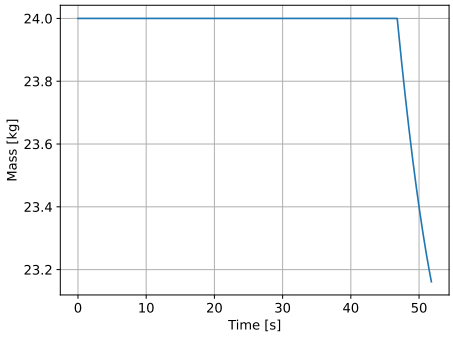


(c) Mass

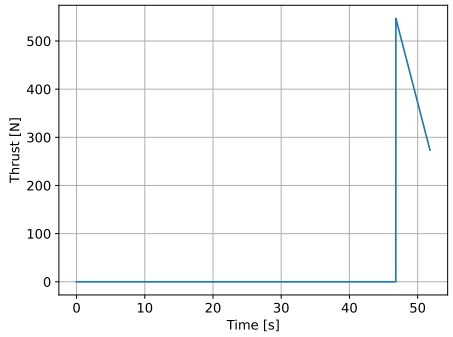


(d) Thrust

Figure 4.4: OCP based on PMP conditions and transformation to TPBVP. Solution optimized by evolutionary algorithm and minimizing the cost function of equation (4.7).

**TPBVP solved only by EC**

To search for an independent solution, a linear activation function $\beta$ is defined, such that,

$$\beta(t) = \alpha y(t) + \gamma v(t). \tag{4.8}$$

Here $\alpha$ and $\gamma$ are gains to adjust the point where ignition is generated based on the following condition.

$$F_k(t_k^*) = \begin{cases} F_k(t_k^*), & \text{if } \beta < 0 \\ 0, & \text{otherwise} \end{cases}. \tag{4.9}$$

On the other hand, the cost function is defined as

$$J = (y(t_f) - y_f)^2 + (v(t_f) - v_f)^2 + \left(\frac{t_f}{t_{free}}\right)^2, \tag{4.10}$$

where $t_{free}$ is the **free fall** time. This time is used to reduce the magnitude of the final time $t_f$ with respect to altitude and velocity error, and it is obtained by solving the following polynomial:

$$\frac{|g_m|}{2} t_{free}^2 - v_0 t_{free} - y_0 = 0. \tag{4.11}$$

The solution to this problem is shown in Figure 4.5.

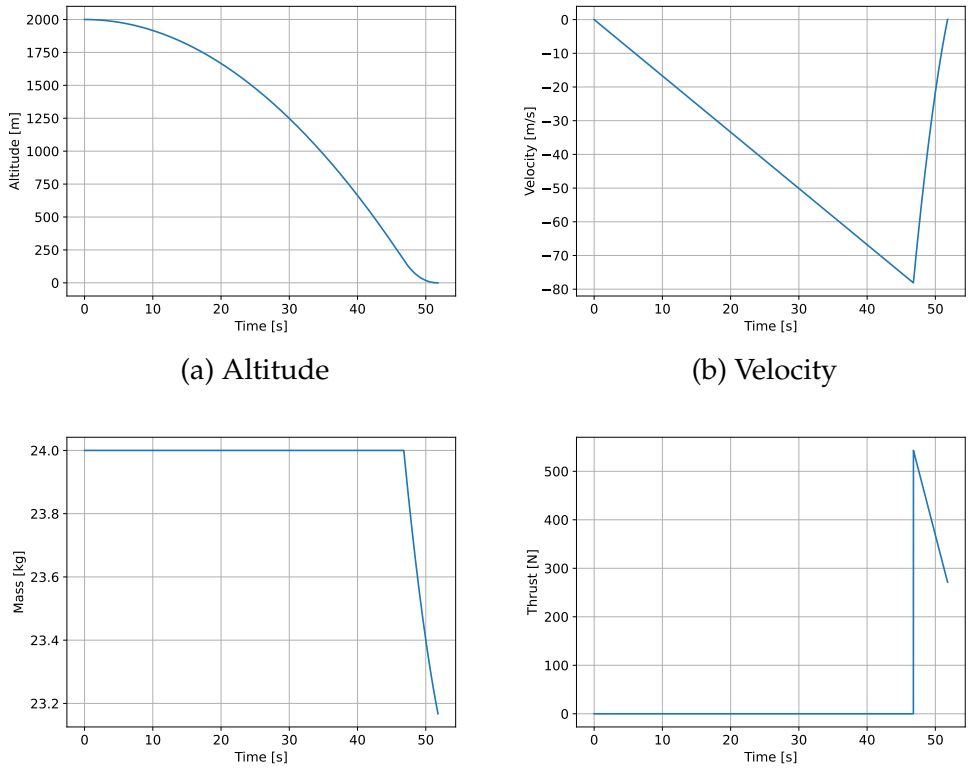


(a) Altitude (b) Velocity

(c) Mass (d) Thrust

Figure 4.5: OCP based on the boundary conditions of the states. Solution optimized by evolutionary algorithm and minimizing the cost function of equation (4.10).

## 4.3 1D Analysis

In section 4.2, a method similar to that proposed by PMP is developed, but with an independent mathematical formulation. For this, a cost function is defined that satisfies the boundary conditions, and a control function that fulfills the same function as *Phi*. For that case, a function $\beta$ is defined that only activates one thrust, but this must be expanded for a greater number of SPEs. In the development that follows, it is expanded to different numbers of SPE considering the mentioned uncertainties. On the other hand, the use of GAs for the robust design is defined in greater detail and compared with a classic design, that is, designing the control for the nominal case. The comparison of these approaches (robust and classical) allows us to further demonstrate the potential of ECs in problems with uncertainties, where the actuators have conditions prior to flight control.

### 4.3.1 Design of control function for 1D

For the purpose of this step, a simple expression that is a candidate to be the control function is select for different numbers of SPE, which is defined as

$$\beta_k(t) = \alpha_k y(t) + \gamma_k v(t). \tag{4.12}$$

The control function $\beta_k(t)$ generates the following instructions: when $\beta_k(t)$ is greater than zero, the $k$-engine stay off; when $\beta_k(t)$ is less than zero, the $k$-engine begin the ignition as

shown in the Figure 4.6. It is important to note that this function, being a straight line in the Cartesian plane, does not represent the real trajectory or velocity. This function only represents the ignition point at the instant $t_{ig,k}$, i.e., $\beta_k(t) \leq 0$.

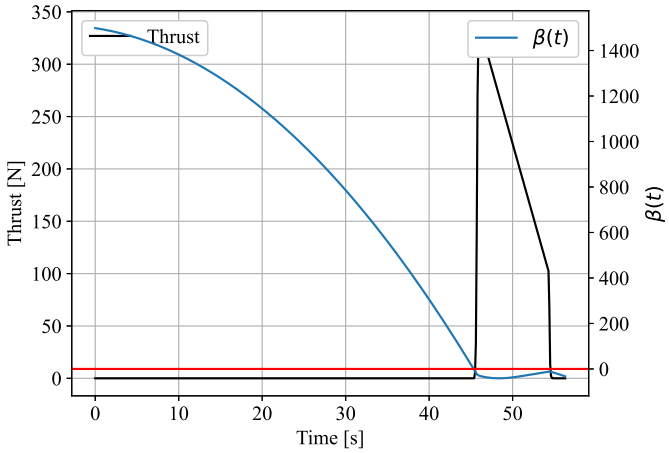


Figure 4.6: Example of activation of each engine. When the control function $\beta(t)$ is less than zero, crossing the red line, the engine turns on at the instant $t_{ig,k}$ of the simulation. The ignition delay seen in the figure is due to the dead time of the propellant.

### Boundary Conditions

The initial condition is defined by

$$y(0) = y_0\ [m], v(0) = 0\ [m/s], m(0) = m_0\ [kg], \tag{4.13}$$

and the desired final condition is

$$\begin{aligned} y(t_{land}) =& y_{land} = 0\ [m] \\ v(t_{land}) =& v_{land} = 0\ [m/s] \\ m(t_{land}) =& m_{land}\ (free)\ [kg], \end{aligned} \tag{4.14}$$

where $t_{land}$ is the time when the module first touches the surface. To estimate this value, it is important to note that due to the discretization of the simulation, the value closest to zero will be considered as the final point of contact with the surface. That is, if at time $t_k$ the height is $y_k = 0.2\ m$ and the position at time $t_{k+1}$ is $y_{k+1} = -0.1\ m$, it is considered as final surface contact the value $-0.1\ m$, and the landing time is $t_{k+1}$.

### Optimal problem

Two optimization approaches are carried out to contrast them: a direct optimization (for classic control design), and a stochastic optimization (for robust control design). The first approach considers a direct cost function as follows:

$$\begin{aligned} \min_{\dot{m},t_a,\alpha_{k=1},\cdots,\alpha_{k=N_e},\gamma_{k=1},\cdots,\gamma_{k=N_e}} J_c =& A(y(t_{land}) - y_{land})^2 + B(v(t_{land}) - v_{land})^2 \\ &+ C\left(\frac{t_{land}}{t_{free}}\right)^2;\ \ c \in [1, 2, \cdots, N_c] \end{aligned} \tag{4.15}$$

where $A, B, C$ are gain parameters, $N_c$ is the number of trajectories, and $t_{free}$ is the **free fall** time. This time is used to reduce the magnitude of the landing time $t_{land}$ with respect to altitude and velocity error, and it is obtained by solving the following polynomial:

$$\frac{g_m}{2} t_{free}^2 + v_0 t_{free} + y_0 = 0 \tag{4.16}$$

The stochastic optimization approach is defined with an average cost function as follows:

$$\min_{\dot{m}, t_a, \alpha_{k=1}, \cdots, \alpha_{k=N_e}, \gamma_{k=1}, \cdots, \gamma_{k=N_e}} \mathcal{J} = b_1 \mu_J(J_c) + b_2 \sigma_J(J_c); \;\; c \in [1, 2, \cdots, N_c] \tag{4.17}$$

with $N_c = 30$. See more details in subsection 4.3.1.

**Genetic algorithm**

In order for the GA to recreate the natural evolutionary process and find an optimal solution, it is necessary to define the terminology involved in the general process. First, the first generation of population must be created, which is usually formed randomly according to the range of the variables. This first generation is evaluated in the landing process by calculating a cost function that delivers an error value with respect to the target. Subsequently, each of the cost functions associated with the population's individuals are compared to form a second generation. This process is divided into Selection, to choose the best individuals called parents; Crossover, to create new individuals from two parents; and Mutation, to randomly affect a parameter within an individual ($\dot{m}$ for example) and prevent them from getting stuck. The full process is shown in Figure 4.7, accompanied by equation (4.18) and the definition of the population set $\mathcal{P}$.

For the selection process, 20% of the individuals with the lowest cost function (which are landings with low error relative to the target) are selected directly. The remaining 80% is selected using the roulette wheel method. For the crossover. we use two types of operators alternately to accelerate the optimization: the one Point crossover, and arithmetic crossover. The one point crossover cuts the individual of two parents randomly selected to create two children (the position of the cut is also chosen randomly). Arithmetic crossover assigns weights to both parents and then performs an arithmetic sum for each parameter within the individual. For this project, weights of 0.3 and 0.7 were used to create two children, respectively. For the mutation process, each parameter within the individual is randomly assigned a probability of mutating from 0 to 1, if one of this is less than the probability of mutation, then that parameter mutates within the value ranges. To continue, the specific definitions of individual parameters and cost functions are introduced in the following sections.

**Individual parameters**

The parameters to be optimized are the control gains, the mass flow $\dot{m}$, and the action time $t_a$. To solve, we propose the following format for a GA individual $\mathcal{G}_\text{i}$:

$$\mathcal{G}_\text{i} = [\dot{m}, t_a, \alpha_{k=1}, \cdots, \alpha_{k=N_e}, \gamma_{k=1}, \cdots, \gamma_{k=N_e}]_\text{i}, \tag{4.18}$$

where i represent the i-th individual of a generation $n_g$ of population $\mathcal{P}^{n_g} = [\mathcal{G}_1, \cdots, \mathcal{G}_{N_\text{i}}]$, with $N_\text{i}$ the number of individuals in the population.

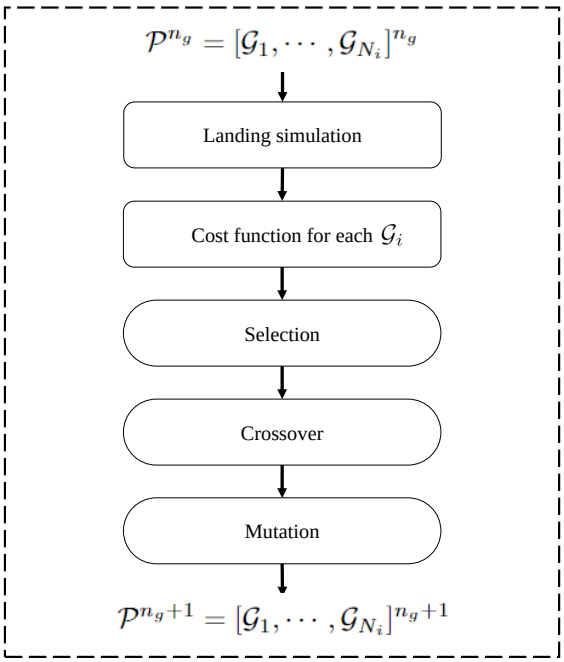


Figure 4.7: Representation of the evolutionary process of the GA, where the landing simulation is used to create a new generation of population $\mathcal{P}$ to solve the optimal problem.

**Individual cost function**

For the hypothesis **H1**, 30 trajectories obtained from the uncertainties are defined, and they are used in the optimization stage. A cost function related to the target (touching the surface with zero speed) is calculated for each of the trajectories. For each individual of the GA, the trajectories must be simulated (differentiated from each other by the uncertainties). The 30 cost functions are defined as,

$$\begin{aligned} J_c =& A(y(t_{land}) - y_{land})^2 + B(v(t_{land}) - v_{land})^2 \\ &+ C\left(\frac{t_{land}}{t_{free}}\right)^2; \quad c \in [1, 2, \cdots, N_c] \end{aligned} \tag{4.19}$$

where $A, B, C$ are gain parameters, $N_c$ is the number of trajectories, and $t_{free}$ is the **free fall** time. This time is used to reduce the magnitude of the landing time $t_{land}$ with respect to altitude and velocity error, and it is obtained by solving the following polynomial:

$$\frac{g_m}{2} t_{free}^2 + v_0 t_{free} + y_0 = 0 \tag{4.20}$$

The equation (4.19) is called as Direct Cost Function (DCF). but the optimization measurement of each individual is defined by an Average Cost Function (ACF) defined as

$$\mathcal{J} = b_1 \mu_c(J_c) + b_2 \sigma_c(J_c). \tag{4.21}$$

Here $\mu_c(J_c)$ and $\sigma_c(J_c)$ is the mean and standard deviation, respectively, of all costs $J_c$ associated with a single individual. The mean is calculated as

$$\mu_c = \frac{1}{N_c} \sum_{j=1}^{N_c} J_c, \tag{4.22}$$

and the standard deviation $\sigma_c$ is defined as

$$\sigma_c = \sqrt{\frac{1}{N_c}\sum_{j=1}^{N_c}(J_c - \mu_c)^2}. \tag{4.23}$$

The parameters $b_1$ and $b_2$ are gains. The benefit of this feature is that the selection of the best individual is based on statistical parameters that show how close all cases are to the expected landing state.

### 4.3.2 First Approach: Controller Optimization without Trajectory Uncertainties

This subsection presents the optimization for an ideal scenario without uncertainties on the training. For this scenario, we solve the optimization problem with cost function present in the Equation (4.19), that is, a single trajectory. The full process of optimization for this case is shown in Figure 4.8. The solutions obtained by the OC and the $N_e$ engines are then evaluated on an uncertain scenario. Each number of engines has a particular solution and is independent of another, so it is evaluated independently. These evaluations show the landing point for all trajectories and are used to form a velocity and altitude distribution. Subsequently, this information is used to obtain the mean and the standard deviation of the landing state for an arrangement configuration of the different numbers of engines.

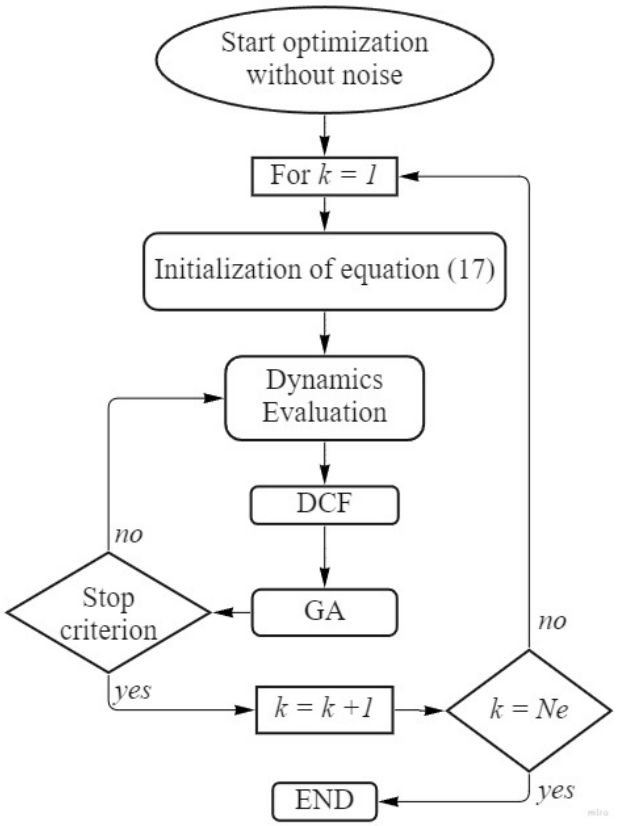


Figure 4.8: First approach: Optimization for scenarios without uncertainties in the training process.

### 4.3.3 Second Approach: Controller Optimization with Trajectory Uncertainties

As a counterpart to the previous subsection, in this scenario we use the information corresponding to the uncertainties to improve the landing of the model. Therefore, we optimize based on the recursion of the training using different initial conditions of the states for each number of engines and generation of the GA.

The optimization process begins by iterating from an array of engines from $k = 1, \cdots, N_e$, and with an initial population of candidate solutions in the GA. In each generation of the GA, we evaluate for different $N_e$. Then, the number of engines is fixed to generate $N_{case}$ of initial states defined by Equations (3.26), (3.27) and (3.30). Each of these initial states create a $j$-th trajectory with $j = 1, \cdots, N_{case}$. These cases are then evaluated in the dynamic model passing for all the individuals of the generation. In the dynamic model, the continuous noise of the specific impulse is added at each time step of the simulation. When the simulation ends, the cost of each trajectory is calculated separately according to Equation (4.19) and stored in a vector that regroups the costs of all the cases (trajectories). When all cases have been simulated, the ACF is calculated to execute the selection, crossing, and mutation process of the GA. Once some criteria for stopping the GA have been satisfied, the number $k$ of engines in the arraignment is increased, and the same process mentioned above is carried out again until $N_e$. The full process is shown in Figure 4.9.

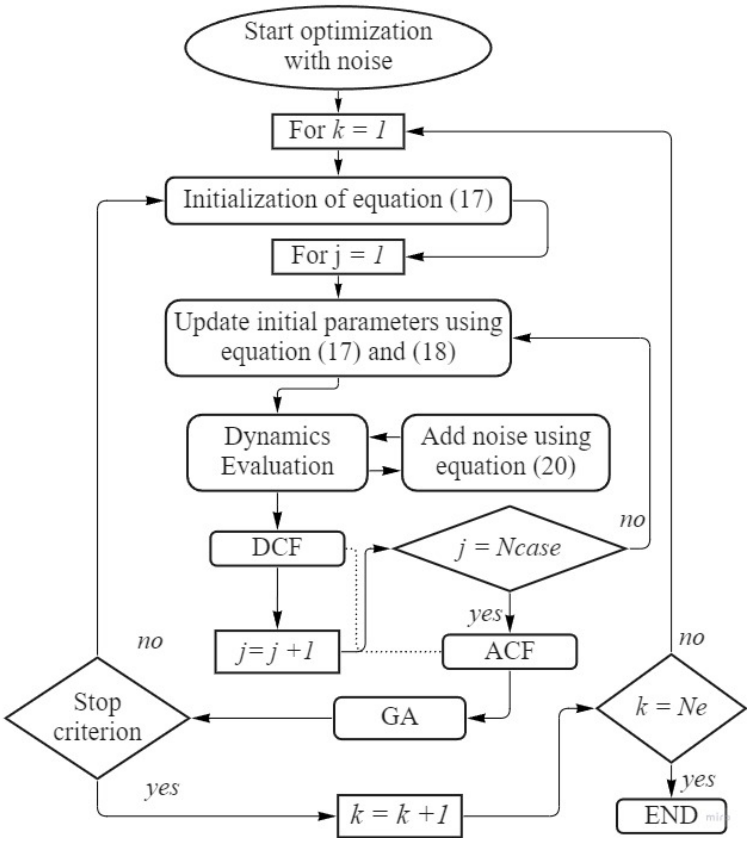


Figure 4.9: Second approach: Optimization for scenarios with uncertainties in the training process.

### 4.3.4 Thrust Model

To avoid complicating the first exploratory feasibility analysis, it is proposed to use a simpler mathematical model for propulsion. The calculations in Section 3.1.3 require numerical propagation and the definition of engine designs, among others. This is why the mathematical model presented below is used in this analysis.

#### PGCS-Regressive

The regressive thrust profile is modeled with a hyperbolic tangent function (HTF) at the beginning, a negatively sloping linear function in the middle, and again with an HTF at the end. The mathematical model for the unitary thrust $T_k(t_k^*)/\max(T_k)$ is

$$\begin{cases} \frac{\left(1+\tanh\left(\left(\frac{t_k^*}{\tau_\mathrm{d}}-\zeta\right)s\right)\right)}{2} & t_k^* \leq \tau_\mathrm{d} + \tau_l \\ \kappa_r t_k^* + c_r & t_k^* \leq \tau_r \\ \frac{\left(1+\tanh\left(\left(-\frac{\left(t_k^*-t_a-2\tau_\mathrm{d}\right)}{\tau_\mathrm{d}}-\zeta\right)s\right)\right)}{2} & t_k^* \leq \tau_\mathrm{d} + t_a + \tau_l \\ 0 & otherwise, \end{cases} \tag{4.24}$$

where $\tau_l$ is the lag time to reach 99.99% of the thrust, $\tau_\mathrm{d}$ is the delay time to reach 10.0% of the thrust, and $\tau_r$ is the final point in the linear regression. The parameters $\kappa_r$, $\zeta$, $s$, and $c_r$ are calculated as

$$s = \frac{\operatorname{arctanh}\left(f_1 \cdot 2 - 1\right) - \operatorname{arctanh}\left(q_\% \cdot 2 - 1\right)}{\left(\frac{(\tau_l+\tau_\mathrm{d})}{\tau_\mathrm{d}} - 1\right)}, \tag{4.25}$$

$$\zeta = 1 - \frac{\operatorname{arctanh}\left(q_\% \cdot 2 - 1\right)}{s}, \tag{4.26}$$

$$\kappa_r = -\frac{f_1 - f_2}{\tau_r - \tau_\mathrm{d} - \tau_l}, \tag{4.27}$$

$$c_r = f_1 - \kappa_r\left(\tau_\mathrm{d} + \tau_l\right), \tag{4.28}$$

where $q_\%$ is the percentage of maximum combustion chamber pressure when the action time $t_a$ starts and ends according to [51]. For a $q_\% = 0.1$ (typical value), the action time corresponds to 80% of the total burning time.

We assume a maximum regression value of 99.9% of the thrust ($f_1 = 0.999$), and a final value in the regressive curve of 30% ($f_2 = 0.3$). Now, $\tau_\mathrm{i}$ is defined as

$$\tau_r = t_a + 2\tau_\mathrm{d} - \left(\frac{\operatorname{arctanh}\left(2f_2 - 1\right)}{s} + \zeta\right)\tau_\mathrm{d}. \tag{4.29}$$

Example: For an ignition time $t_{ig,k} = 0$ of a single engine, $\tau_\mathrm{d} = 0.2$, $\tau_l = 0.5$, $t_a = 5$ s, the Equation (4.24) result in the thrust profile shown in Figure 4.10.

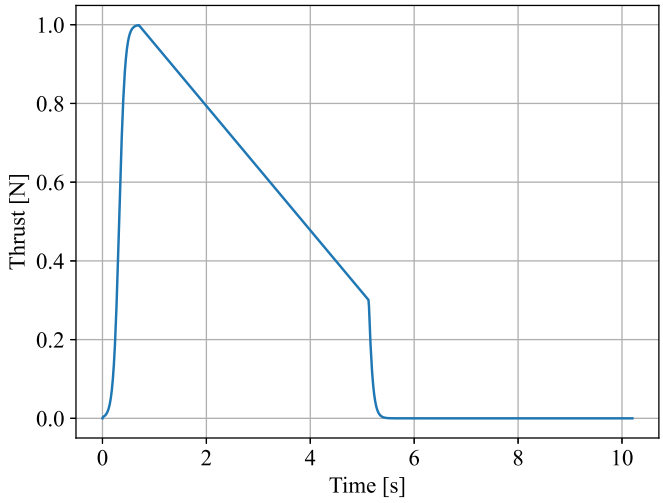


Figure 4.10: An example of regressive unitary thrust.

**PGCS-Neutral**

The neutral star grain ($\theta_{\mathrm{d}} = \theta_{neutral}$) is used because of its advantages in order to increase the initial surface area [82] and to keep a semi-constant thrust. The typical thrust profile for the star design is a backward-neutral burn area. As the burning area progresses, its surface area decreases as the outer portion of the grain expands, exposing more surface area. This trade-off yields the thrust profile depicted in Figure 4.11. The mathematical model for the unitary thrust $T_k(t - t_{\mathrm{i}g,k})/\max(T_k)$ is

$$\begin{cases} \frac{\left(1+\tanh\left(\left(\frac{t_k^*}{\tau_{\mathrm{d}}}-\zeta\right)s\right)\right)}{2} & t_k^* \leq \tau_{\mathrm{d}} + \frac{t_a}{2} \\ \frac{\left(1+\tanh\left(\left(-\frac{\left(t_k^*-t_a-2\tau_{\mathrm{d}}\right)}{\tau_{\mathrm{d}}}-\zeta\right)s\right)\right)}{2} & t_k^* \leq \tau_{\mathrm{d}} + t_a + \tau_l \\ 0 & otherwise \end{cases}. \tag{4.30}$$

**PGCS-Progressive**

For progressive solid propellant, the BATES PGCS is the most widely known shape. The whole grain is in the shape of a solid cylinder with a circular hole in the center along the cylinder. Another progressive thrust is obtained by star-progressive. The progressive thrust is shown in Figure 4.12.

The mathematical model for the unitary thrust $T_k(t - t_{\mathrm{i}g,k})/\max(T_k)$ is

$$\begin{cases} \frac{\left(1+\tanh\left(\left(\frac{t_k^*}{\tau_{\mathrm{d}}}-\zeta\right)s\right)\right)}{2} & t_k^* \leq \tau_p \\ \kappa_p t_k^* + c_p & t_k^* \leq \tau_{\mathrm{d}} + t_a - \tau_l \\ \frac{\left(1+\tanh\left(\left(-\frac{\left(t_k^*-t_a-2\tau_{\mathrm{d}}\right)}{\tau_{\mathrm{d}}}-\zeta\right)s\right)\right)}{2} & t_k^* \leq \tau_{\mathrm{d}} + t_a + \tau_l \\ 0 & otherwise \end{cases}, \tag{4.31}$$

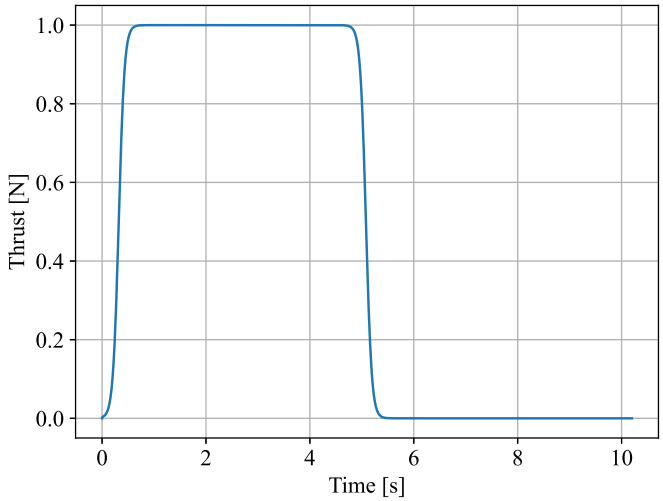


Figure 4.11: An example of neutral unitary thrust.

where $\kappa_p = -\kappa_r$, $\tau_p$ is the starting point in the linear progression. $\tau_p$ and $c_p$ are defined as

$$\tau_p = \left( \frac{\operatorname{arctanh}(2f_2 - 1)}{s} + \zeta \right) \tau_d, \tag{4.32}$$

$$c_p = f_2 - \kappa_p \tau_p. \tag{4.33}$$

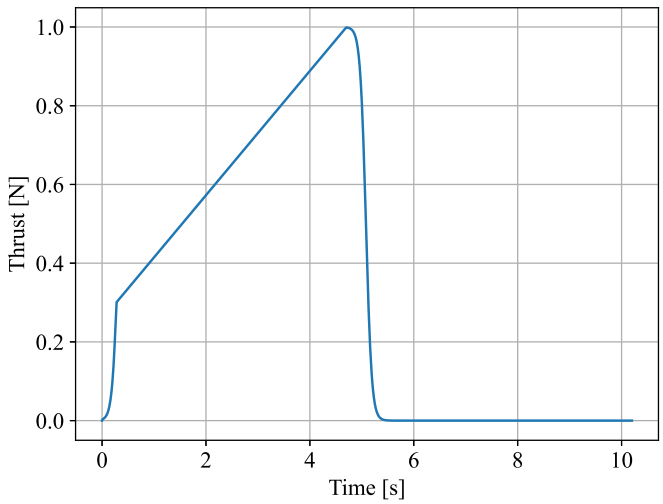


Figure 4.12: An example of progressive unitary thrust.

Now, in section 5.1 the reader will be able to see the results of the analysis in a descending dimension. These results was published in [13].

## 4.4 Plane coordinate analysis

### 4.4.1 Expansion of Mission and Requirements

Taking the results from the methodology of the Section 4.3, it is shown that an SPE array performs better when using a robustly designed control [13]. However, solving the problem of landing a module at a height of 2,000 m and passing another to an orbital landing at a height of 262 km (peri-moon equal to 2,000 km), is a more complex scenario. Among the new complexities added are:

1. The mass required by the propellant is greater than the landing from 2000 m.
2. Residual torque must be quantified and how it affects the reaction wheel flywheel design.
3. An orientation change is required to leave the orbit and then orient the module vertically.

**Point 1**

First, it is necessary to know if the required mass of propellant satisfies the restrictions in Table 3.1. To do this, we use Tsiolkovsky's rocket equation, which relates the amount of velocity desired to change with the mass needed in the process. An approximation of the speed $\Delta v$ needed to land in the worst case is calculated as,

$$\Delta v = \Delta v_{\mathrm{e}} + \Delta v_f, \tag{4.34}$$

where $\Delta v_{\mathrm{e}}$ and $\Delta v_f$ are the velocity of an elliptical orbit and the free fall velocity, respectively. For energy conservation, both are defined as

$$\Delta v_{\mathrm{e}} = \sqrt{\mu_m \left(\frac{2}{R} - \frac{1}{R_A}\right)}, \tag{4.35}$$

$$\Delta v_f = \sqrt{2\mu_m \left(\frac{1}{R_m} - \frac{1}{R}\right)}. \tag{4.36}$$

Here, $R$ is the module of the vector $\mathbf{R}^{\mathrm{i}}$, $R_m$ is the moon radius, and $R_A$ is the semi-major axis of the ellipse defined as $R_A = R_p + R_a$. The apolune $R_a$ and perilune $R_p$ are 68000 km and 2000 km, respectively ($R_A = 35000km$). The approximation of equation (4.34) considers that the module completely slows down its speed in the elliptical orbit, and then uses another thrust to slow down the speed acquired in the free-fall descent (in a straight line). This $\Delta v$ is the worst case shown in Figure 4.13a, where the maximum velocity required is 3316 m/s. Using the Tsiolkovsky equation, the approximate mass required can be calculated. This is defined as

$$\Delta v = I_{sp} \cdot g_{\mathrm{e}} \ln \frac{m_0}{m_f}; m_p = m_0 - m_f, \tag{4.37}$$

where $m_0$ and $m_f$ are the initial and final mass of the CubeSat module, respectively.

Now, for different values of $R$ belonging to the path of the ellipse, there is the graph in Figure 4.13b that show the mass required. The red line represents the limit of available

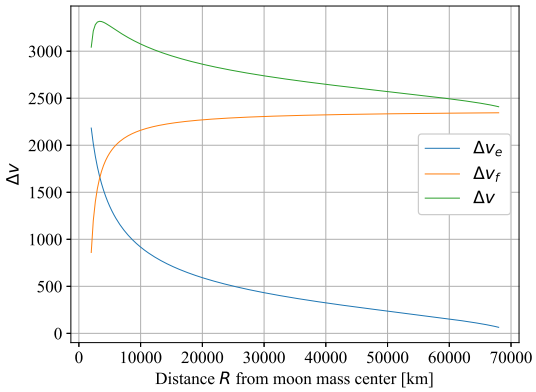


(a) Simplified case to estimate the worst case of mass required in the descent and landing of the lunar module. The required $\Delta v$ velocity is calculated for different release distances from the orbit according to the center of mass of the moon.

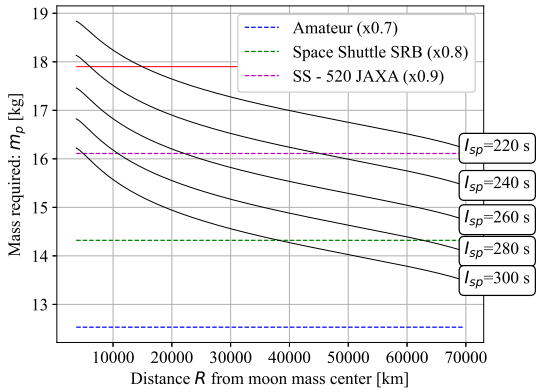


(b) Mass of propellant $m_p$ required according to the distance $R$ from center of mass for different values of $I_{sp}$ and release distances from the orbit according to the center of mass of the moon. The mass available on the CubeSat for the propellant is reduced depending on the make of the engine.

Figure 4.13: Balance of energy and mass to land a CubeSat of an orbit NRHO.

mass in our 12U CubeSat module, while the other lines represent the limit of propellant, taking into account the structural parts needed to build the assembly (ignition systems, engine casing and nozzle). This value considers the manufacturing technology used in the engines. For amateur technologies, the structural mass corresponds to 30% of the mass of the propellant $m_p$ (for conventional and small engines), therefore, the available mass $m_p$ is very low and does not intersect the values of $I_{sp}$ displayed. Using manufacturing advances such as the Space Shuttle Solid Rocket Booster (SRB) and the JAXA SS-520 sounding rocket [83], whose structural mass corresponds to 20% and 10% of the propellant respectively, the available mass limit $m_p$ is higher. This value now matches some typical $I_{sp}$ values of conventional blends. In this graph we can see that the higher the specific impulse, the lower the mass required (a characteristic that occurs in plasma thrusters, recently used in CubeSat satellite maneuvers where the mission time is long or is not a critical component since the thrust is considerably lower than an SPE).

Another important component is that the reference values that we can find in the literature, such as [53, 51] consider calculations and experiments at sea level. The selection of the propellant must consider this calculation correction, since the SPE will work in a vacuum environment (slightly increasing the $I_{sp}$). The theoretical specific impulse can be calculated as follows,

$$I_{sp} = \frac{1}{g_e} C_F C^*. \tag{4.38}$$

The specific impulse calculated for terrestrial applications is assigned as $I_{sp}^{e}$. On the other hand, it can be assumed that the design is optimal at sea level, that is, $P_e = P_a$. This mainly

affects the equation (3.18), which for an Earth mission is defined as,

$$C_F^{\mathrm{e}} = \sqrt{\frac{2\gamma^2}{\gamma-1}\left(\frac{2}{\gamma+1}\right)^{\frac{\gamma+1}{\gamma-1}}\left[1-\left(\frac{P_{\mathrm{e}}}{P_c}\right)^{\frac{\gamma-1}{\gamma}}\right]}. \tag{4.39}$$

The parameters $g_{\mathrm{e}}$ and $C^*$ remain constant for missions on earth as well as in a vacuum if it is true that the speed of the fluid at the nozzle throat is equal to the speed of sound. Then, the coefficient of thrust in vacuum ($P_a^v = 0\ atm$) $C_F^v$ is defined as

$$C_F^v = \sqrt{\frac{2\gamma^2}{\gamma-1}\left(\frac{2}{\gamma+1}\right)^{\frac{\gamma+1}{\gamma-1}}\left[1-\left(\frac{P_{\mathrm{e}}}{P_c}\right)^{\frac{\gamma-1}{\gamma}}\right]} + \frac{A_{\mathrm{e}}}{A_t}\left(\frac{P_{\mathrm{e}}}{P_c}\right). \tag{4.40}$$

Finally, the relationship between the specific impulse of ground missions at sea level and missions in vacuum, $I_{sp}^{\mathrm{e}}$ and $I_{sp}^v$ respectively, is defined as

$$\begin{aligned} I_{sp}^v &= I_{sp}^{\mathrm{e}} * \frac{C_F^v}{C_F^{\mathrm{e}}} \\ &= I_{sp}^{\mathrm{e}}\left(1 + \frac{A_{\mathrm{e}}}{A_t}\frac{P_{\mathrm{e}}}{P_c}\frac{1}{C_F^{\mathrm{e}}}\right). \end{aligned} \tag{4.41}$$

On the other hand, the output area $A_{\mathrm{e}}$ is obtained from the conservation of mass with the following expression

$$\frac{A_{\mathrm{e}}}{A_t} = \frac{\Gamma}{\sqrt{\frac{2\gamma}{\gamma-1}\left(\frac{P_{\mathrm{e}}}{P_c}\right)^{\frac{2}{\gamma}}\left[1-\left(\frac{P_{\mathrm{e}}}{P_c}\right)^{\frac{\gamma-1}{\gamma}}\right]}}. \tag{4.42}$$

Substituting the equation (4.42) in equation (4.41), the following expression is found

$$\begin{aligned} I_{sp}^v &= I_{sp}^{\mathrm{e}}\left(1 + \frac{\Gamma}{\sqrt{\frac{2\gamma}{\gamma-1}\left(\frac{P_{\mathrm{e}}}{P_c}\right)^{\frac{2}{\gamma}}\left[1-\left(\frac{P_{\mathrm{e}}}{P_c}\right)^{\frac{\gamma-1}{\gamma}}\right]}}\frac{P_{\mathrm{e}}}{P_c}\frac{1}{C_F^{\mathrm{e}}}\right) \\ \frac{I_{sp}^v}{I_{sp}^{\mathrm{e}}} &= 1 + \frac{1}{\left[1-\left(\frac{P_{\mathrm{e}}}{P_c}\right)^{\frac{\gamma-1}{\gamma}}\right]}\frac{\gamma-1}{2\gamma}. \end{aligned} \tag{4.43}$$

This equation is valid considering that the flow reaches the speed of sound at the throat of the engine forming a normal shock wave. This occurs when

$$P_{th} = P_c\left(\frac{2}{\gamma+1}\right)^{\gamma/(\gamma-1)} \tag{4.44}$$

according with Figure 3.5. Therefore, Figure 4.14 shows the ratio between $I_{sp}^v/I_{sp}^{\mathrm{e}}$ for a range of the pressure ratio $P_c/P_{\mathrm{e}}$ from 10 to 100.

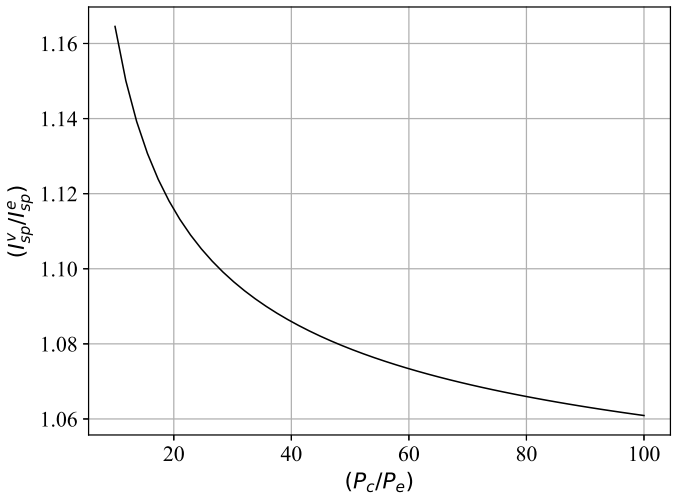


Figure 4.14: Variation of the specific impulse in vacuum according to the specific impulse calculated at sea level. It can be seen that the percentage increase is greater in low pressure rockets, that is, smaller engines.

With what is presented in this subsection, it can be seen that with a specific impulse greater than 220 s and with the development of an advanced manufacturing of the SPE combustion chamber, the mass of propellant required is within the margins of Figure 4.13b. On the other hand, if the pressure ratio of the SPEs belonging to the array is around 30 ($P_C/P_e$), an increase in $I_{sp}$ of up to 10% is expected. We can see this in the results presented by [84], from where the data to solve this work is taken. There are a variety of solid propellant fuels to use in this development. Before selecting a specific one, or taking its characteristics as references, there are some important considerations. The first of these is the ecological and safety trends in space exploration that exist today, and one of the propellants is known as "Green Propellant" [85]. This is important for interplanetary exploration, since the goal is to contaminate the places to be explored as little as possible, especially with highly toxic propellants such as hydrazine.

To use the propellant in a civil launcher, the propellant must be of hazard class 1.3 (non-detonable) and the burning rate must be adjustable in the range of 7 to 15 mm/s at 7 MPa, with a pressure exponent less than 0.5 [84]. Some examples of propellant for different configurations are presented by the author, and are shown in Table 4.1. For this work, **the properties of HTPB 1912 are used, where the specific impulse equal to 280 and a density of 1.81** $g/cm^3$ **is taken as a reference**. This propellant is not experimental and has been used in several applications. Its performance corresponds in a minimum total mass of 14.5 kg, of which approximately 8 kg correspond to orbital braking.

**Point 2**

The torques generated by the SPE arrangement are analyzed for the case of Figure 3.8, that is, two SPEs symmetrically separated and oriented in the same direction. Based on the equations (3.35) and (3.33), the residual torques of two engines are generated for different values of $\hat{d}_k$ and types of PGCS. This is seen in Figure 4.15, where the values used in the

Table 4.1: Delivered vacuum specific impulse for HTPB/Al/AP and optimized HTPB/Al/ADN/AN propellants (Vacuum specific impulse) [84].

| Propellant | Oxidizer (%) | Al (%) | HTPB (%) | $I_{sp}$ (s) | $T_c$ (K) | $\rho$ ($g/cm^3$) |
|---|---|---|---|---|---|---|
| HTPB 1912 | 69 (AP) | 19 | 12 | 280 | 3550 | 1,81 |
| ADN/AN 100/0 | 70/0 | 17 | 13 | 291 | 3395 | 1,70 |
| ADN/AN 80/20 | 53,6/13,4 | 20 | 13 | 287 | 3335 | 1,70 |
| ADN/AN 60/40 | 39/26 | 22 | 13 | 283 | 3254 | 1,70 |
| ADN/AN 50/50 | 32/32 | 23 | 13 | 281 | 3208 | 1,70 |

simulation are shown in Table 4.2.

Table 4.2: Uncertainties in SPE position to respect to center of mass.

| Parameters | Value |
|---|---|
| $\sigma_{\mathrm{d}}$ | 0.1 mm |
| $\sigma_{\alpha}$ | 0.5° |
| $t_{\mathrm{d}}$ | Unif(0, 0.5) |

Figure 4.15 shows 6 cases of residual torques generated from the aforementioned equations. Although it is not possible to see a clear pattern of distribution, the following observations can be drawn for each type of PGCS. Regarding the maximum value of the torques, this is more affected by the torsion arm $\mathrm{d}_k$ than by the type of PGCS. That is why the worst scenario occurs with $\mathrm{d}_k = 0.05m$ in the 3 types of PGCS.

- Neutral: The initial and final torque peaks have similar values, and they are opposites. On the other hand, the central area of the residual torque has a constant value close to zero in most cases.

- Progressive: Initial and final peaks differ in level due to burn-in behavior, and they are opposites. It can be seen that the initial torque is less than the final torque, and in the central zone the torque is close to zero, but it changes both backward and forward.

- Regressive: Initial and final peaks differ in level due to burn back behavior, and they are opposites. It can be seen that the initial torque is greater than the final torque, and in the central zone the torque is close to zero, but it changes both backward and forward.

From a control point of view, the progressive PGCS type appears to be more controllable (by a reaction wheel). This is because the initial torque is small at the beginning of the thrust, allowing the rest of the thrust to be applied correctly. As the highest residual torque is at the end of the burn, this could be corrected with time before starting a new thrust. However, based on the results obtained in hypothesis **H1** (shown in Figure 5.6), the progressive PGCS has a lower performance than the regressive one on the moon landing. This is why it must be solved in such a way that the solution remains optimal with respect to the soft landing.

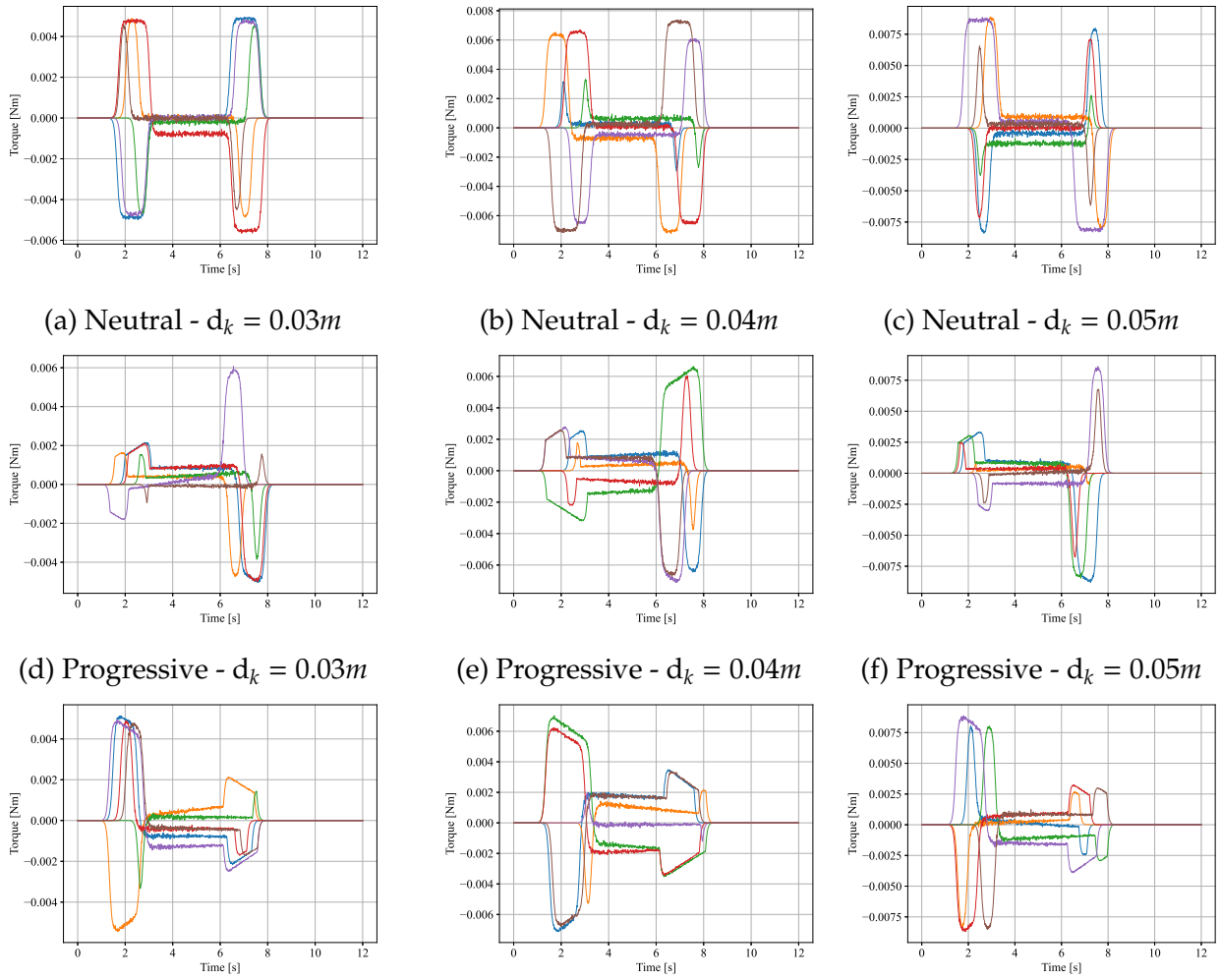


(a) Neutral - $d_k = 0.03m$ (b) Neutral - $d_k = 0.04m$ (c) Neutral - $d_k = 0.05m$

(d) Progressive - $d_k = 0.03m$ (e) Progressive - $d_k = 0.04m$ (f) Progressive - $d_k = 0.05m$

(g) Regressive - $d_k = 0.03m$ (h) Regressive - $d_k = 0.04m$ (i) Regressive - $d_k = 0.05m$

Figure 4.15: Random residual torque for different types of PGCS and distance from the center of mass $d_k$. Each graph shows 6 random torques for each configuration.

**Point 3**

To understand the problem in its final state and the critical points of ignition control and change of orientation, the landing problem is divided into 3 stages: 1) Entry, 2) Descending, and 3) landing (EDL process of the Figure 3.1).

- The first entry stage is where the module must be slowed down to leave the initial orbit and begin to decay by gravity. For this stage, the module must burn only one engine with a required initial orientation. The SPE required for this stage is the largest, and can weigh between 3 and 5 kg.

- For the second stage, the module must make a controlled descent from orbital release to close to 2,000 m. This stage is the one that presents the greatest orientation challenge, since it must rotate the module from its orbital orientation to the orientation required in the descent. Orbital orientation requires that the thrust be tangent to the orbit, whereas in descent the thrust must be parallel to the trajectory.

- For the third stage, the module is expected to be close to 2000 with a speed of less than 50 m/s. At this point, the decrease is similar to that presented in the SO1 and SO2 objectives, but considering the effects of attitude. Since the array has a larger number of motors at this stage, the residual torques are expected to be constant, and therefore the reaction wheel response must be in accordance with the requirements. A point in favor that we can find at this stage is that the mass and inertia of the module will have already decreased due to the burning of the previous SPE (from stage 1 and 2). This decrease in inertia will help make the reaction wheel response less demanding and the reaction wheel dimension smaller.

### 4.4.2 Uncertainties and Boundary Conditions

Based on the literature studied [86, 72, 21, 3], the uncertainties and requirements for the mission are grouped in Table 4.4, and 4.3, respectively. According to the uncertainties and the action plan to carry out the control mission, the information presented in Figure 4.16 is regrouped. It can be seen that initially the mission starts from an elliptical orbit with uncertainties of 100 meters with respect to the nominal orbit, and for the speed an error of 10 m/s. Then, an ignition begins that makes it descend in free fall with a tangential speed close to zero (desirable). The error in the descent stage is 50 m in position, and 5 m/s in speed. Once an altitude close to 2000 m is reached, the main engine burns out, which will slow down a large part of the free fall speed. Subsequently, comes the soft landing stage. At this point the height error decreases drastically to 0.1 m thanks to the relative sensors that exist. Likewise, the speed error decreases to 0.5 m/s. In this last stage the remaining engines will be activated to make the soft landing.

Table 4.3: Placeholder Touchdown conditions.

| Parameters | Value |
|---|---|
| Error of position landing $\|\|\vec{e}\|\|$ | $> 10$ [$m$] |
| Error landing velocity $\|\|\vec{e}\|\|$ | $> 0.5$ [$m/s$] |
| Horizontal landing velocity | $> 0.5$ [$m/s$] |
| Error of angular orientation | $> 1$ [deg] |
| Error of angular rate | $> 5$ [deg] |

Table 4.4: Parameters with uncertainties.

| Parameters | Value | Details |
|---|---|---|
| $\sigma_{pos}$ | 100, 50, 0.1 $m$ | The standard deviation of position for the First, Second, and for the Third stage |
| $\sigma_{vel}$ | 10, 5, 0.5 $m/s$ | The standard deviation of velocity for the First, Second, and for the Third stage |
| $I_{sp} : \sigma_{bias}$ | (10% at $3\sigma$) | Bias in specific impulse |
| $I_{sp} : \sigma_{noise}$ | (3% at $3\sigma$) | Noise in the specific impulse |
| $\tau_{\mathrm{d}}$ | 0.2 $s$ | Thrust dead time of each motor |
| $\tau_l$ | 0.5 $s$ | Thrust lag time of each motor |
| $\sigma_{\mathrm{d}}$ | 0.1 mm | The standard deviation of engine position |
| $\sigma_\alpha$ | 0.5° | The standard deviation of engine pointing |
| $t_{\mathrm{d}}$ | Unif(0, 0.5) | Ignition dead time (for electrical signal) |

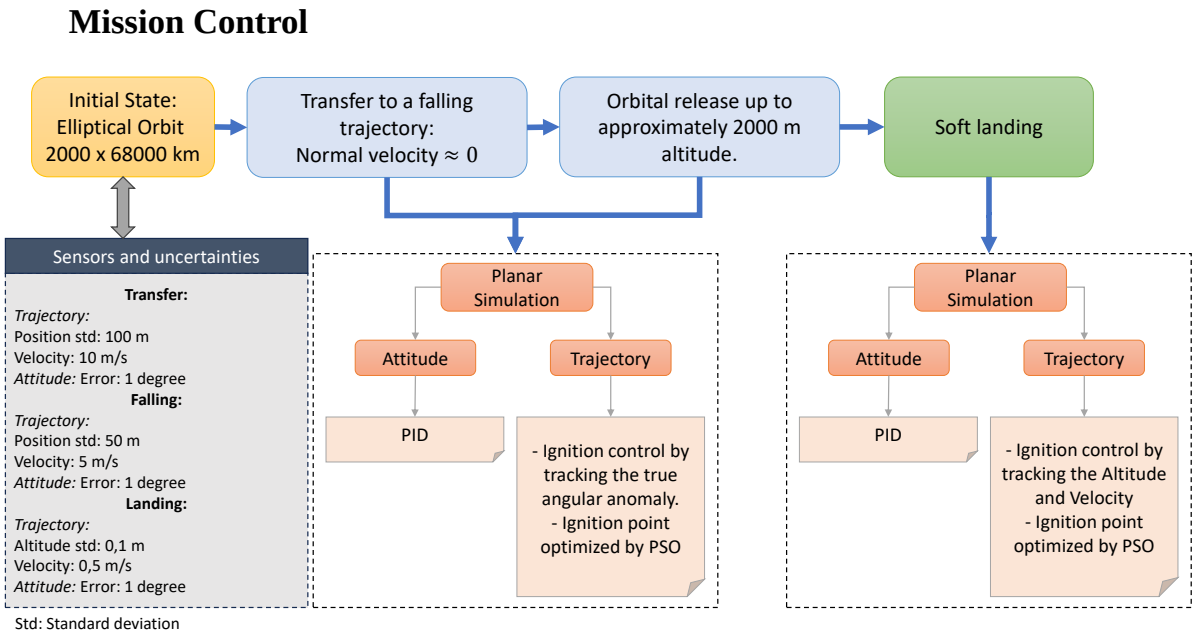


Figure 4.16: General mission stages with state errors in each process.

### 4.4.3 Optimization and Control Design

The optimal control design is separated into 2 studies. The first of them contemplates the optimization of the first and second landing stages (Entry and Descending stage), and the second contemplates the soft and vertical landing stage (landing stage). The concept for the first study is detailed in Figure 4.17, where all possible descent configuration combinations can be seen. That is, explore whether braking will be better for a forward, backward, or neutral PGCS, and at which orbital locus the burn should be initiated. After this, the module must change its orientation to vertical and explore the next configuration of the SPE, and a new position and speed of burning. This exploration allows to optimize the base configuration and is solved with the use of the PSO algorithm. The same process is then applied to the final stage of landing.

Unlike the control function presented in section 2.2.1 by [13], we propose as future work a function of the ANN type. This idea is based on the concept presented in Figure 4.18, where the use of an ANN can be better adjusted to the soft landing requirements, increasing the flexibility of the ignition point of each engine.

The flexibility is associated with the type of actuator, such as an SPE. These engines only have one ignition point, if a control condition is not satisfied there is no other option to start it. These have a defined thrust and burn time prior to flight, but that may vary slightly due to environmental conditions. Together with these variations, uncertainties about state parameters such as position and speed are added, therefore, it is more feasible to miss the ideal ignition point. The focus of this work is to work on a line where the ignition point is a control function that covers a larger domain, as presented in [13]. But this still has room for improvement, and that is why an Artificial Neural Network is proposed as the control function of each engine. On the other hand, the method presented in [87, 88]

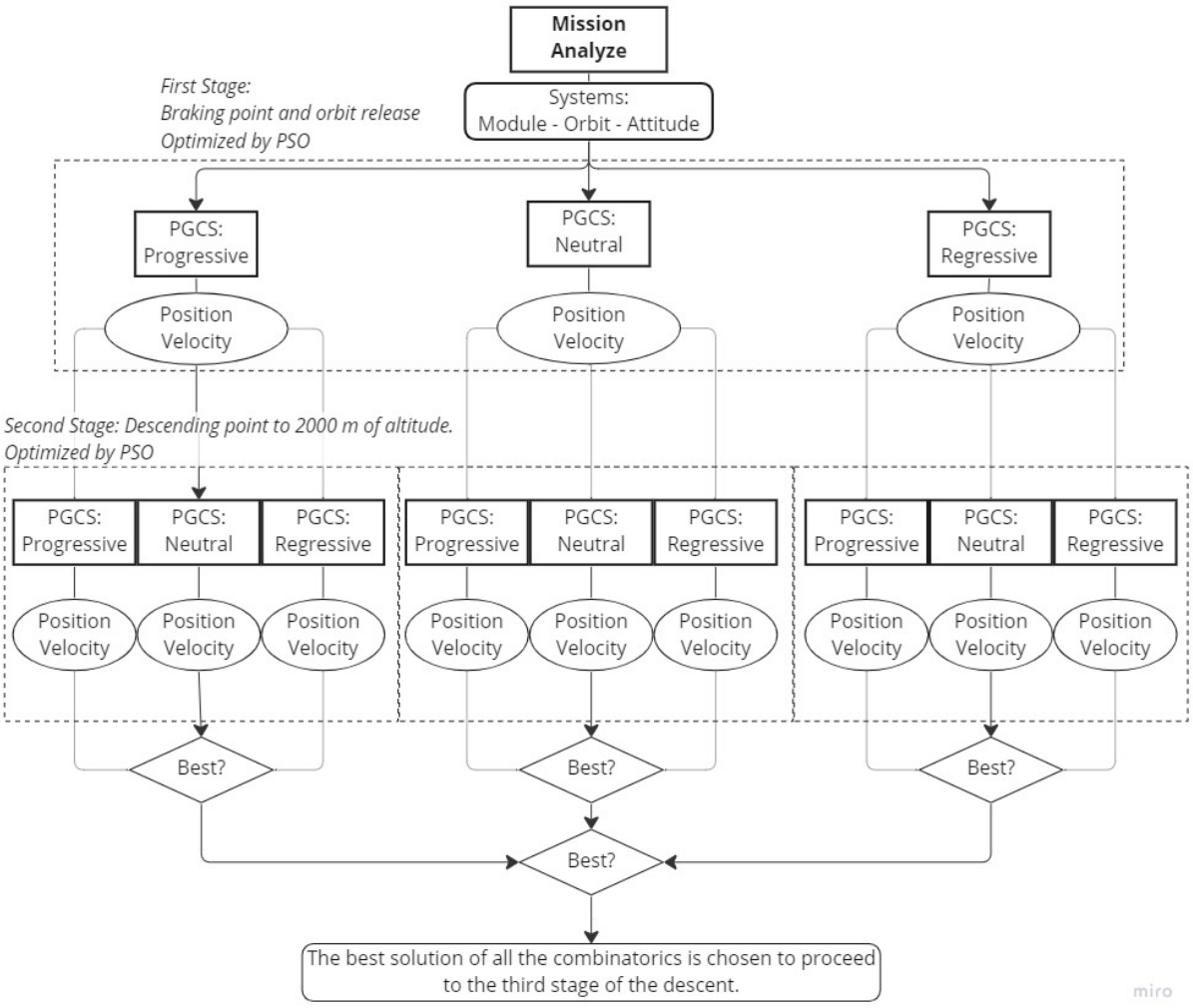


Figure 4.17: The Figure shows the optimization formulation of the PGCS type and the ignition points for the three landing stages: Orbital braking and release, and Descent stage up to 2000 m (Where the 3rd landing stage begins). The optimization is performed based on the error between the final landing state and the target state, associated with a soft landing. On the other hand, consider minimizing the mass used in the descent of these first two stages.

applied sparsity techniques to decrease the dimension of the matrices using regulators, which is an important key in space missions that require decrease the complexity of control functions.

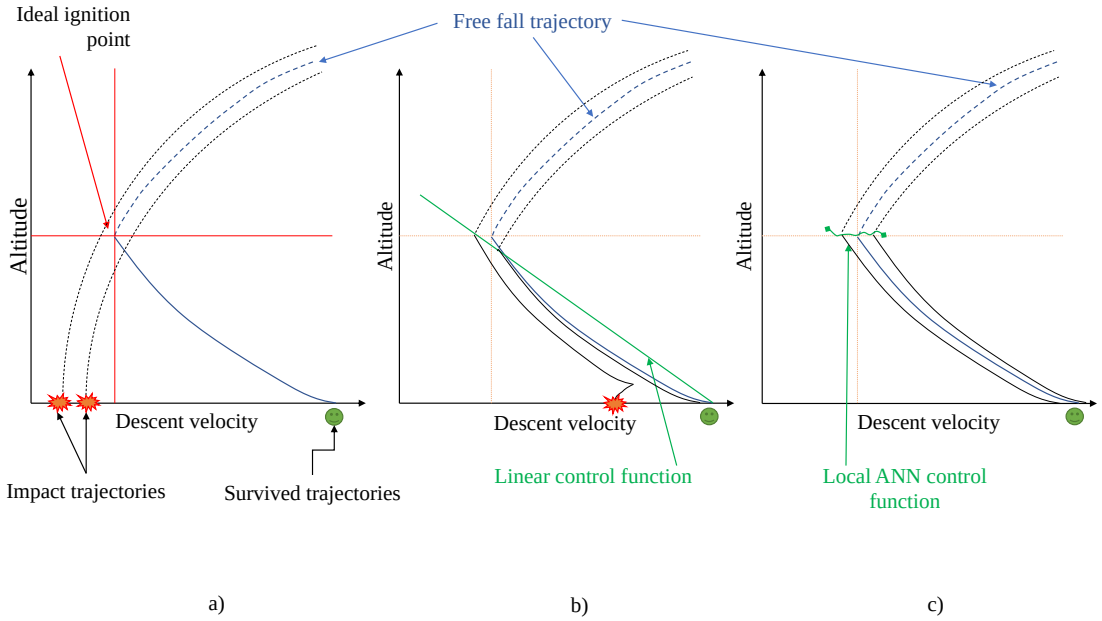


Figure 4.18: Landing process with one Solid propellant engine, showing that the robust optimization tackles the problem of the uncertainties in the trajectories. Figure a) shows an ideal optimization (without uncertainties) that has only one point of ignition, any trajectory that is not ideal will impact the surface. Figure B) shows the linear control function present in [13], which is calculated from a population of trajectories controlled by the same control function, this allows more trajectories to survive (more flexible control). Figure C) shows an ANN proposed as future work and that is the control function. This is not limited to a linear function and can explore more dimensions of the function in a local area.

Now, the main concept aimed at is to use the PSO algorithm to find the ignition point of each motor and its trajectories and save the control activation. The present proposed step by step solution is:

1. Create $N_p$ different trajectories from a normal random noise uncertainties in position and velocity. Each trajectory is a module that has $N_e$ numbers of engines.

2. For each trajectory, search the best position of ignition point and the PGCS configuration of the engine with PSO algorithm.

3. Save the position $\vec{R}$, velocity $\dot{\vec{R}}$, mass $m$, the orientation $\theta$, and the angular velocity $\dot{\theta}$ at the moment that each engine ignited to create a set of data for training $\mathcal{X}, \mathcal{Y}$. This data set is created for each engine of the module and for each trajectory, and it is defined as the algorithm 1, where $\beta$ is the ignition variable control. $\beta = 1$ if the ignition results in a soft-landing trajectory, and $\beta = 0$ otherwise. $\hat{\beta}$ is a measure of the dispersion associated to the desired landing trajectory (for each engine), and it is defined as

$$\hat{\beta}_i^p = \sigma((\beta)_i^p). \tag{4.45}$$

with $\tilde{x}$ defined as error state $\tilde{x} = [\vec{e}, \dot{\vec{e}}]$. The error of the state are defined as $\vec{e} = \vec{R}_{target} - \vec{R}(t)$, and $\dot{\vec{e}} = \dot{\vec{R}}_{target} - \dot{\vec{R}}(t)$. $\sigma$ is the standard deviation operator of the vector

state $\tilde{x}$ (This formulation could be modified to improve the importance of $\hat{\beta}$).

4. Training the proposed ANN with the dataset created by PSO.

**Algorithm 1** Optimization process to create the data set needed to train the ANN

**Require:** $N_p$ Initial population
**Ensure:** $\vec{R}_{target} - \vec{R} < 10[m]$
**Ensure:** $\dot{\vec{R}}_{target} - \dot{\vec{R}} < 0.5[m]$
  $\mathcal{X} = []$
  $\mathcal{Y} = []$
  **for** $p \rightarrow N_p$ **do**
    **for** i $\rightarrow N_e$ **do**

$$\mathcal{X}_i^p \rightarrow \begin{bmatrix} \vec{R} \\ \dot{\vec{R}} \\ m \\ \theta \\ \dot{\theta} \end{bmatrix}_i^p \sim \mathcal{Y}_i^p \rightarrow \begin{bmatrix} \hat{\beta} \\ \beta \end{bmatrix}_i^p$$

    **end for**
    $\mathcal{X}.append(\mathcal{X}_i^p)$
    $\mathcal{Y}.append(\mathcal{Y}_i^p)$
  **end for**

Using training data from each SPE, the landing control system is complemented by a PID controller to drive the reaction wheel. The complete control process is shown in the example diagram in Figure 4.19.

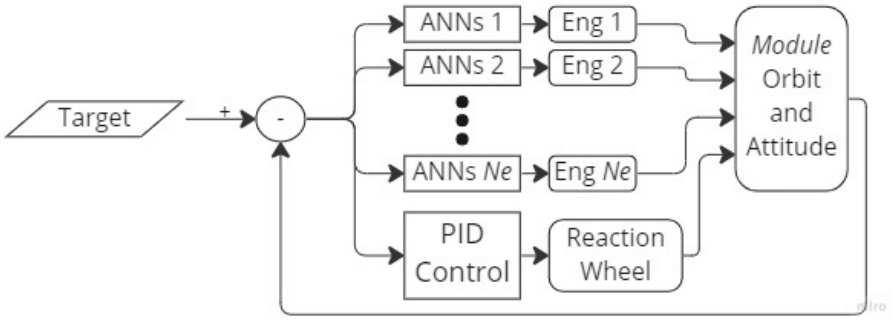


Figure 4.19: Block diagram of the final operation of the ignition control system. The ANNs of each engine are independent so as not to affect the system in case an SPE fails, or one wants to replace one with different properties. The $\mathcal{X}$, $\mathcal{Y}$ data set should be used relative to the target values.

Regarding the training data, it is expected to find an ANN that resolves the ignition points in a range of state space as shown Figure 4.18. In this case, if the trajectory never passed through the ignition zone, then it will fail. If it passes through the ignition zone, then the module has an opportunity to continue attempting a soft landing with the next engine.

### 4.4.4 Simulation Framework

For this development, the dynamics and knowledge we have of the models are expanded. That is why to carry out the simulation it is proposed to create a pseudo simulator that involves the transition of the Dynamics, the propagation of the Module states, and the propagation and updating of the SPE state. The general simulation flow of the system to be solved is shown in Figure 4.20. The entire simulation framework is based on python.

Details of the main elements are defined below.

- Core: The core is the central part of the simulator that functions as the user interface. By defining variables, the user can change the orbit types, simulation times, and the parameters of the evolutionary methods used. This element is the interconnection between the module simulations and the mathematical tools.

- Module: The module is a class that represents the lander, contains its characteristics, and manages time propagation. The propagation is carried out for each instance of the class separately, and during the cycle calls are made to the control and the measurement of the states. In the same way, this module is the one that sends the activation signal to the thusters.

- Dynamics: This class is responsible for managing and propagating the module states. The class is fed with mathematical tools, such as Runge Kutta, to give rise to the simulation. Each module created from the Module.py class has an instance of the Dynamics.py class, which allows the historical data of each Module to be saved separately.

- Thrust: This class is responsible for simulating the thrust of the SPEs. The propellant

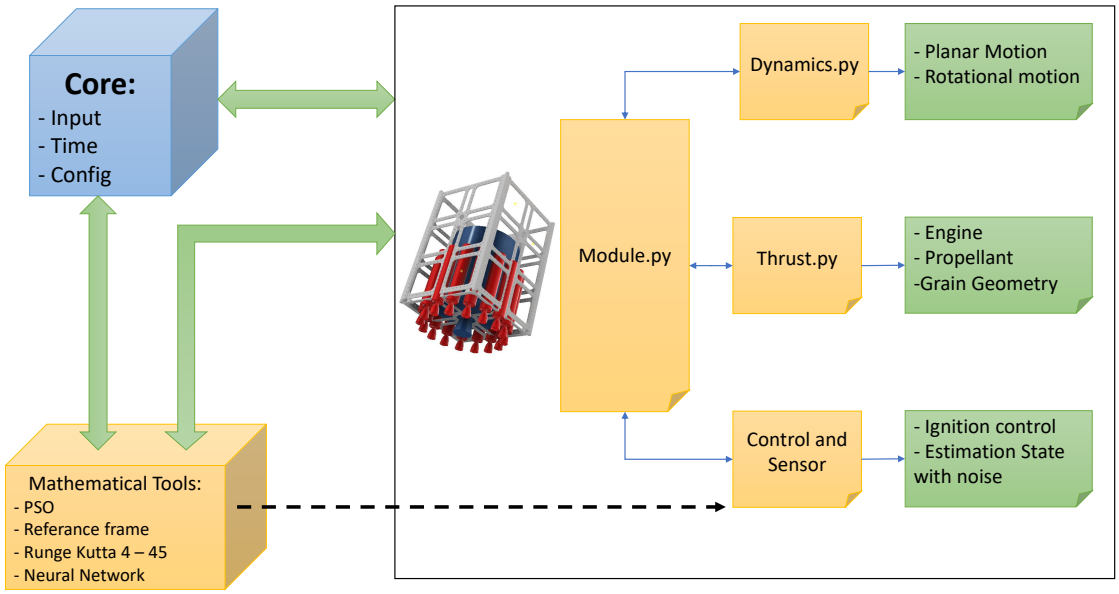


Figure 4.20: Simulator framework outline. The interconnection of the main classes and tools used in this work is shown.

class can be selected to work based on a mathematical model (as proposed in section 4.3.4), through input data, or through the rocket and propellant equations in section 3.1.3. In addition, it contains a class of the base type that is responsible for simulating the random ignition dead times for each instance of the engine created.

- Control and Sensor: These functions are part of the module class and are defined by the user. For control, you can define specific ignitions that depend on the position and angular displacement, or define to activate the neural network that will be trained in this work. To simulate the sensing, the error defined in section 4.4.2 is added to the nominal states.

- Math Tools: This tool works as an almanac of useful functions for any dynamic problem. Some of them are coordinate changes, rotations, etc. In addition, it contains the base structure of integrators such as Runge-Kutta 4 (RK 4), and Runge–Kutta–Fehlberg 4(5) (RK 4(5)).

It is important to note that the default simulation uses the RK 4(5) integration method, but every time the SPEs are activated it changes to a fine step with RK 4. On the other hand, all trajectory simulations are optimized independent of orientation, where

$$\hat{\mathbf{u}}_k^{\mathrm{i}} = -\frac{\dot{\mathbf{R}}^{\mathrm{i}}}{|\dot{\mathbf{R}}^{\mathrm{i}}|}. \tag{4.46}$$

In a subsequent analysis, the conditions that this imposes on orientation control will be extracted.

## 4.5 Mechanical considerations

### 4.5.1 Disposition

The preliminary mechanical arrangement of each SPE is shown in Figure 4.21. It shows the arrangement of SPEs with the tentative distances of each engine with respect to the center of mass. Two of the black motors will be used for Entry simultaneously. The large red motor and the remaining 2 black ones will be used to brake the module on the Descent. Finally, each pair of golden engines will be used for soft landing. An attempt is made to reduce the diameters to a minimum to avoid residual torques that are too large.

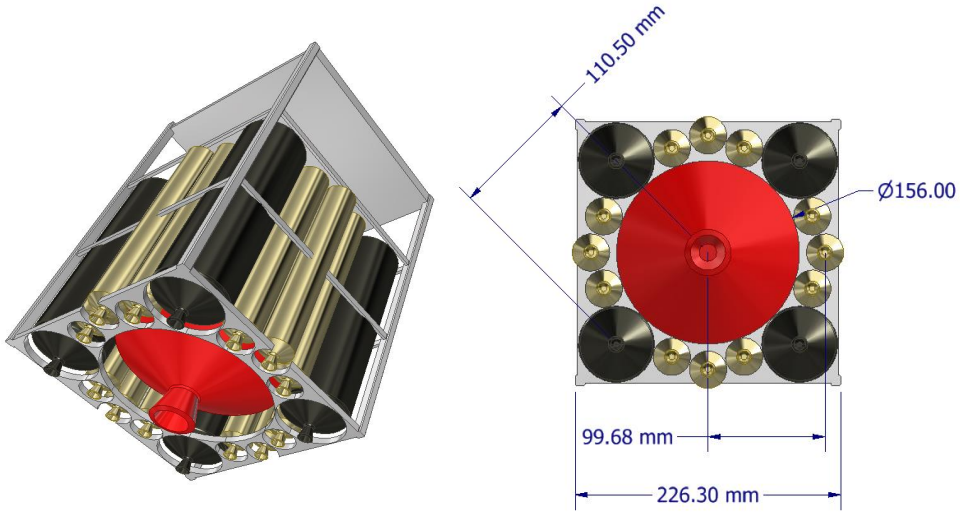


Figure 4.21: Preliminary design of SPEs arrangement with the tentative distances of each engine from the center of mass. The dimensions of the SPEs are not final.

### 4.5.2 Structural

Depending on the diameter and length configuration of the motors, they must withstand the maximum propellant pressure. As an example, simulations of mechanical stress at pressure levels expected in the process are shown. The graphs in Figures 4.22a and 4.22b show thrust curves for a progressive and neutral engine. Figures 4.23a and 4.23b show the pressures of the combustion chamber, where the maximum pressures of each of them are around 9 MPa and 6 MPa, respectively.

A preliminary design of the engines was made using CAD to simulate the pressure inside and calculate the safety factor of the design. The material used is 440 C stainless steel. The result of the progressive type motor is shown in Figure 4.22a. On the other hand, the result of the neutral motor is shown in Figure 4.25.

As can be seen in Figure 4.24, there are points that have safety factors of 1.3 and that implies that they will withstand the pressures. However, it is recommended to perform a transient analysis to see thermal and pressure transient effects. This may require a higher base safety factor (recommended >2). However, in Figure 4.25 all the safety factors of

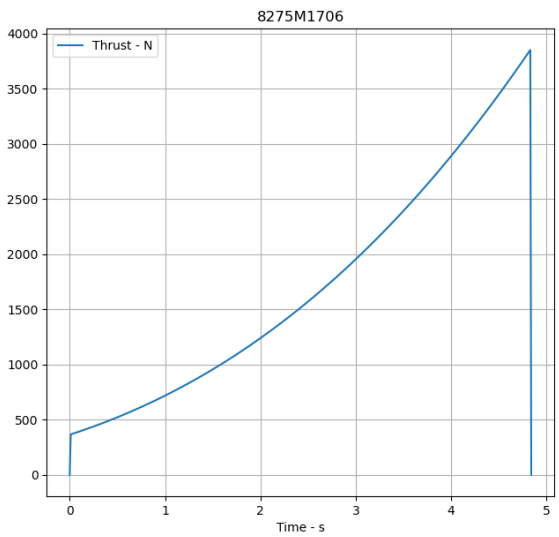


(a) Simulation of main Engines 10 MPa

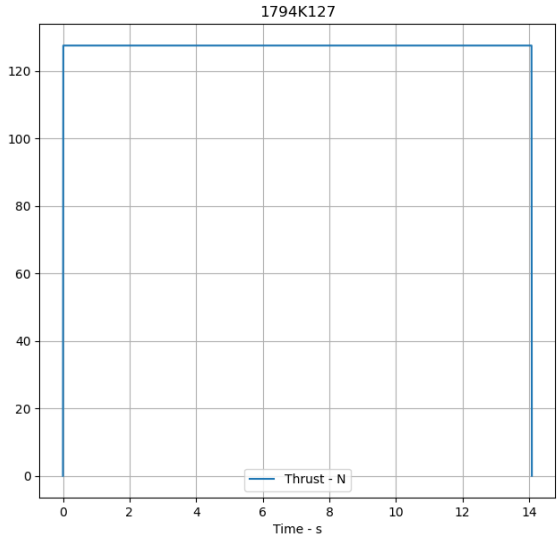


(b) Simulation of main Engines 7 MPa

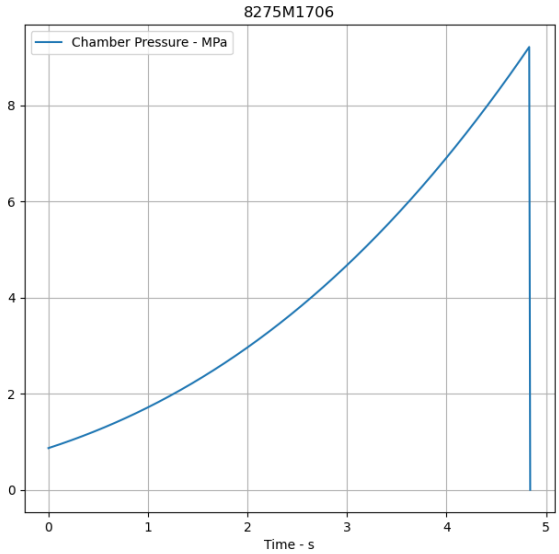


(a) Simulation of main Engines 10 MPa

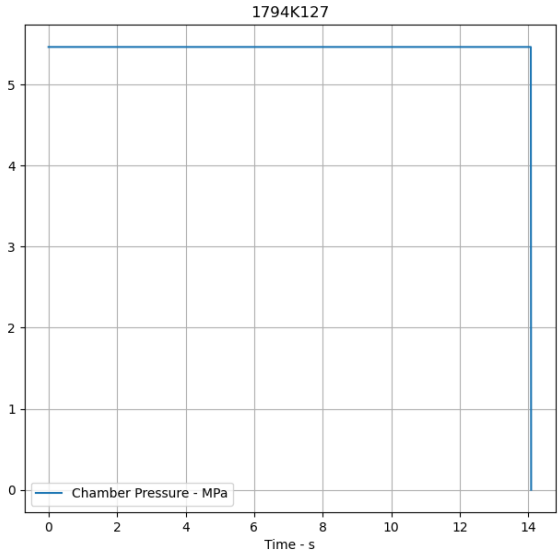


(b) Simulation of main Engines 7 MPa

the motor are greater than 2. This opens up a whole process of development, design and manufacturing of optimized motors, which could reduce the mass to a minimum.

### 4.5.3 Engine design

From the theory of rocket engines, necessary conditions arise for the operation of the engine to achieve the best performance. A well-known example of this is the diameter of the nozzle, which must reach the sonic velocity with a normal shock wave. This condition comes from equation (4.44), which relates the pressure of the nozzle with respect to the pressure in the combustion chamber, that is, the pressures of Figures 4.23a and 4.23b. Once the shock wave is reached in the throat, the system is not affected by the physical phenomena that are happening downstream. Therefore, increasing the pressure in the combustion chamber, as progressive burning does, only affects the throat. This is

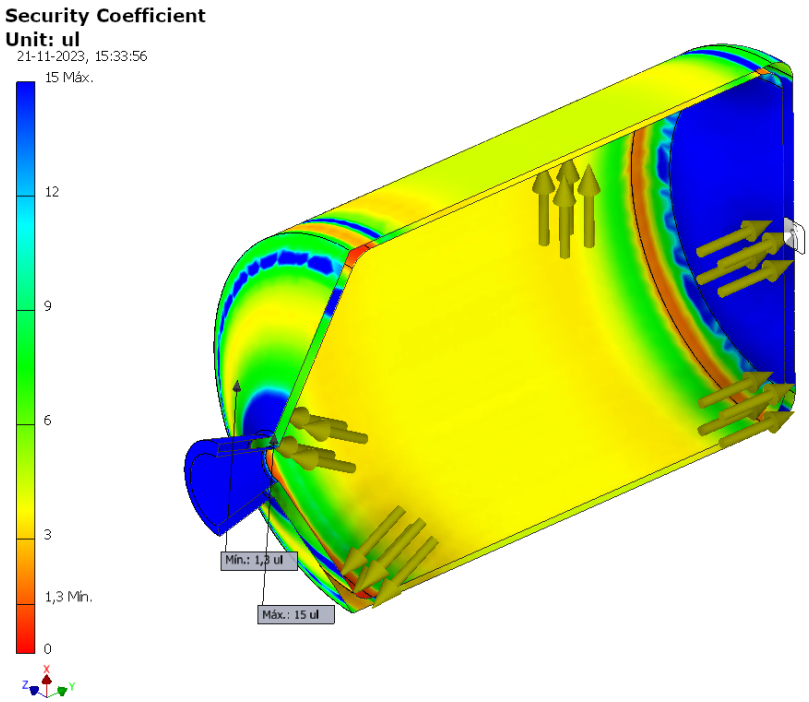


Figure 4.24: Simulation of main Engines with an internal pressure of 10 MPa. The propellant mass is 6.11 kg, and the engine case mass is 3.975 kg.

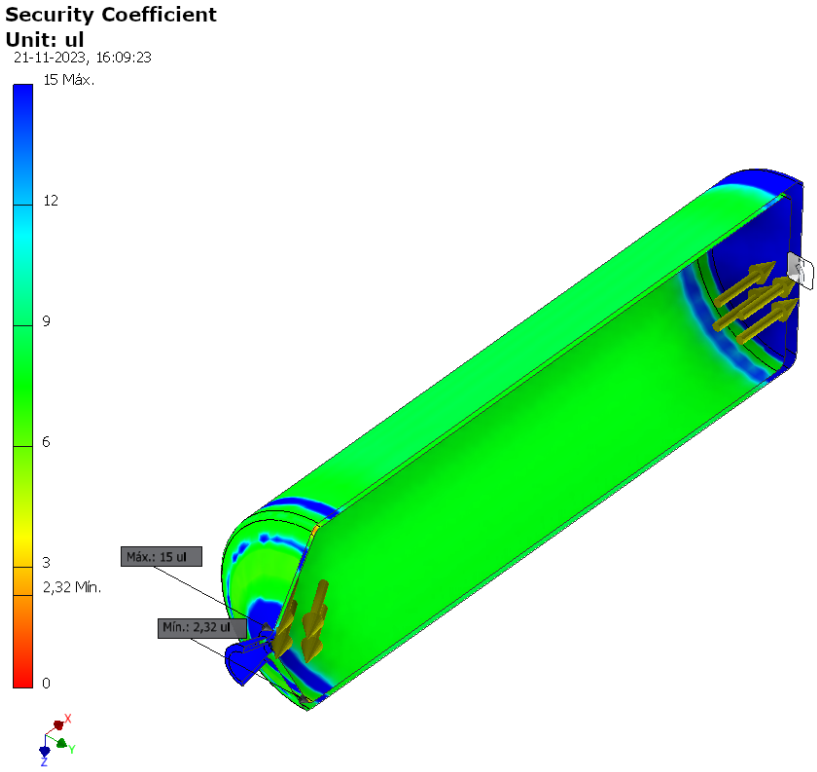


Figure 4.25: Simulation of main Engines with an internal pressure of 7 MPa. The propellant mass is 1.05 kg, and the engine case mass is 0.805 kg.

important, since the exploratory optimization analysis of this work seeks to reduce the mass of propellant used. Since the evolutionary algorithm will search for the ignition point with different propellant lengths and diameters, the throat diameter with the best performance must be recalculated for each possible solution.

From the above, the important thing is to calculate the initial pressure that the propellant will generate in a stable state. For this we consider the variation of the equation 3.16 equal to zero, resulting in

$$P_c = \left[ \frac{A_b}{A_t} \frac{a(\rho_p - \rho_g)}{\Gamma / \sqrt{\mathbb{R}T_c}} \right]^{1/(1-n)} . \tag{4.47}$$

This equation indicates that the smaller the diameter of the throat (smaller throat area $A_t$), the pressure is greater, and the thrust is greater. However, if the pressure is higher, the mass of the motor casing increases significantly when the pressure reaches 10 MPa. According to Adde Y. et al. [89], a parameter $K_n = A_b/A_t$ can be defined which relates the mass generated inside the combustion chamber, and that which can exit through the throat. Experimentally, it has been found that values of $K_n$ greater than 2 provide desired performance. Depending on the technology and desired thrust levels, this can go up to 220. Then, considering a maximum pressure restriction of 7MPa, the engine design has the following condition depending on whether it is the solution candidate of the evolutionary algorithm,

$$At = \frac{A_b}{K_n}, \text{ such that, } \max_{K_n \in (2,220)} P_c = \left[ K_n \frac{a(\rho_p - \rho_g)}{\Gamma / \sqrt{\mathbb{R}T_c}} \right]^{1/(1-n)} \text{ with } P_c < 7MPa. \tag{4.48}$$

The higher $K_n$ value is, the higher the pressure will be, and the more mass the casing will have to have. In this way, in this work $K_n$ is optimized between [0 - 150]. On the other hand, by limiting the value of $K_n$, the value of the maximum combustion pressure is also limited. This helps to reduce the thrust of the engines and therefore, the maximum residual torques.

# 5. Simulation and Results

## 5.1 One Dimensional Simulation

Based on the case studies, the simulations are separated into two evaluation scenarios using the Monte Carlo method: one that evaluates the first approach, and a second that evaluates the trajectories with the second approach. As both cases must be evaluated, we regroup the simulation data in the Table 5.1, which is also used in the optimization of the scenario with uncertainties. The altitude and velocity states are selected according to the final stage of soft-landing process, such as mentioned by [39, 86, 29]. The optimization parameters are shown in Table 5.2, where the limits of the mass flows of each individual are calculated as follows:

$$\dot{m}_{min} = \frac{|g|m_0}{v_e k}, \; \dot{m}_{max} = \frac{2\dot{m}_*}{k}, \; k = 1, \cdots, N_e, \tag{5.1}$$

where $\dot{m}_*$ is the theoretical optimal mass flow obtained from Pontryagin's principle for a constant thrust and action time [37, 38]. For simplicity, the action time used in $\dot{m}_*$ is equal to the mean between the min $(t_{a,k})$ and max $(t_{a,k})$, which is equal to 10.5 s. As expressed in the Equation (5.1), the mass flows must be updated according to the number $k$ of engines in the array.

Table 5.1: Simulation parameters.

| Parameters | Value |
|---|---|
| $y_0$ | 2000 m |
| $v_0$ | 0 m/s |
| $\sigma_{alt}$ | 50 m |
| $\sigma_{vel}$ | 5 m/s |
| $I_{sp}$ | 300 s |
| $\sigma_{bias}$ | 10.83 s (10% at $3\sigma$) |
| $\sigma_{noise}$ | 3.25 s (3% at $3\sigma$) |
| $m_0$ | 24 kg |
| $g$ Acceleration of the moon | 1.67 [m/s$^2$] |
| $\Delta t$ of simulation | 0.1 s |
| Numerical method | Runge-Kutta 4th Order |
| $\tau_d$ | 0.2 s |
| $\tau_l$ | 0.5 s |

Table 5.2: Optimization parameters.

| Parameters | Value |
|---|---|
| $N_e$ | 10 |
| $N_{case}$ | 30 in trained |
| $R_a, R_b, R_c$ | 0.1, 1.0, 10.0 |
| $b_1, b_2$ | 1.0, 1.0 |
| $\alpha_k$ | $\in [0.0, 1.0]$ |
| $\gamma_k$ | $\in [0.0, \gamma_{max}]$ |
| $t_{a,k}$ | $\in [1.0, 20.0]$ s |
| $\dot{m}$ | $\in [\dot{m}_{min}, \dot{m}_{max}]$ |
| Probability of mutation | 0.25 |
| Number of individuals | 40 |
| Number of generations | 300 |
| *center* | 0.7 |

The limits of the $\alpha_k$ and $\gamma_k$ control parameters are selected based on the dynamic model and the linear function defined in the plane. The limits of $\alpha_k$ were chosen between 0 and 1 to normalize one of the parameters of the linear function. On the other hand, for any speed and altitude value, the control function must cut the height axis between the initial speed $y_0$ and the final speed $y_{land}$. To understand the relationship that exists between the control variables, it is useful to express the Equation (4.12) as,

$$y(t) = -\frac{\gamma_k}{\alpha_k} v(t) \tag{5.2}$$

where we can see that if $\alpha_k$ is small, the slope tends to infinity. To counter this, the value of $\gamma_k$ must also tend to zero. Then, the minimum value of $\gamma_k$ is zero.

The worst-case scenario is when $\alpha_k$ stagnates at its maximum value, where the slope only depends on $\gamma_k$. If this value is not high enough, the maximum slope will not be able to reach optimal ranges. However, if it is too high, it could take a long time for GA to find an optimal solution. To satisfy these two points, we define that the control line must pass through the point that contains the initial altitude and the final velocity in free fall. In this way, the maximum value of $\gamma_k$ is defined as follows.

$$\gamma_{max} = \frac{y_0}{\sqrt{v_0^2 + 2|g|y_0}}. \tag{5.3}$$

This analysis is performed with a simulator developed in Python, which is available in the Space Exploration and Planetary Laboratory (SPEL) repository (`https://github.com/spel-uchile/SolidPropellantforLanding` (accessed on 20 September 2022)).

### 5.1.1 Optimization and Evaluation of First Approach

In this section, the best result obtained with the DCF approach in the scenario of the Section 4.3.2 is present. These optimal parameters are evaluated in a scenario with all the

mentioned uncertainties. In this evaluation, it is possible to differentiate the point with the lowest impact velocity, resulting in the control and optimization parameters shown in Tables 5.3 and 5.4 for Regressive PGCS.

The behavior of the altitude and the velocity of the lander are shown in Figure 5.1, while the distribution is shown in Figure 5.2. Here, it is possible to see that the impact velocity is −5.87 m/s with a standard deviation of 2.49 m/s. Additionally, the green and red circles in Figure 5.1 represent the ignition time and the shutdown time of each engine, respectively.

Table 5.3: Design parameters of the best result obtained from the optimization scenario without uncertainties.

| **Parameters** | **Value** |
|---|---|
| PGCS | Regressive |
| $N_e$ | 9 |
| $\dot{m}$ | 14.15 $times$ $10^{-3}$ kg/s |
| $t_a$ | 15.75 s |
| $v_{land}$ | −5.87 m/s |
| Std Dev. of $v_{land}$ | 2.49 m/s |
| Mass used | 1.51 kg |

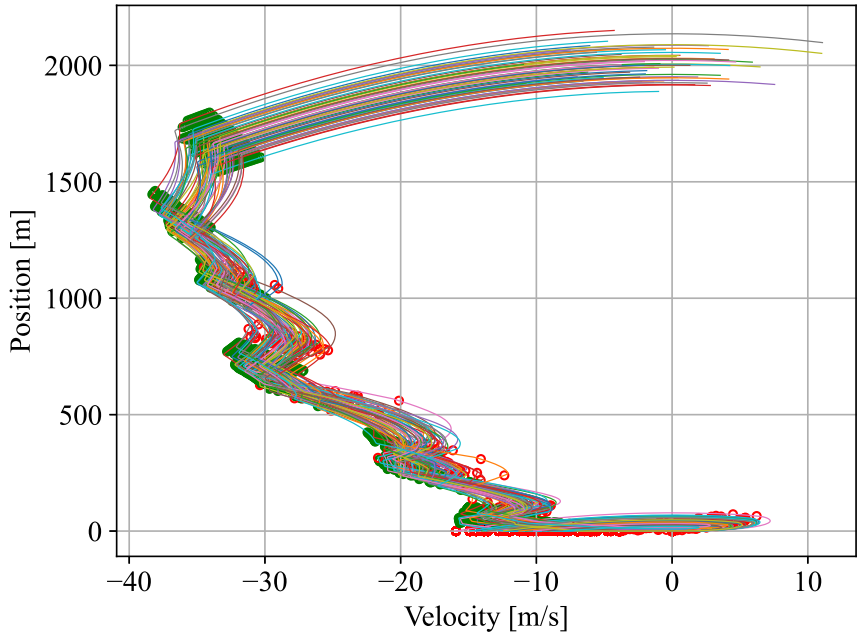


Figure 5.1: Behavior of altitude and velocity in the evaluation of the best individual $\mathcal{G}$ obtained from the optimization without uncertainties in training. The SPEs array has $N_e = 9$ and Regressive PGCS. Color map is used to differentiate different random trajectories.

In Figure 5.3, we present the performance for different numbers of engines and PGCS. Although the result shows a certain pattern to improve the landing process, it has an undefined pattern for a certain number of engines and type of PGCS. On the other hand, the standard deviation of the results does not decrease as a function of the number of engines. This randomness is one of the main reasons why it is necessary to use the method presented in Section 4.3.3. These results are presented in the next subsection.

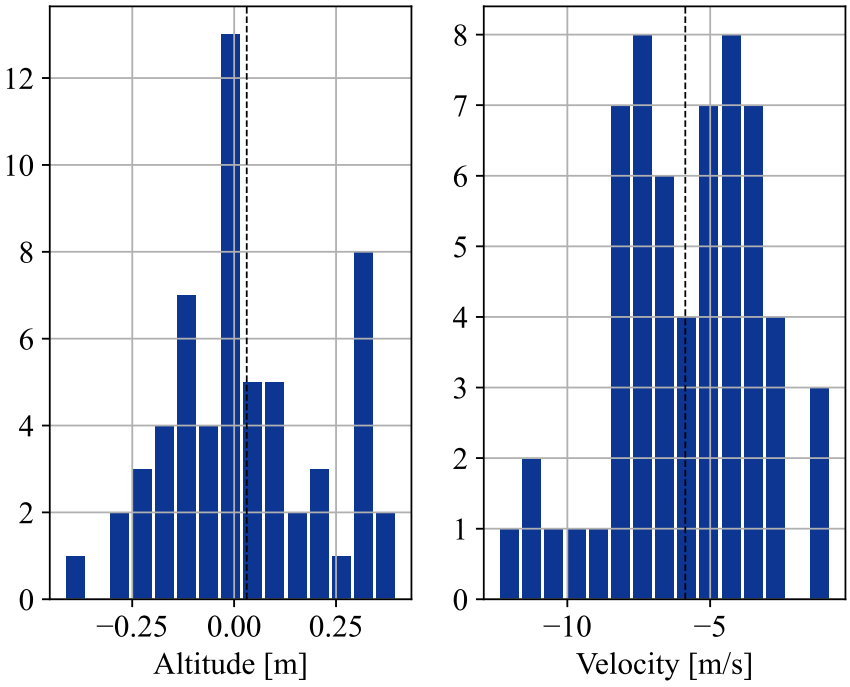


Figure 5.2: Distribution of altitude and velocity landing in the evaluation of the best result obtained from the optimization without uncertainties in training. The SPEs array has $N_e = 9$ and Regressive PGCS. The vertical axis shows the frequency of the values.

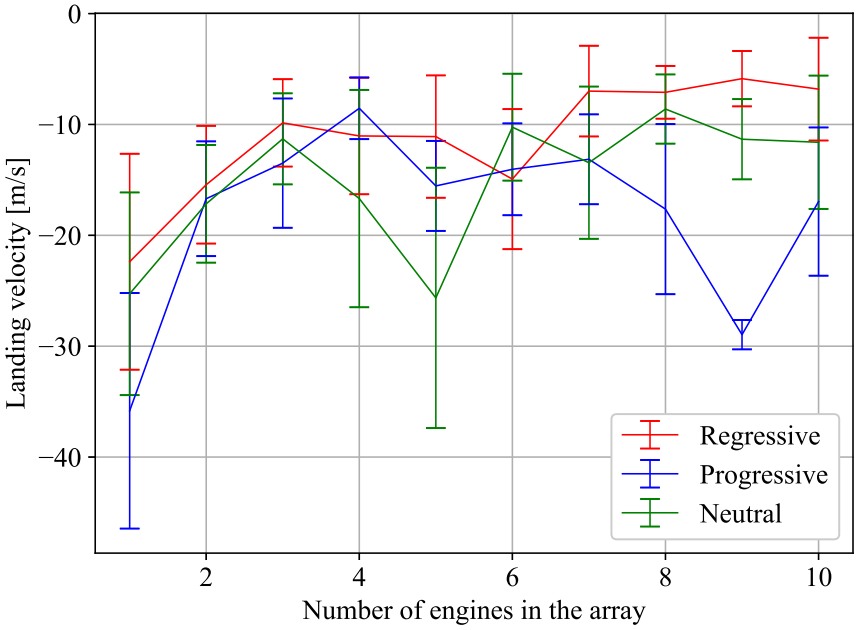


Figure 5.3: First approach: performance comparison for an array between 1 and 10 configuration engines, and for the three types of PGCS: Regressive, Neutral and Progressive.

Table 5.4: Control parameters from the best result obtained in the scenario without optimization uncertainties. The SPEs array has $N_e = 9$ and Regressive PGCS.

| $k$ | $\alpha_k$ | $\gamma_k$ |
|---|---|---|
| 1 | 0.511 | 3.632 |
| 2 | 0.992 | 4.393 |
| 3 | 0.300 | 10.071 |
| 4 | 0.755 | 19.199 |
| 5 | 0.531 | 20.431 |
| 6 | 0.795 | 11.292 |
| 7 | 0.560 | 17.099 |
| 8 | 0.323 | 8.667 |
| 9 | 0.729 | 16.382 |

### 5.1.2 Optimization and Evaluation of Second Approach

In this scenario, all the information corresponding to the uncertainties is used to optimize the landing. Such optimization shows poor performance if performed with a single engine, but it improves as the number of engines in the array increases. This not only decreases the landing velocity, but also decreases the standard deviation in the evaluation. The evaluation of the optimization result shows that the best configuration is given for a number of engines equal to $N_e = 10$ and a Regressive PGCS. The altitude and velocity variables of the best result are shown in Figure 5.4, while the distribution of the landing parameters is shown in Figure 5.5. The optimization obtained is grouped in Table 5.5 for the arrangement of engines, where for $N_e = 10$ shown a landing velocity of $-2.97$ m/s and standard deviation of 0.993 m/s. Additionally, the control parameters are in Table 5.6.

Table 5.5: Design parameters of the best result obtained from the optimization scenario with uncertainties.

| **Parameters** | **Value** |
|---|---|
| PGCS | Regressive |
| $N_e$ | 10 |
| $\dot{m}$ | $10.16 \times 10^{-3}$ kg/s |
| $t_a$ | 20.0 s |
| $v_{land}$ | $-2.97$ m/s |
| Std Dev. of $v_{land}$ | 0.99 m/s |
| Mass used | 1.35 kg |

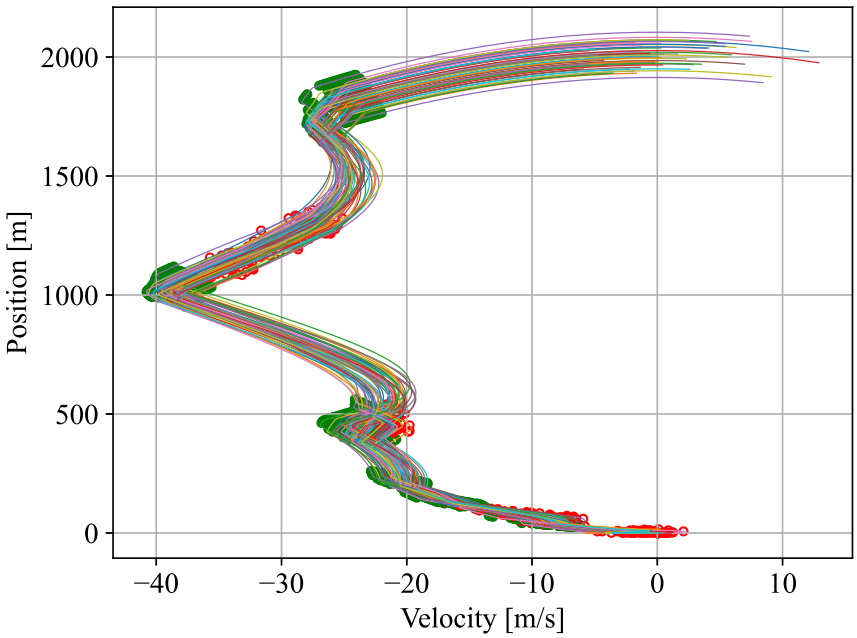


Figure 5.4: Behavior of altitude and velocity in the evaluation of the best $\mathcal{G}$ obtained from the optimization with uncertainties and $N_e = 10$. Color map is used to differentiate different random trajectories.

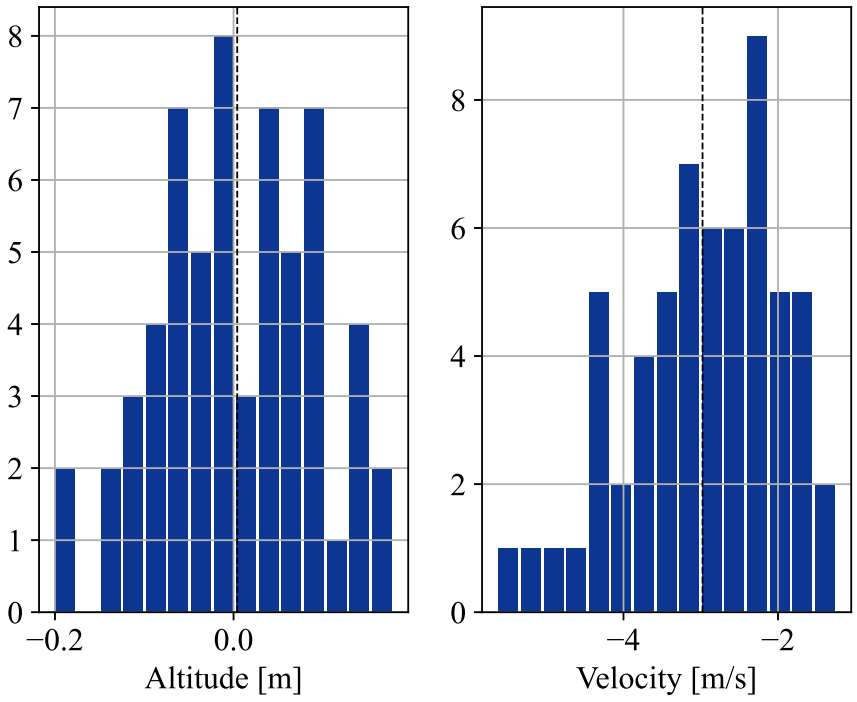


Figure 5.5: Distribution of altitude and velocity landing in the evaluation of the best result obtained from the optimization with uncertainties and $N_e = 10$. The vertical axis shows the frequency of the values.

Table 5.6: Control parameters from the best result obtained in the scenario with optimization uncertainties.

| $k$ | $\alpha_k$ | $\gamma_k$ |
|---|---|---|
| 1 | 0.639 | 12.111 |
| 2 | 0.138 | 11.165 |
| 3 | 0.862 | 4.742 |
| 4 | 0.551 | 12.844 |
| 5 | 0.999 | 11.465 |
| 6 | 0.091 | 6.036 |
| 7 | 0.768 | 22.285 |
| 8 | 0.608 | 5.219 |
| 9 | 0.624 | 17.851 |
| 10 | 0.867 | 24.439 |

As supported by Figure 5.6, we see that the pattern of the performance curves shows asymptotic behavior. This pattern indicates a relationship between the increase in the number of engines and the increase in landing performance. Therefore, $N_e = 10$ is a local optimum based on the limits summed up in this work.

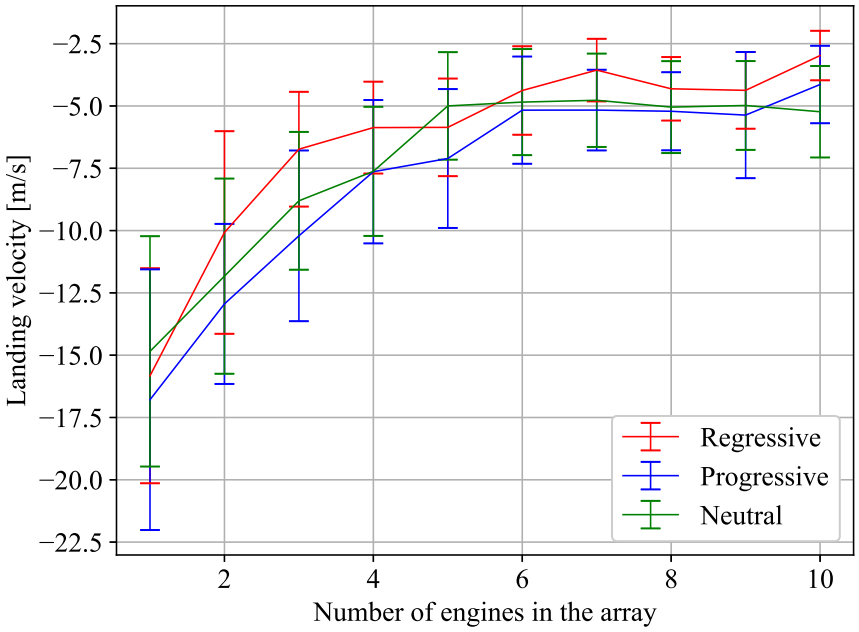


Figure 5.6: Second approach: Performance comparison for an array between 1 and 10 configuration engines, and for the three types of PGCS: Regressive, Neutral and Progressive.

### 5.1.3 Discussion

The optimization carried out with the first approach of Figure 4.8 generated worse scenarios in the evaluation with landing velocity over the 5.87 m/s. Even so, the regressive PGCS simulation in Figure 5.3 shows better performance than the other types of PGCS. In

this scenario, it is possible to see that the ignition points of the $k$-engines of the simulations (the group of green circles in Figure 5.1) do not belong exactly to the control function line. This phenomenon is caused by the dead time $t_d$ and it is observed when $t_d > 0$. In this way, while there is uncertainty about the dead time, all engines start their ignitions below the control function. By not considering this in the classic design of the controller, we can see that the impact velocity distribution of the evaluation has values greater than 10 m/s (see Figure 5.2). Using the approach presented in Figure 4.8, it is not possible to see a clear pattern in the performance of the landing system based on an arrangement of SPEs.

With the second approach summarized in Figure 4.9, we can see an improvement in the performance of the propulsion system. Figure 5.6 shows a performance curve that improves asymptotically with increasing the number of engines. This not only decreases the impact velocity to $-2.97$, $-4.13$, $-4.77$ m/s for Regressive, Progressive, and Neutral, respectively, but also decreases the standard deviation to 0.99, 1.55, 1.87 m/s. This is reflected in the impact velocity distribution for the 60 cases evaluated in simulation, which are shown in Figure 5.5. Additionally, to demonstrate the asymptotic behavior of the performance, an auxiliary simulation is performed with $N_e = 16$. Figure 5.7 shows the behavior of the altitude and velocity, meanwhile Figure 5.8 shows the distribution. From this distribution, it can be seen that the mean landing speed is $-2.04$ m/s and the standard deviation is 0.48 m/s. Although these values are above the landing speed of $-1.7$ m/s of the Chang'E 5 module [23], they are well below what was the landing of the MPF with $-12.5$ m/s, and the CubeSat OMOTENASHI with $-30$ m/s. Finally, the total mass used by the propellant in the soft-landing stage is 1.35 kg , which corresponds to 5.62% of the 12U CubeSat mass.

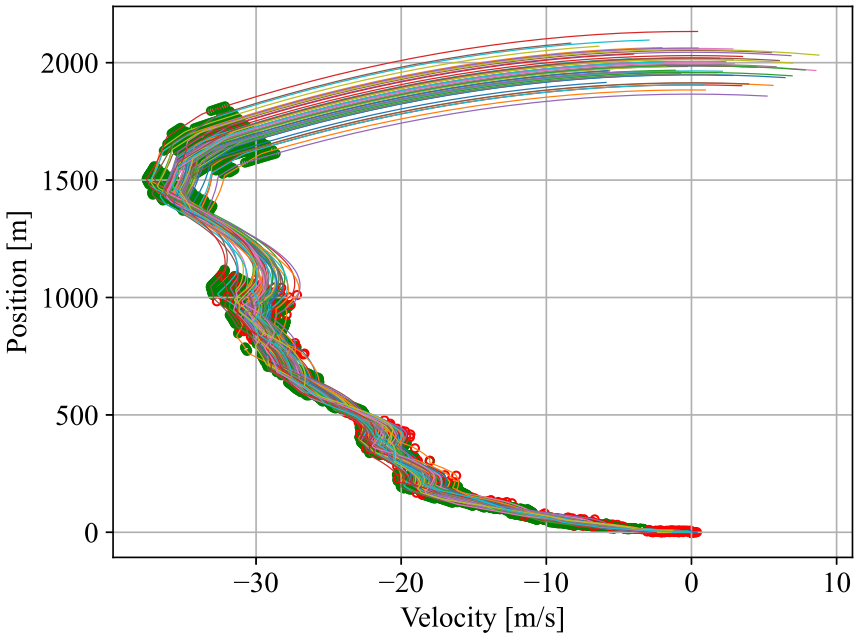


Figure 5.7: Behavior of altitude and velocity in the evaluation of the best $\mathcal{G}$ obtained from the optimization with uncertainties and $N_e = 16$. Color map is used to differentiate different random trajectories.

With respect to the dead time, the evaluation of the second approach shows that the

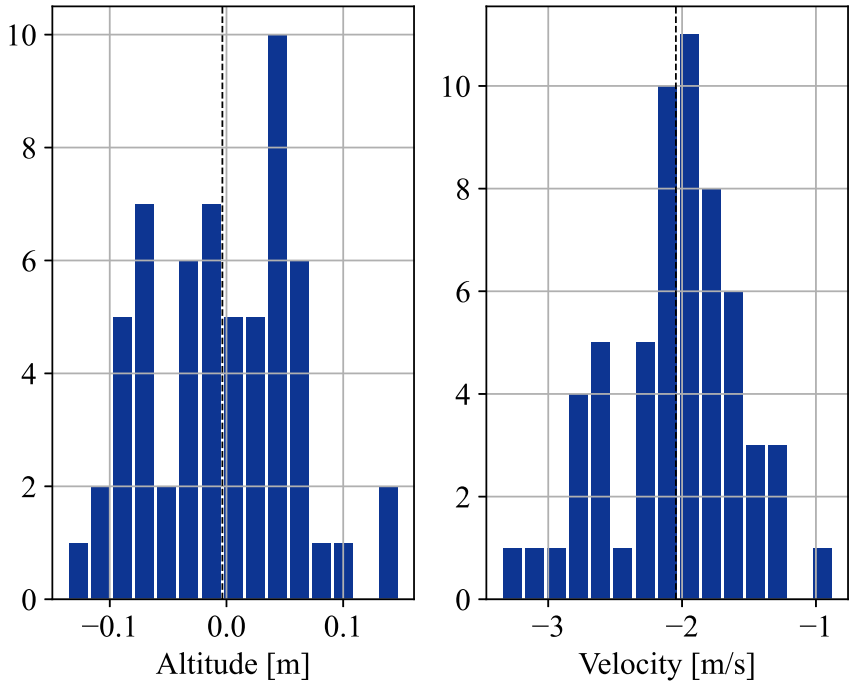


Figure 5.8: Distribution of altitude and velocity landing in the evaluation of the best result obtained from the optimization with uncertainties and $N_e = 16$. The vertical axis shows the frequency of the values.

control design is robust to the ignition dead times. This improvement is more evident in a regressive PGCS, which can be designed as a star type, or with a tubular grain of variable cross-sectional area. Lastly, a star-type burn configuration can work with a thinner-walled engine to withstand the temperatures and pressures of the combustion chamber. This helps to decrease the weight of the engines, as mentioned in Table 3.2. However, this configuration has a small action time $t_a$ compared to the results in the Tables 5.3 and 5.5.

## 5.2 Planar Coordinate Simulation

As mentioned above, control optimization and design will be carried out in separate parts. The first stage is the release of the module into orbit, the second is vertical braking, and the third is soft landing. For orbital release it is necessary to find the best cost function that helps us minimize the mass used, that is, look for a representation of what is shown in Figure 4.13a. Braking requires a push in a radial direction with a large amount of force, and a large amount of mass used. The last stage requires finer thrust elements, compared to the previous ones, and with a greater degree of orientation control.

### 5.2.1 Entry

According to the requirements of this point, a cost function can be defined that minimizes the energy $e_M$ of the module. However, as will be seen later, this mainly affects the height at which the module orbits, since the height dimension is orders of magnitude greater than the speed. That said, a cost function must be defined that penalizes the speed of the module more, as shown below.

$$J = e_M + \eta v_{aux}^2, \tag{5.4}$$

where $\eta$ es a gain, en $v_{aux}$ is an auxiliary velocity. For the example case below, and the input stage of the module, $v_{aux}$ is defined as the tangential velocity $v_T$ in orbit. This speed needs to be decreased to avoid horizontal speeds upon landing. Within the optimization, the tangential velocity is calculated as,

$$v_{aux} = v_T = \cos(\psi - \pi/2)v_x - \sin(\psi - \pi/2)v_y, \tag{5.5}$$

where $\psi$ is the positional angle with respect to cartesian plane, $v_x$ and $v_y$ are the $x$ and $Y$ components of cartesian velocity, respectively. $\psi$ is calculated with cartesian position as

$$\psi = \arctan(R_y/R_x). \tag{5.6}$$

Below are simulations optimized for values of $\eta = (0, 1, 100, 10000)$ and with $J = v_t^2$. In Figure 5.9 you can see how this affects the energy and tangential speed of the module for different types of PGCS. The optimization of this example is done with PSO. As can be seen, there is no appreciable difference with the type of PGCS, but a difference can be observed by changing the cost function. On the other hand, Figure 5.10 shows the tangential speed of different modules (represented by the blue lines) for different conditions of the cost function. Therefore, if it is required to immediately decrease the tangential velocity (analogous to horizontal velocity) upon landing, a cost function $J = v_T$ is needed.

Note: the different trajectories of the modules in Figures 5.9 and 5.10 were created from the same initial condition, but considering the measurement uncertainties mentioned in section 4.4.2.

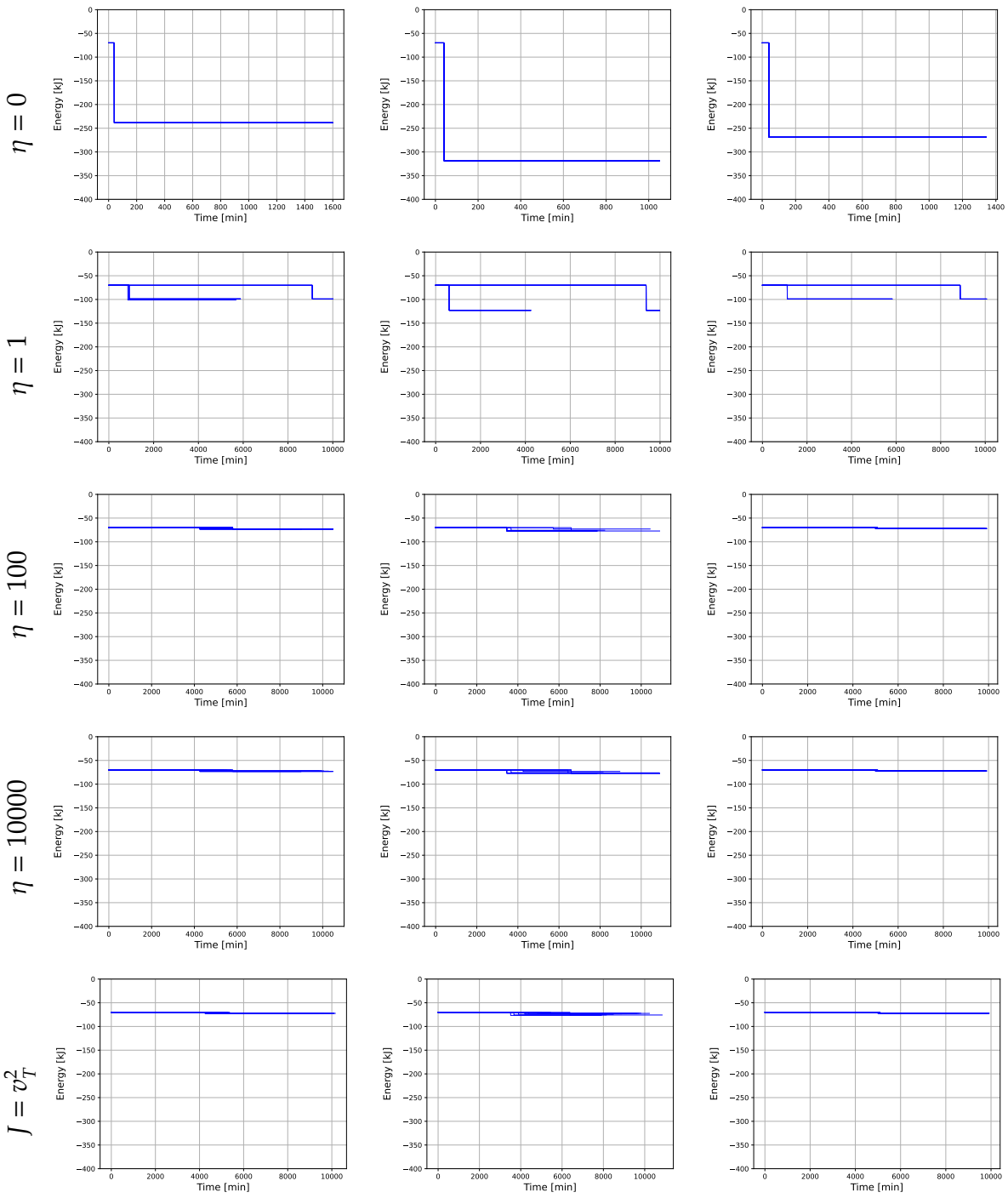


(a) Progressive (b) Neutral (c) Regressive

Figure 5.9: Evolution of the total energy of different modules represented by each blue line. They are shown for different types of PGCS, and for different values of $\eta$.

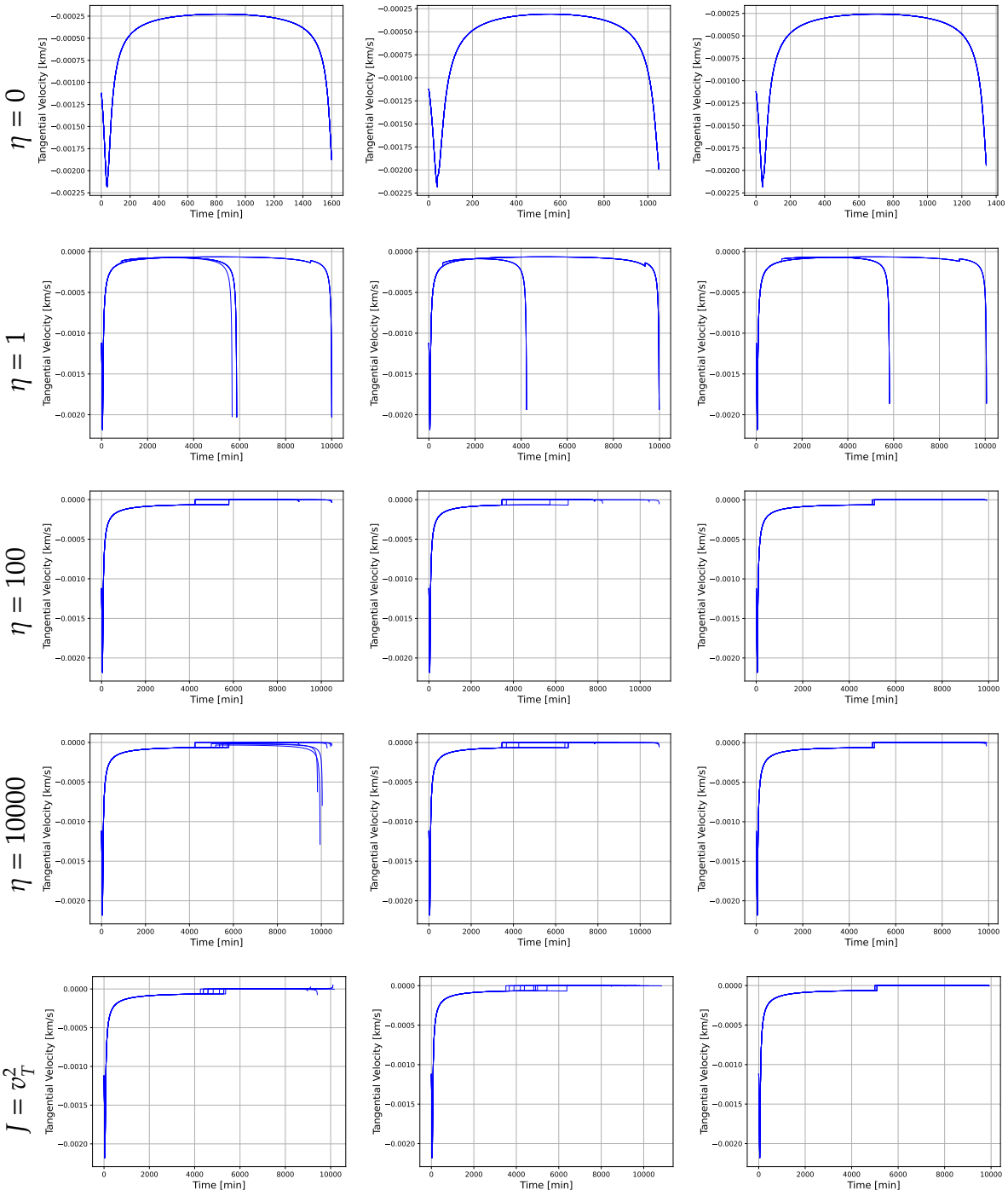


(a) Progressive (b) Neutral (c) Regressive

Figure 5.10: Tangential velocity for different modules and conditions of the cost function. The result is shown for the three types of PGCS mentioned in this work.

From the results presented, the cost function is selected where only the tangential speed is considered. On the other hand, it is important to look for the minimum thrust that manages to satisfy the cost function while minimizing the mass used. For this, the cost function is modified as

$$J = \left( \frac{v_T^2}{m(t_f)} \right), \tag{5.7}$$

where $m(t_f)$ is the final mass.

The next step of the exploration, using a PSO algorithm, focuses on finding the external diameter and length of each SPE. Due to design concepts, it is defined that the input stage is carried out by two neutral-type SPEs. The main reason is for its stability and for decreasing the thrust level in exchange for increasing the burning time. This feature decreases residual torque compared to other types of PGCS. Figure 5.11 shows the convergences of the particles of the algorithm for ten different trajectories, where **P1** is the ignition point (angle) with range in $[0, 2\pi]$ *ra*d, **P2** is the external diameter of the propellant with range in $[0.03, 0.05]$ $m$, and **P3** is the length with range in $[0.15, 0.2]$ $m$. As can be seen, the ignition points are close to the apolune as expected from Figure 4.13b when the mass decreases. As these simulations include the uncertainties of the parameters, the ignition points are not unique, but they continue to remain within the same zone. On the other hand, the dimensions of the engine do not have a clear point of convergence, and in reality they seek to compensate the diameter for the height until the required thrust is achieved. However, the average diameter is above 0.04 m, and the height is below 0.18 m.

In Figure 4.5.1 it is mentioned that in this stage two SPEs from the ends are considered. Now, from the results obtained, it is known that they must be of the neutral type. This implies that the residual torques will be able to decrease their torque level thanks to the low thrust of a neutral SPE. Along these same lines and considering the results of the previous simulation, it is defined that the diameter of the motors will be 0.04 m and 0.2 m long. The main reason is that by decreasing the diameter, the thrust and residual torques also decrease. And to compensate for the loss of momentum, the length of the engine is increased.

From the above, the results for a fixed diameter of 0.04 m and length of 0.2 m are shown in Figures 5.15 and 5.16. The optimization result is shown in annex 7.1.5.

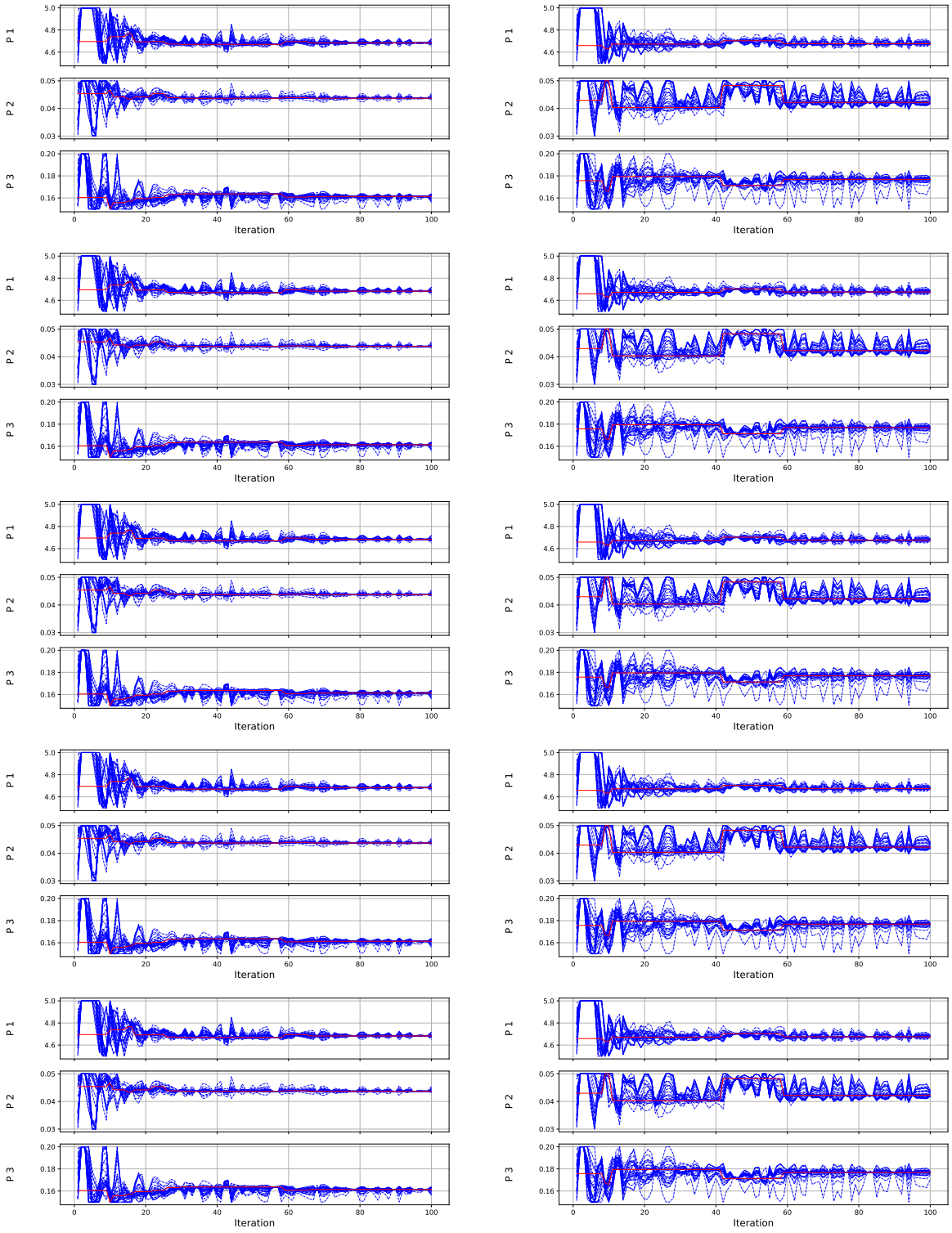


Figure 5.11: Solution of the optimization problem of the equation (5.7). The blue lines show the positions of each particle in the algorithm and the red line is the global best solution.

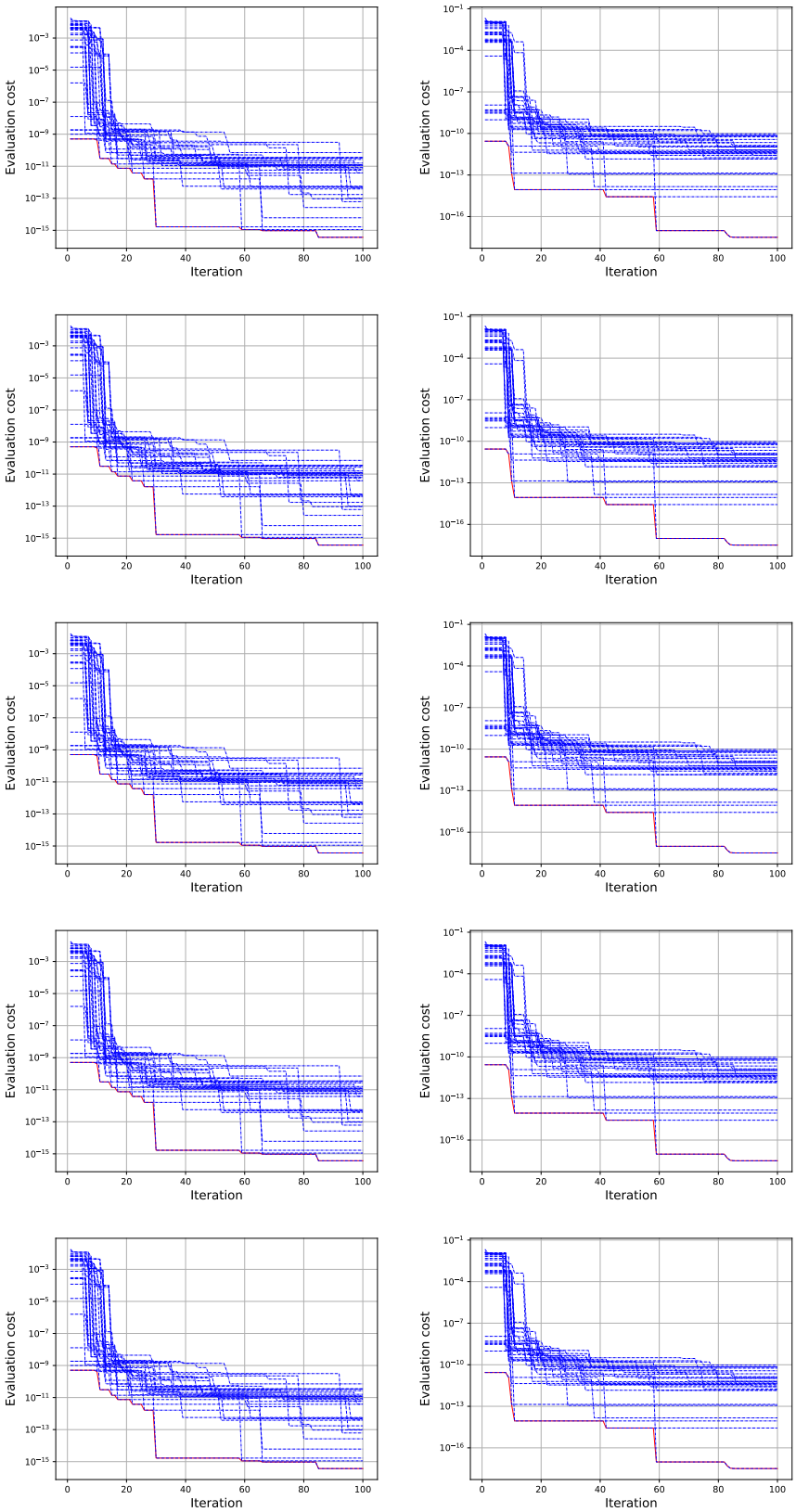


Figure 5.12: Evaluation of the cost function of the optimization problem of the equation (5.7). The blue lines show the individual evaluation of each particle and the red linear is the best cost evaluation.

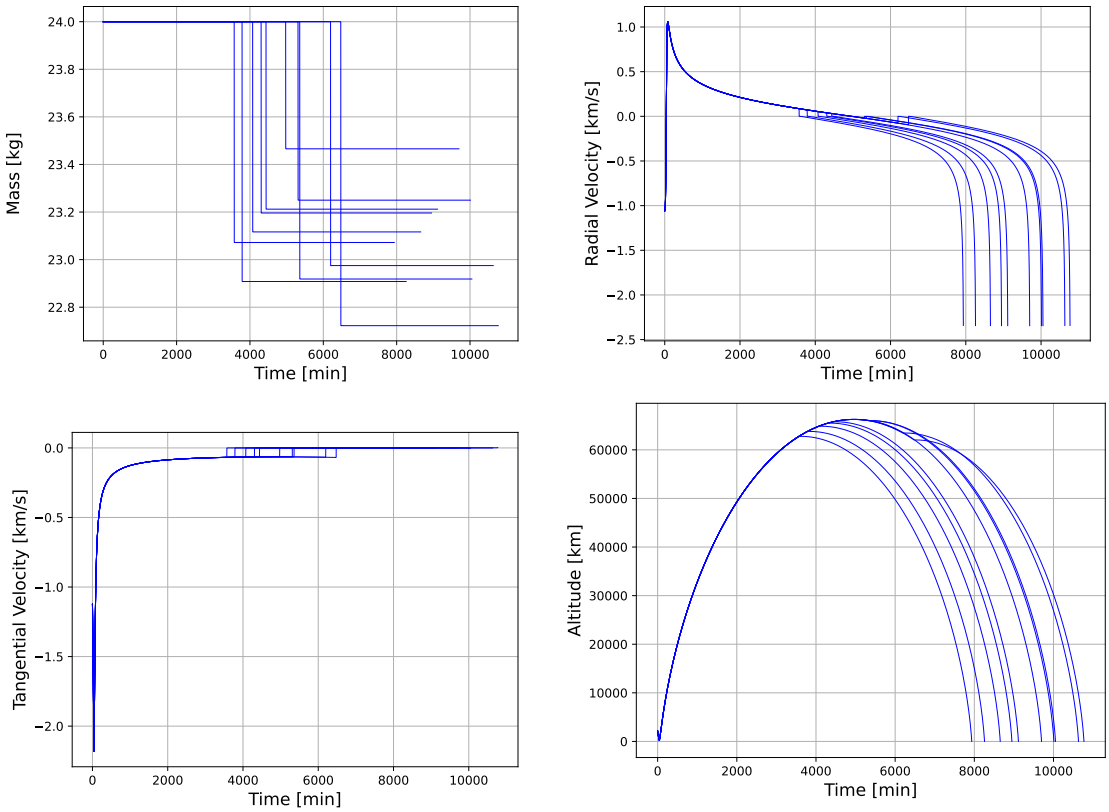


Figure 5.13: State solution for 10 trajectories.

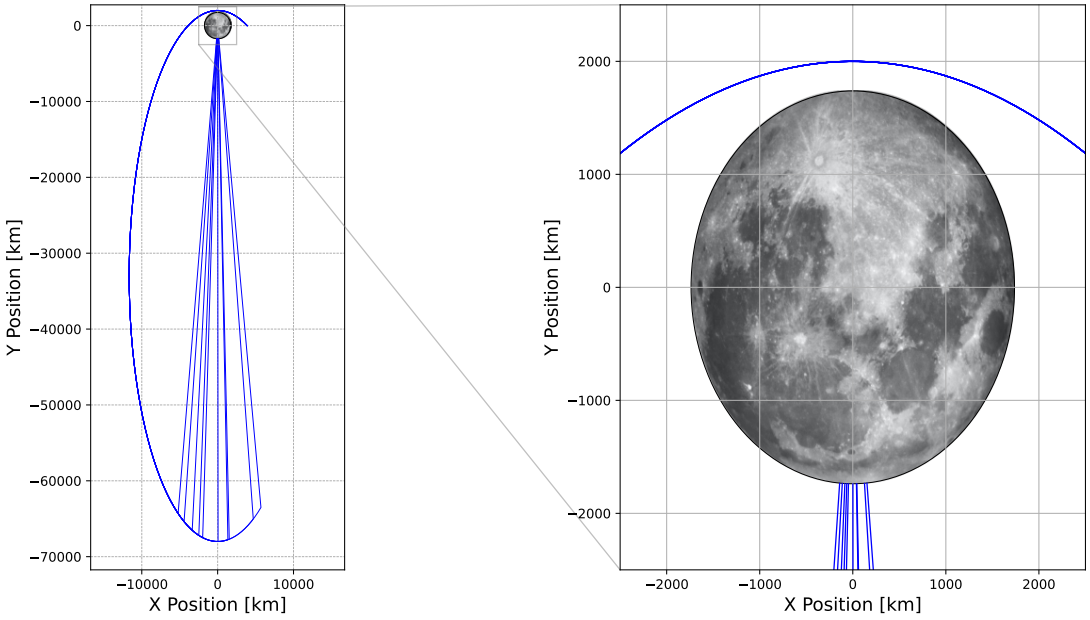


Figure 5.14: Orbit solution for 10 trajectories.

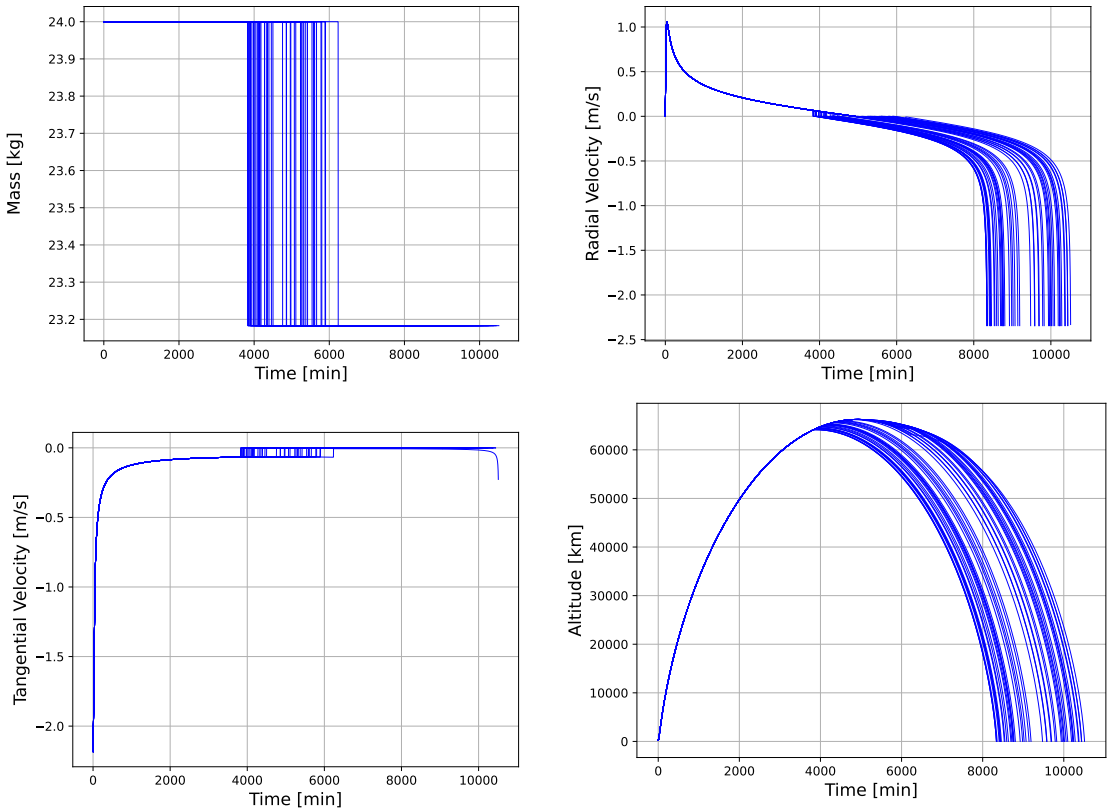


Figure 5.15: State solution for 50 trajectories optimized with a fixed dimension of SPE.

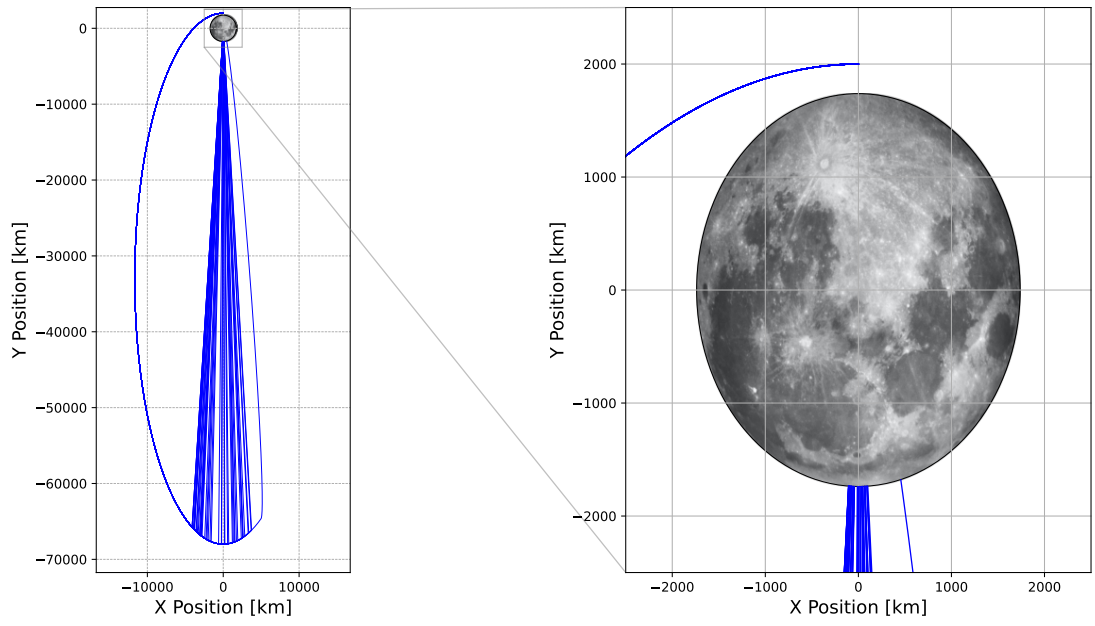


Figure 5.16: Orbit solution for 50 trajectories optimized with a fixed dimension of SPE.

The question that arises now is what is the effect in terms of torque and why the Neutral type burn is more convenient. From Figures 5.9 and 5.10 it is observed that in

terms of the trajectory, there are no important differences between the different types of PGCS. However, from the equation (4.47) it is known that if the burning area is very large, the pressure will also be large, which will make the motor casing more massive. Large burn areas are typical of progressive and regressive PCGS, at least at one point in time. Therefore, Neutral burning is essential at this stage. In the subsection 5.2.1 are all possible residual torque scenarios with the dimensions obtained in the results above.

**Attitude Requirements at Entry**

As mentioned above, this stage considers using 2 black motors simultaneously (these are shown in Figure 4.21). As the SPEs are not in the center of mass, they generate different torques according to the uncertainty variables mentioned in Table 4.4. To observe which element generates higher residual torques, a separate sensitivity analysis is presented for each uncertainty and for the arrangement of the two black motors. Figures 5.17 and 5.18 show 1000 Monte Carlos simulations around the uncertainties of the residual torques. The SPEs are considered to be aligned with the axis $\hat{z}^b$.

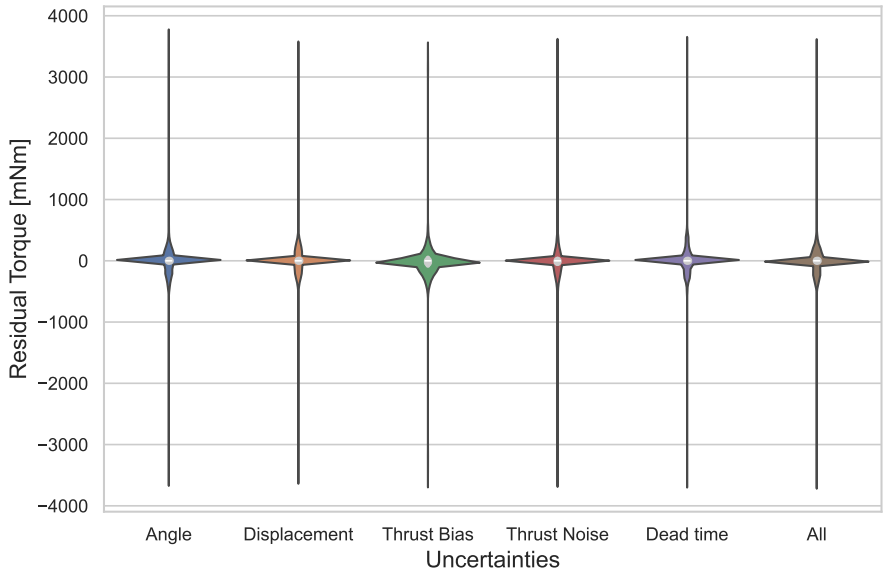


Figure 5.17: Violin plots for the residual torque distributions of each variable mentioned in Table 4.4. High torques of 4 Nm can be seen but the largest amount is concentrated around zero.

Figure 5.18 shows a close-up view of the distribution generated by each normalized variable. Although all variables generate torques close to 4 Nm, the population distribution is slightly different. For the uncertainties in the angle, the distribution has a lower standard deviation than the rest of the group, and all the uncertainties together generate the highest standard deviation of the group.

In the entry (or reentry) stage, the module must point in the opposite direction than the unit velocity vector, that is, the target vector must be equal to $-\hat{v}$. Then the angular error

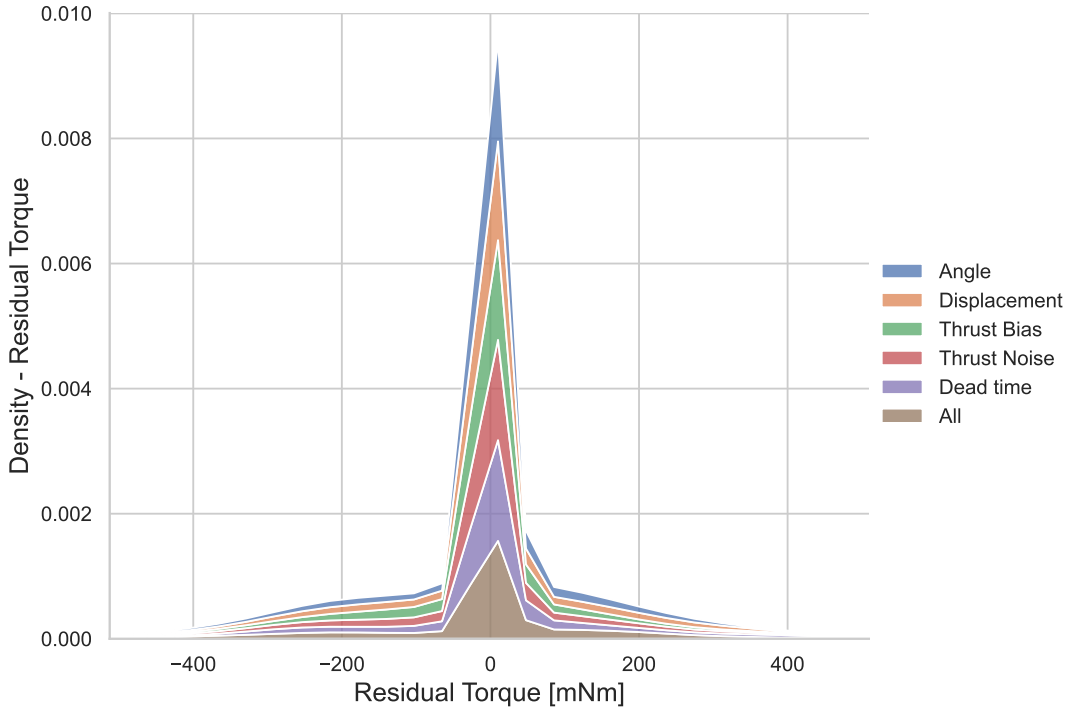


Figure 5.18: Normalized graph of the distribution of residual torques with an approach to the most populated areas.

with respect to $\hat{z}^b$ axis in body frame is defined as

$$\theta_{error} = \arccos(< \hat{z}^b, -\hat{v}^b >) = \arccos(< \hat{z}^{\mathrm{i}}, -\hat{v}^{\mathrm{i}} >). \tag{5.8}$$

### 5.2.2 Descent

For the descent stage the cost function changes to the radial velocity $v_R$ of the module. Taking as reference the component perpendicular to the equation (5.5), the following cost function is defined,

$$J = 0.1 \cdot (\|\mathbf{R}\| - R_m) + \left(\frac{v_R^2}{m(t_f)}\right), \tag{5.9}$$

where $(\|\mathbf{R}\| - R_m)$ is the altitude of the module. This term is added to force the optimization to explore low altitude areas, otherwise it remains at high altitudes where the radial velocity is low without turning on the SPE.

On the other hand, the simulations are separated so that the cost function is more focused on the ignition point of interest. That is, first the entry point is optimized, and then the best trajectory is taken as the starting point of the new trajectory search. As an example, Figure 5.19 shows the PSO optimization results for the input case. Then, the continuation of the best trajectory is shown in Figure 5.21.

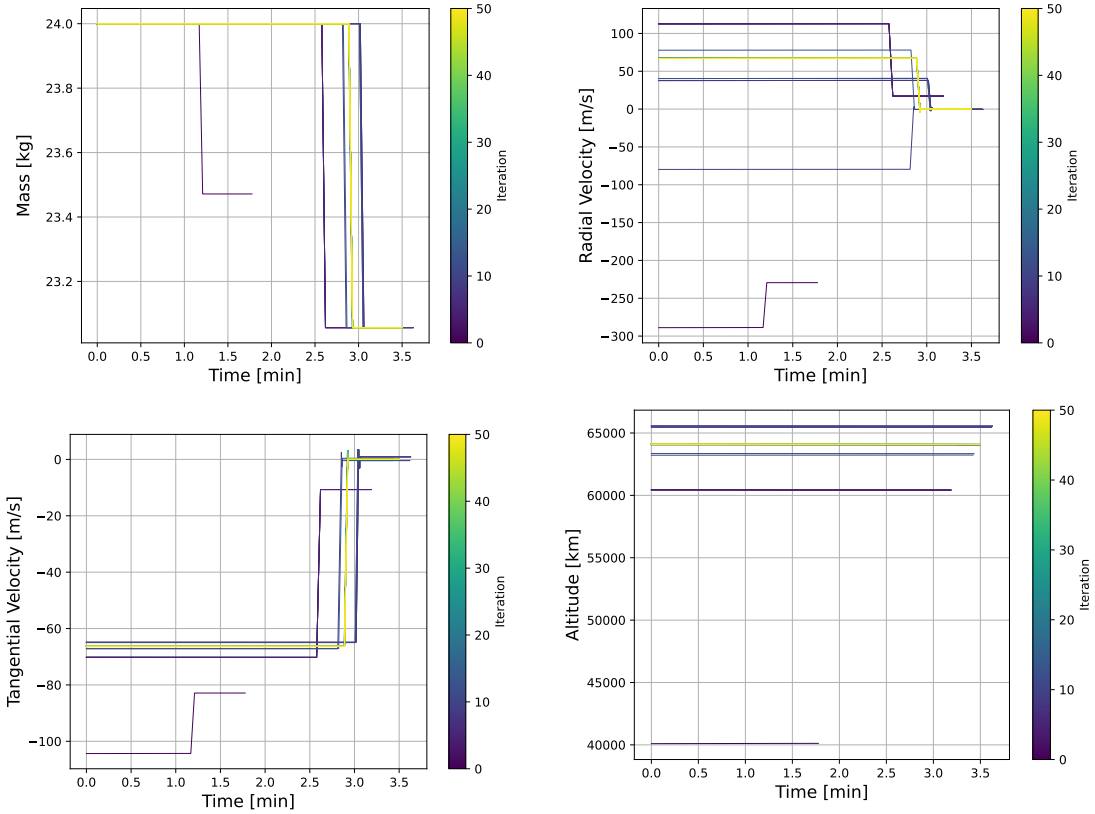


Figure 5.19: Evolution of the best candidate for PSO optimization. The bar shows the iteration it belongs to. This result seeks to minimize the tangential velocity.

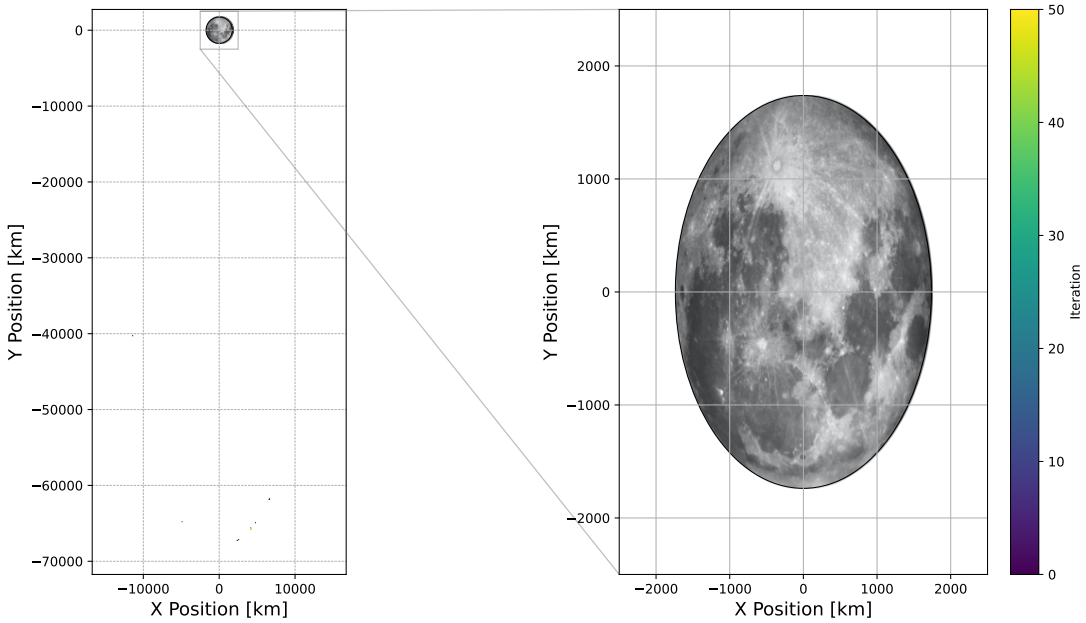


Figure 5.20: PSO orbital solution. The initial simulation point begins 0.01 degrees before the ignition point to include the effects of numerical integration on the ignition position.

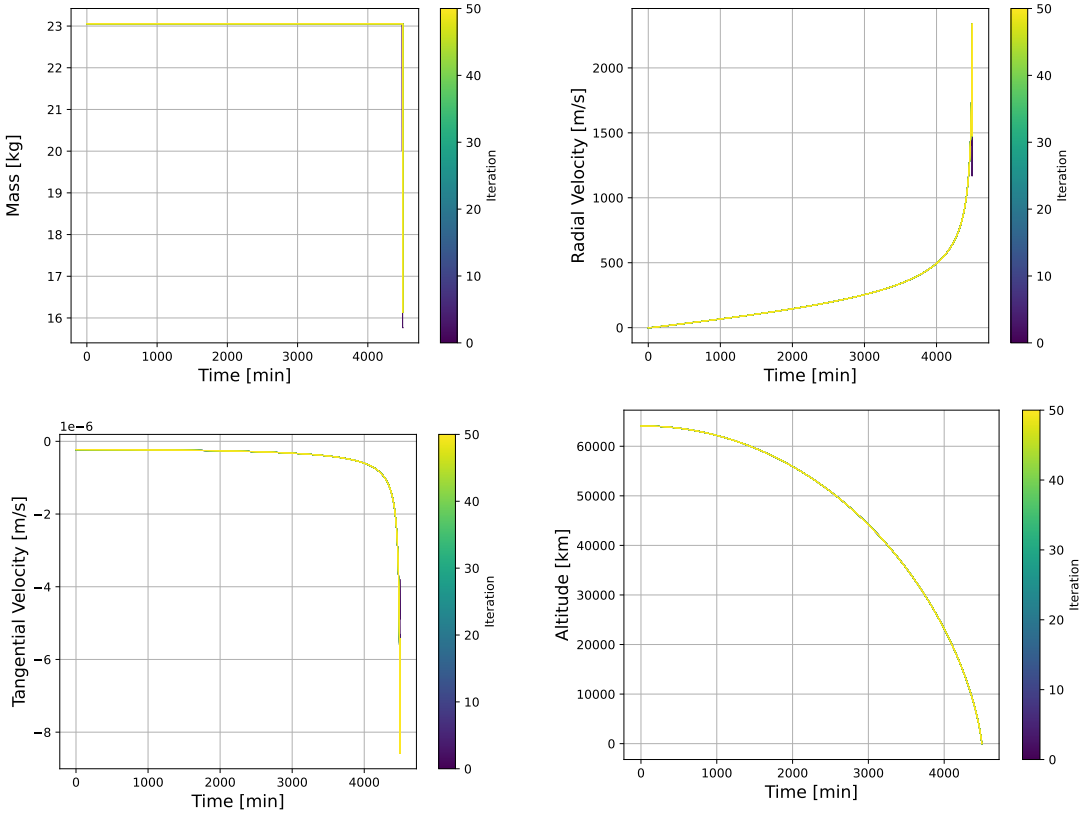


Figure 5.21: Evolution of the best candidate for PSO optimization. The bar shows the iteration it belongs to. This result seeks to minimize the radial velocity with the mechanical constraint of the section 4.5.1 and using the final state condition of the Figure 5.19.

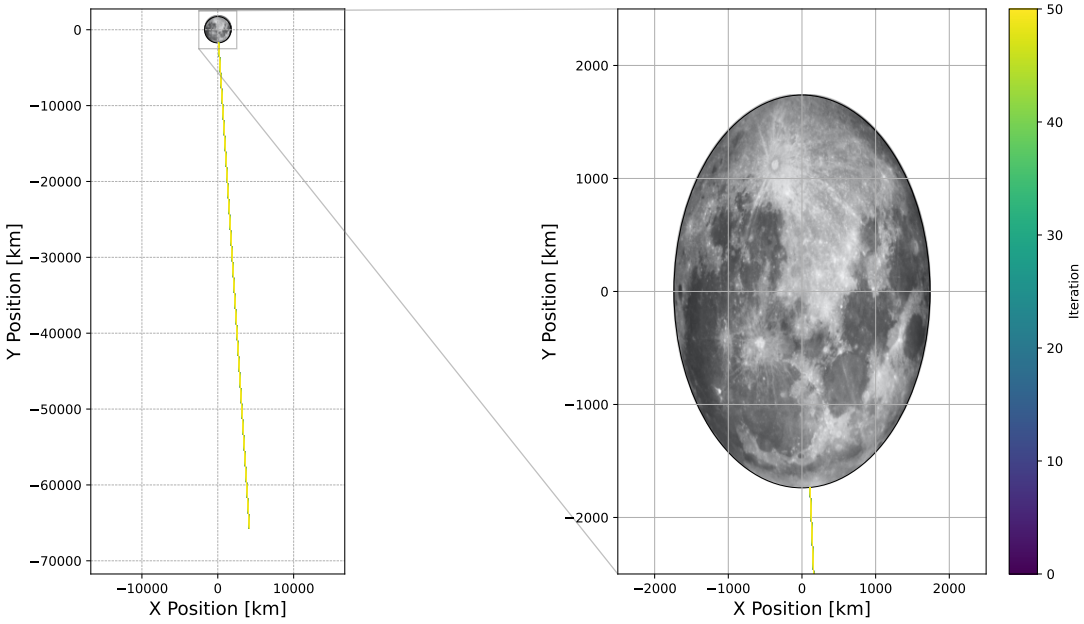


Figure 5.22: PSO orbital solution for radial velocity optimization.

Zooming in on the results in Figure 5.21, it can be seen that the module has not yet reached the surface (2000 m) and that the descent velocity is 1480 m/s. This can be seen in Figure 5.23. Finally, the entry and descent process is shown in the following Figures.

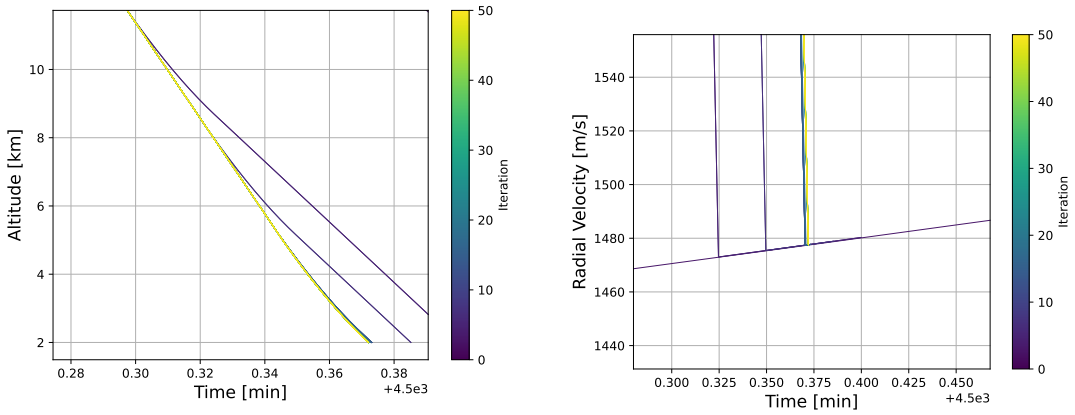


Figure 5.23: Altitude and radial velocity for descent stage optimization.

Taking the results from Figures 5.16, 5.20, and 5.24, the optimizations (derived independently) are grouped in Figure 5.24 and 5.25. The optimal ignition point, defined by the color yellow, shows the entry and descent trajectory to reduce the tangential and radial velocities, respectively.

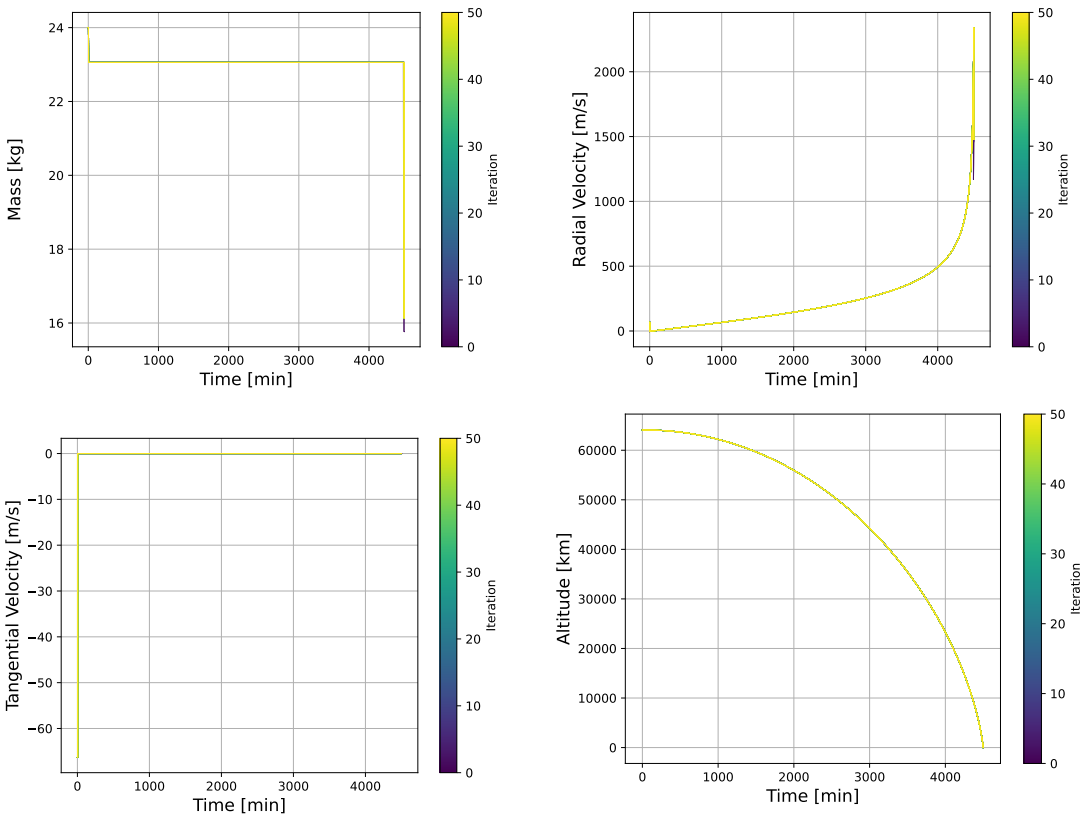


Figure 5.24: PSO optimization for Entry and Descent stages.

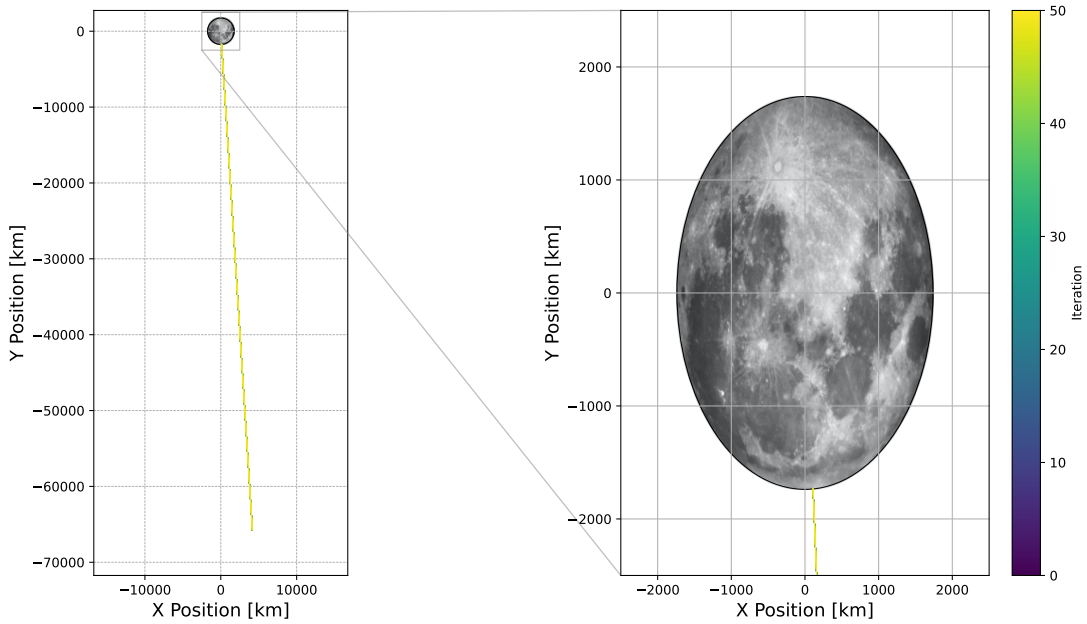


Figure 5.25: PSO orbital solution for entry and descent optimization.

The optimization process is shown in the appendix 7.1.5.

# 6. Conclusions

In this work, a methodology to solve the soft-landing problem with an array of solid propellant engines (SPEs) was presented for the last stage of EDL. This study was performed by using a 1-dimensional dynamic model and for different numbers of engines in the array, where each one is controlled independently by a linear control function $\beta_k(t)$. This linear function is designed with two gains, $\alpha_k$ and $\gamma_k$ for each engine, which are optimized by GA using two different approaches following the current stage of art. Consequently, the optimization based on the second approach, robust design, presents better results in the evaluation simulations that considered the uncertainties of the variables. The results show that the SPEs array generates an asymptotic increase in performance as the number of engines increases, which also helped to decrease the standard deviation of the impact velocity distribution. For a range of $N_e \in [0, 10]$, the lowest impact velocity is $-2.97\ m/s$ with a standard deviation of $0.993\ m/s$ for $N_e = 10$. These findings show that the regressive propellant grain cross-sections (PGCS) allow landings with lower impact velocities than those obtained with progressive and neutral PGCS. On the other hand, this approach is independent of the thrust profile modeled in this work and can be replaced by measured thrust data.

It was extended in the analysis to an orbit in the Cartesian plane, considering the residual torques that are generated during ignition. Considering the increase in variables and calculation times of the GA optimizer, it was changed to a continuous optimizer such as the PSO, which showed greater agility for eccentric orbits. This included creating a Simulation Framework that changed the RungeKutta integration steps from fixed-fine to variable, depending on whether the module was near an ignition point. For this scenario, it was found that considering the uncertainties there is an approximate arc of 10° where the first ignition point can be generated without increasing the tangential speed (Figure 5.16). On the other hand, the simulations show that the residual torque is lower for an END-Burning type thrust, in line with the results of [4]. But even with this type of thrust (small, but long lasting compared to the other burns), residual torques greater than 400 mNm are generated as seen in Figure 5.18. This value is comparable with commercial reaction wheels, however, it must be taken into account the torque peaks that reach 4mN as shown in the Figure 5.17.

Finally, a simulator framework was implemented to continue researching and developing tests of algorithms involving SPEs. The simulator allows you to optimize certain engine geometry in the ranges defined by the user. On the other hand, the simulator has the potential to be applied for other types of missions, such as small spacecraft orbital

maneuvers, where the ignition point can also be optimized by changing the cost function.

The algorithms used to model, simulate, and optimize the control scenarios in 1D were uploaded to a GitHub repository with a free license (`https://github.com/spel-uchile/SolidPropellantforLanding`).

The algoritm used to solve the proposed work in 2D was uploaded to a GitHub repository (`https://github.com/EliasObreque/SP_Landing/tree/Thesis`)

# 7. Future work

Future work seeks to reduce the residual torque generated by the engines, either by improving the ignition electronics or creating a hybrid drive. However, the latter would be to control the attitude.

## 7.1 Hybrid propulsion

This is a current work that is about to be published. We are working on testing very low-cost and robust commercial automobile injectors.

### 7.1.1 Automotive fuel injector

This section presents a brief description of automobile injectors based on M. B. Çelik et al. [90]. One of the main features of the new electronically controlled automotive injectors is that they are ideal for controlling the flow rate necessary to improve combustion efficiency. The current injectors were designed to have low noise and low specific fuel consumption. An example of the injector is shown in Figure 7.1, where the electrical/hydraulic connector, coil, armature, and sealing are presented.

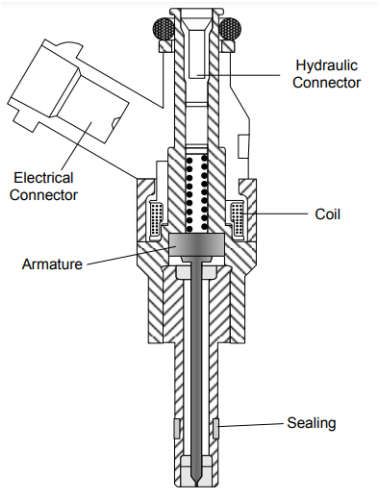


Figure 7.1: Typical High-pressure injector. Source [90].

The electrical connector is used to control the state of the coil that opens and closes the fuel outlet. When the coil is energized, the armature allows mass flow, and then a spring

returns it to its initial closed state.

Summarizing, the propulsion systems are widely used in CubeSat-type satellite missions, opening a door for the development of accessible and low-cost micro-propulsion systems. In this line, automotive fuel injectors can play an important role thanks to their reliability, durability, effectiveness in long-term use, and ability to work under high-pressure conditions. On the other hand, they are low-cost commercial systems that are accessible at any car mechanic store. In the development of this article, we show our preliminary evaluation of an injector used as a valve and tested at ambient pressure and vacuum. The methodology used for the tests, the calculation of metrics, the analysis of the results, and the conclusions are also presented.

### 7.1.2 Methodology

The methodology section contains the hypotheses of our work, the approach of the experiments, and the acquisition of data. For final operating conditions, it is expected that the injector can be adapted to work with liquid or gaseous sources. Therefore, in the first test, we introduced the injector operation at ambient pressure with liquid alcohol, and then we switched to pressurized air in the vacuum tests. The change from liquid to gas is mainly done to prevent damage in the vacuum chamber, but also to show that the injector can work for both liquid and gas source.

**Hypothesis** The following hypotheses start the investigation of this article.

1. By pressurizing liquid alcohol to over 1 atm and using the injector as a valve, measurable micro-thrusts, and mass flow can be created in atmospheric conditions to quantify the performance of the injector.

2. A latex balloon can be used to pressurize the liquid alcohol with minimal pressure difference. This pressure is the elastic pressure of the latex.

3. Automotive fuel injector has a heritage in environments with high differential pressure and then could work in a vacuum environment.

4. In the vacuum test, the pressurized balloon and its joint with the injector must be isolated. It is proposed to add an airtight acrylic chamber on the outside of the latex balloon in order to seal the pressurized balloon under vacuum conditions and to observe the behavior of the latex balloon in the event of possible leaks.

### 7.1.3 Experimentation

**Components** The electrical components used to measure the thrust are shown in Table 7.1, and Figure 7.2 to 7.4. The load cell is used to measure the mass variation produced by the propellant, which is then amplified by the HX711 component. Additionally, for proper function of the injector, a stable circuit is required during propulsion tests. Figure 7.4 shows the control board to carry out the injector activation tests. The power supply is made with 12 [$V$] with an average consumption of 0.25 [$A$] (3 [$W$]).

The main circuit is made up of several elements, with the ne555 oscillator in Zone I being the most prominent. This oscillator is capable of controlling the output frequency as a function of a variable resistor in Zone II and a fixed capacitor. The frequency range that it can generate is between approximately 2 and 159 [$Hz$]. The circuit has a power stage in Zone V that allows controlling the current consumed by the injector (A critical element in CubeSat satellites). This power stage uses a TIP3055 and is directly connected to the output of the injector located in Zone IV of the image. Together, these components allow a controlled and efficient injector activation tests.

Table 7.1: Electronic components.

| Name | Work |
|---|---|
| Load cell of max 100 g | Used to measure analogically the thrust of the injector |
| HX711 | Used to amplify the analog signal and convert to digital signal |

Figure 7.2: Load cell of 100 (g) max.

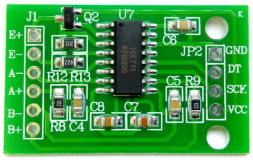


Figure 7.3: Analog digital converter HX711

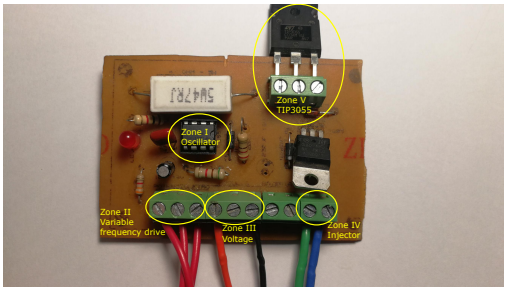


Figure 7.4: Injector control circuit.

To increase the data sampling, a modification was made to the HX711 device, as directed by the vendor. This can be seen in Figure 7.5c, where a pin need to be up as shown in Figure 7.5a, and then, it needs to be soldered to high voltage as shown in Figure 7.5b with modification.

The injector used is identified with the model 1.0 12V BER. 3P/B/998CC from a OPEL Corsa vehicle, and is shown in Figure 7.6. Incorporating the pressurizing latex balloon, the preliminary injection system is shown in Figure 7.7.

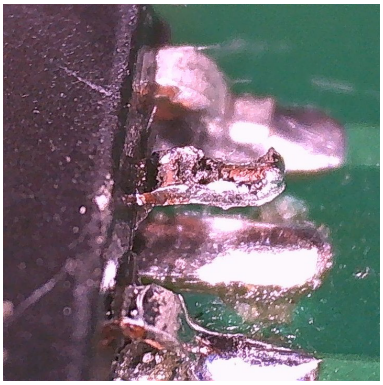

(a) Pin disconnected

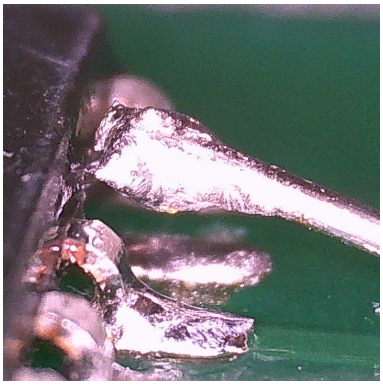

(b) Welded pin

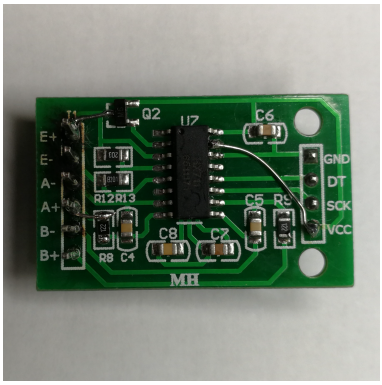


(c) Modified component

Figure 7.5: HX711 Circuit Modification

Figure 7.6: Injector model: 1.0 12V BER. 3P/B/998CC.

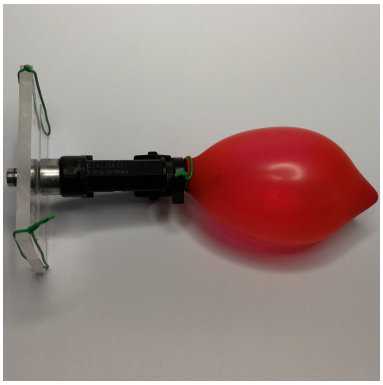

Figure 7.7: Injector with pressurized latex balloon.

**Test bench** A test bench is building with an acrylic platform as a support to measure the thrust in atmospheric conditions, and a PVC cylinder is used to keep the injector in a vertical position to avoiding measurement errors produced by a horizontal measurement (the platform is shown in Figure 7.8). This test bench measures the resistor difference of the load cell, which has a direct relationship with the vertical normal force divided per the gravity acceleration of the system (the static mass). Different known masses were used to calibrate the voltage signal from the resistor with the corresponding mass. On the other hand, the normal force depends on the current system mass and the thrust generated by the injector. The mathematical model is derived from the Free body diagram shown in Figure 7.9, $N$ is the normal force, $W$ is the weight, $T$ is the Thrust, and $y$ is the relative displacement.

The dynamics presented consider only vertical elements, since the horizontal deformation of the load cell is not significant in the dynamics. The system was previously calibrated to associate the voltage difference (resistance variation) as a function of the

graduated static masses. The resistance change is measured with two centrally placed load cell voltage gates, generating potential differences in the circuit. To avoid torsion and angular strain calculations, the calibration relates the voltage measurement to the normal force $N$, i.e. $N = m_m/g$ with $m_m$ as the measured mass and $g$ the acceleration of gravity. The dynamics of the system is

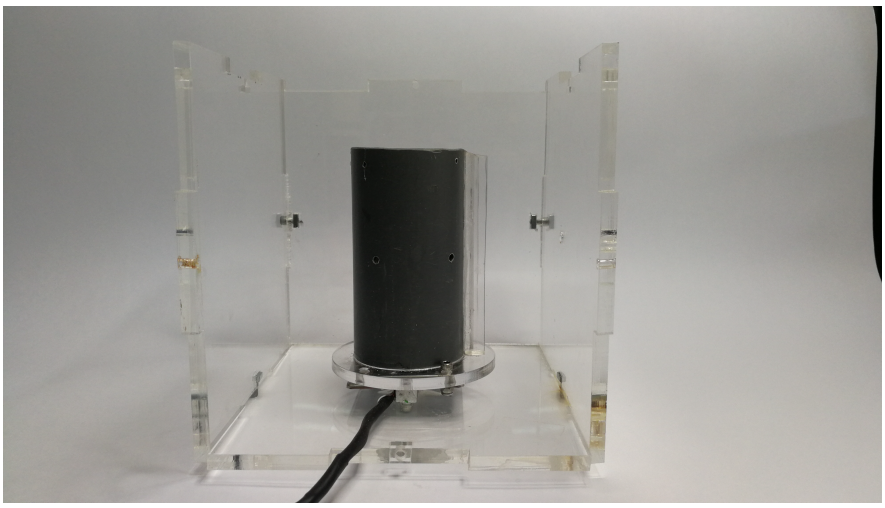

Figure 7.8: Vertical test bench configuration.

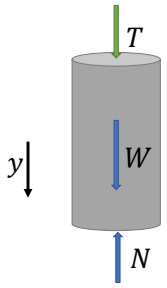


Figure 7.9: Free body diagram of the injector system and the Load Cell.

$$N - W - T = m\ddot{y} + c\dot{y} + ky, \tag{7.1}$$

where $T = \dot{m} I_{sp} g_e$ with $I_{sp}$ as the specific impulse, and $g_e$ the gravity acceleration in sea level. $c$ and $k$ are the damping and equivalent spring rate of the load cell (beam embedded in one end), respectively. Now the expected mass measured $m_m$ is

$$m_m = \frac{m\ddot{y} + c\dot{y} + ky + mg + \dot{m} I_{sp} g_e}{g}. \tag{7.2}$$

Generally, the terms associated with the free response of the load cell, such as the beam embedded in one end, are usually not considered.

**Vacuum test** For this test, we use the knowledge acquired in the PlantSat mission of the space and planetary exploration laboratory (SPEL) of the University of Chile. This mission contemplated the manufacture of a transparent hermetic container to carry a plant into space, allowing the entry of light and the acquisition of images, as seen in Figure 7.10. In this process, containers with different dimensions were created, but they differed mainly by the number of O'rings used. Experimentally, the configuration with two O'rings was found to have no significant leakage within 3 months, and once the vibration tests had passed, it was selected to go on the satellite that is currently located in orbit. This leaves us with two interesting versions of test chambers: the fly version with two O'ring and without leaks, and a version with only one O'ring and significant leaky.

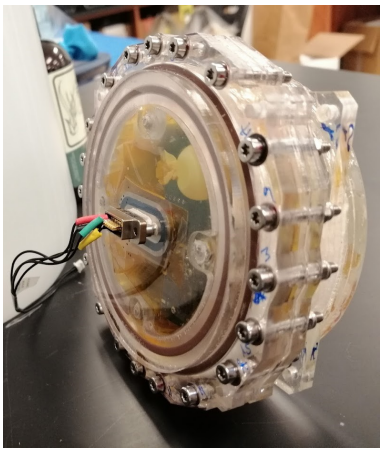

Figure 7.10: Container Payload in PlantSat mission. Knowledge of design and manufacturing is used in this work.

In conclusion, the version with leaks is used in this work to observe the robustness of the system in the face of a possible drainage in space. In addition, the behavior of the latex balloon in that condition can be observed. On the other hand, this vacuum test helps to observe the behavior of the injector in a vacuum environment and quantify the pressure released in each control pulse. The setup for the experiment is shown in Figure 7.11 and 7.12.

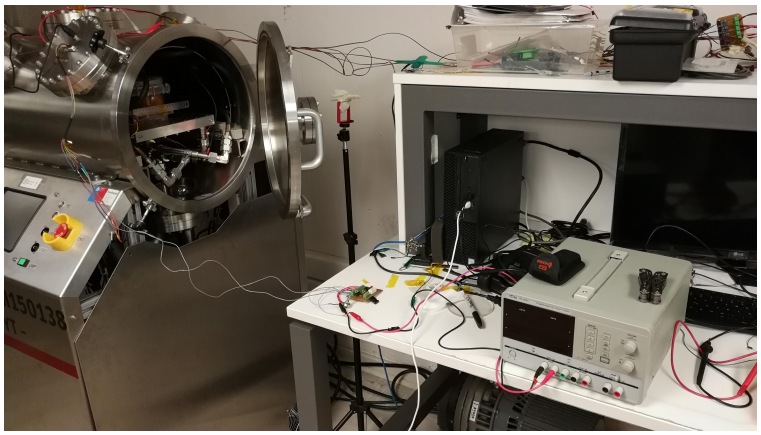

Figure 7.11: Preparation of vacuum chamber for air injector propulsion tests.

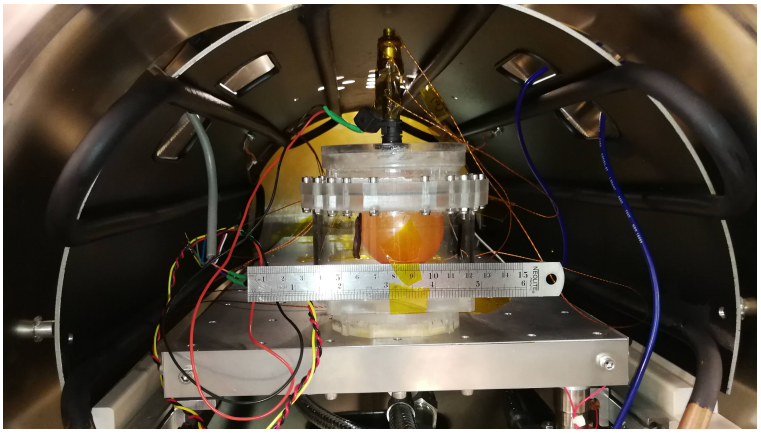

Figure 7.12: Propulsion system based on an injector in a vacuum chamber.

### 7.1.4 Preliminary Results

**Test bench** For the test under ambient pressure and liquid alcohol conditions, 12 consecutive push pulses were performed. The measurement was performed approximately every 12ms, generating thrusts every 1 minute. The duration of the discharge was 15 seconds and 45 seconds of rest. The results can be seen in Figure 7.13, where the mass measured decrease as mass is released.

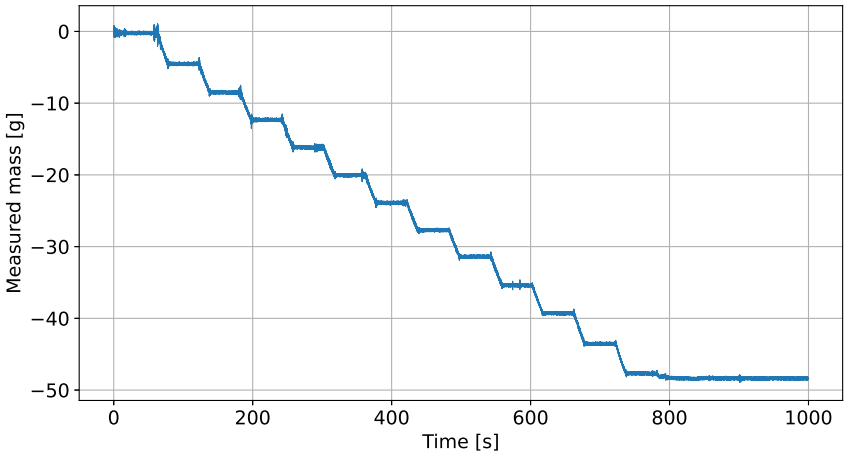


Figure 7.13: Original mass measured every 12 ms. Pushes are performed every 1 minute, with a rest window of 45 seconds, and a continuous push window of 15 seconds.

As can be seen, the signal is very sensitive to sensor noise, in addition, the initial oscillations of the system generate wave measurements of the mass as described in equations (7.2). For this reason, different levels of low-pass filters are implemented until finding a signal that does not depend in great manner on the initial oscillations, as shown in Figure 7.14. The selected cutoff frequency is 10 Hz, as it is the cleanest and does not lose track of the signal. However, it is important to note that there is more information available in the signal that can be useful in describing injector performance, but the focus of this article is more exploratory on automotive injector capabilities in micro-thrust and vacuum tests.

With the implementation of the filter and losing information of the oscillatory response of the load cell, we can eliminate the terms that depend on $y$ in the equation (7.2).

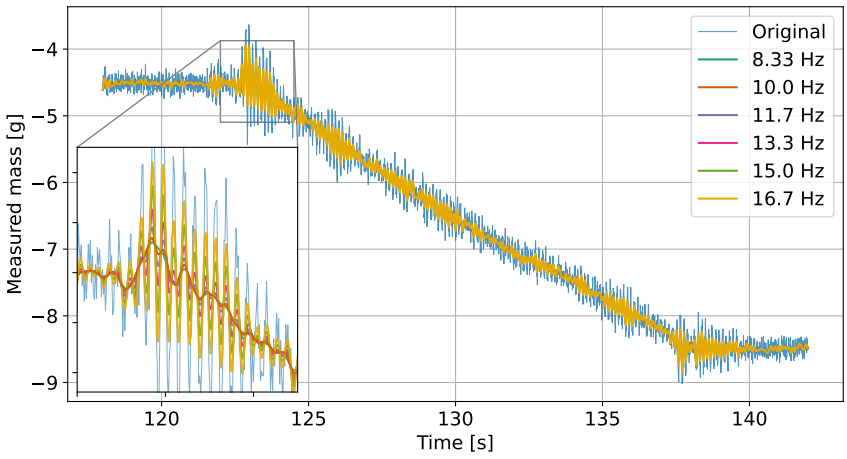


Figure 7.14: The injector is zooming in on the moment the second pulse is generated. The original mass is shown with different frequency values for a low pass filter.

**Vacuum test** For the vacuum test, the liquid alcohol was exchanged for air inside a latex balloon. In addition, the balloon is protected with a hermetic system made of acrylic to see the behavior of the balloon inside the vacuum chamber. To quantify the proper functioning of the injector under vacuum conditions, the same pressure sensor of the vacuum chamber was used, since the thrust generated by the air is imperceptible by the load cell. The results of this experiment are shown in Figure 7.15.

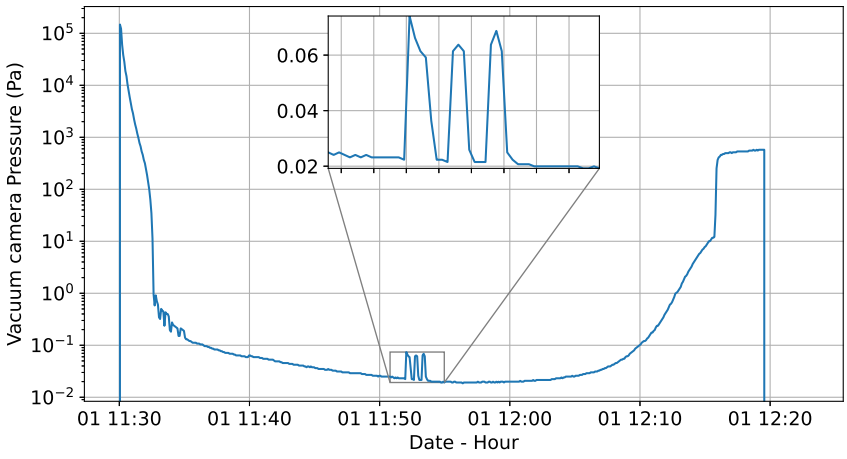


Figure 7.15: Vacuum injector test. The vacuum chamber performs ambient-internal pressure measurements every 5 seconds. The graph is displayed on a logarithmic scale to highlight three injector tests, each 20 seconds long.

In the test, small leaks were observed in the acrylic receiver, interpreted by an increase in the size of the balloon as shown in Figure 7.16. This caused the emptying of the chamber

not to reach the minimum. However, the injector and the air contained in the balloon remained stable, since three consecutive impulses could be generated.

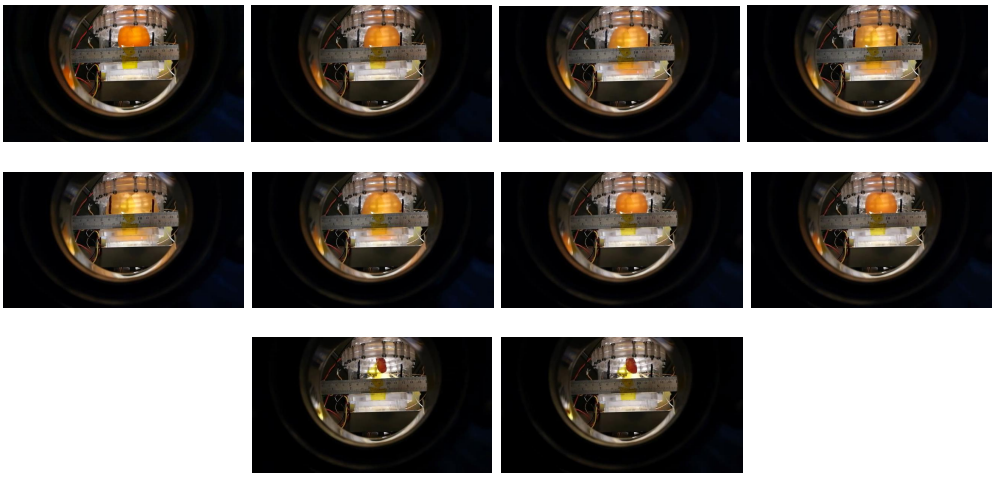

Figure 7.16: Automobile injector vacuum test. From left to right, and downwards, the presence of leaks in the acrylic container is observed as the volume of the balloon inside increases. However, the air inside the balloon remains stable and the three pulses in Figures 7.15 can be generated.

### 7.1.5 Analysis of preliminary results

**Test bench** Using the reduced equation (7.2), the mass measured by the data acquisition system can help us estimate the thrust generated by the injector. For this, the measured mass is defined as follows

$$m_m(t) = m + \dot{m} I_{sp} \qquad (with\ g_e = g). \tag{7.3}$$

Considering that the mass $m$ varies according to the mass flow as

$$m(t) = m_0 - \dot{m}t, \tag{7.4}$$

replacing equation (7.4) into (7.3), and with $m_0 = 0$ for calibraton, it results in the following expression

$$\begin{aligned} m_m(t) &= m_0 - \dot{m}t + \dot{m} I_{sp} \\ m_m(t) &= \dot{m}(I_{sp} - 1). \end{aligned} \tag{7.5}$$

Equation (7.5) is a good approximation to obtain the mass flow of the system and to find information about the approximate thrust levels. In order to incorporate the data, the 12 pulses of the test are broken down as shown in Figure 7.17. In these graphs, the slope of the mass variation in each pulse can be seen it. In addition, a red line resulting from the equation (7.5) without thrust is added and incorporated into the graph to compare the actual flows. As long as the thrust curve is above the red line, the injector will generate

thrust with positive efficiency. On the other hand, the red line is an approximation of the mass variation of each push with a duration of 15 seconds. The results of the mass flows are shown in the Table 7.2. Additionally, equation (7.5) shows that the specific impulse $I_{sp}$ is responsible for maintaining the level of thrust above the initial mass of the pulse, finding the moment in which this phenomenon is generated gives us an indication of the specific impulse as shown in Figure 7.18.

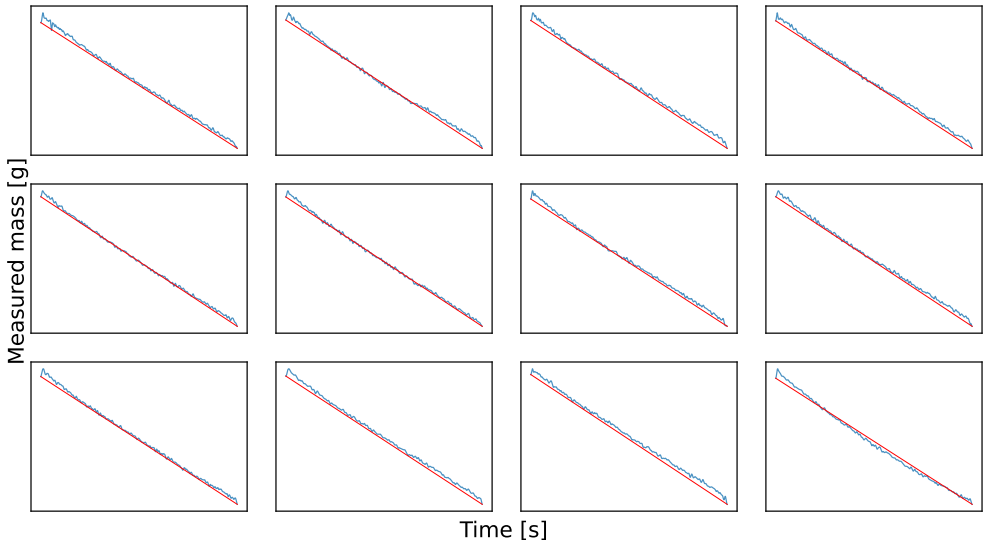


Figure 7.17: Measured mass of each pulse. The red line is an approximation of the theoretical no-thrust mass flow and is added as a visual aid to view injector efficiency.

Using the thrust definition ($T = \dot{m} I_{sp} g_e$), the maximum thrust in each peak of the pulses can be calculated as

$$T_{max} = g_e((m_m)_{max} + \dot{m}\Delta t_{max}), \tag{7.6}$$

where $(m_m)_{max}$ is the maximum mass measured, and $\Delta t_{max}$ is the time when the maximum value is reached from the pulse start. Figure 7.18 shows a close-up of the area where each peak is generated for a better understanding. The resulting mean $\Delta t_{max}$ and the mean maximum thrust are shown in Table 7.3.

Using these equations, the parameters presented in Table 7.2 can be extracted.

Table 7.2: Injector performance at ambient conditions.

| Parameters | Value |
|---|---|
| Mean mass peak | 0.230 $[g]$ |
| Standard deviation (s.t.d) of mass peaks | 0.048 $[g]$ |
| Mean specific impulse | 0.592 $[s]$ |
| Standard deviation of specific impulse | 0.101 $[s]$ |
| Mean Mass flow | 0.263 $[g/s]$ |
| Standard deviation of mass flow | 0.011 $[g/s]$ |

To calculate the exit velocity $v_e$ of the gases, the density $\rho$ of the alcohol equal to 789 $[kg/m^3]$ is considered, with 4 exit holes with a diameter equal to 0.1 $mm$. Thus, the output

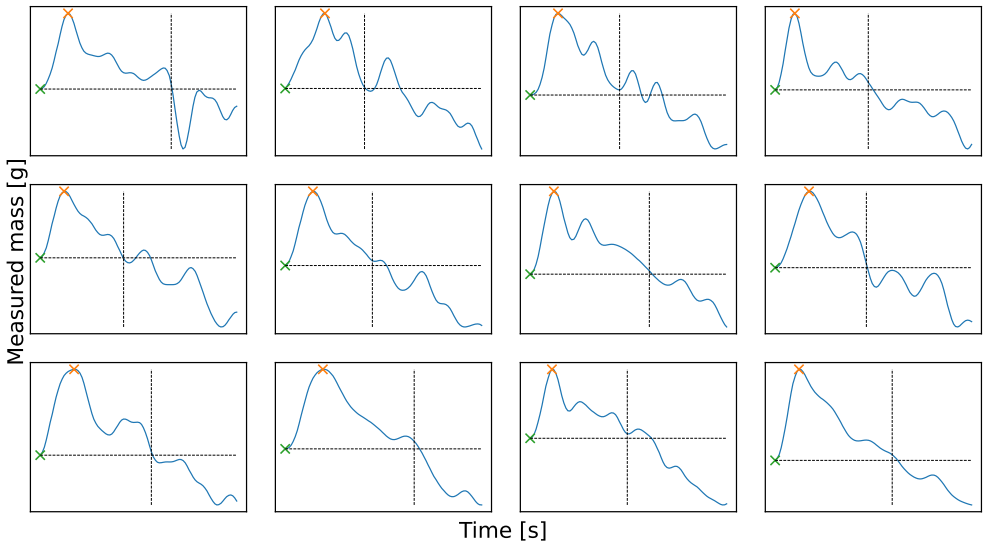


Figure 7.18: A close-up of the peaks of each thrust is shown. The green "x"'s are the starting points, and the red "x"'s are the maximum level of thrust for the signal with a 10 Hz low-pass filter. The dashed lines represent the cutoff generated by the specific impulse value.

Table 7.3: Thrust performance at ambient conditions.

| Parameters | Value |
|---|---|
| Mean $\Delta t_{max}$ | 0.161 [$s$] |
| Standard deviation of $\Delta t_{max}$ | 0.035 [$s$] |
| Mean maximum thrust | 2.681 [$mN$] |
| Standard deviation of maximum thrust | 0.482 [$mN$] |

velocity is equal to 10.616 [$m/s$] with a standard deviation of 0.449 [$m/s$]. Considering that the speed of sound in liquid media, such as alcohol, is greater than 1000 $m/s$, it can be mentioned that the injector flow was not supersonic. Then, the exit pressure is equal to ambient pressure and the internal over pressure $p_0$ of the latex balloon can be calculated according to Bernoulli as follows,

$$p_0 = \frac{1}{2}\rho v_e^2 = 44562.284\ [Pa] \quad (s.t.\text{d. } 3812.818\ [Pa]). \tag{7.7}$$

**Vacuum test** As was presented in Figure 7.15, the vacuum test highlights 3 points of interest that are shown in Figure 7.19. If the base pressure of the chamber is considered (represented by the segmented line), we can calculate the differential pressure generated by the impulses, which are summarized in Table 7.4. It is important to note that the pressures recorded by the vacuum chamber correspond to the total internal pressure, and not the gas outlet pressure from the injector. If we wanted to make an estimate of the force, we can make the following assumptions.

It is important to note that the pressures recorded by the vacuum chamber correspond to the total internal pressure, and not the gas exit pressure $p_e$ from the injector. If we wanted to make an estimate of the force, we can make the assumption that the overpressure

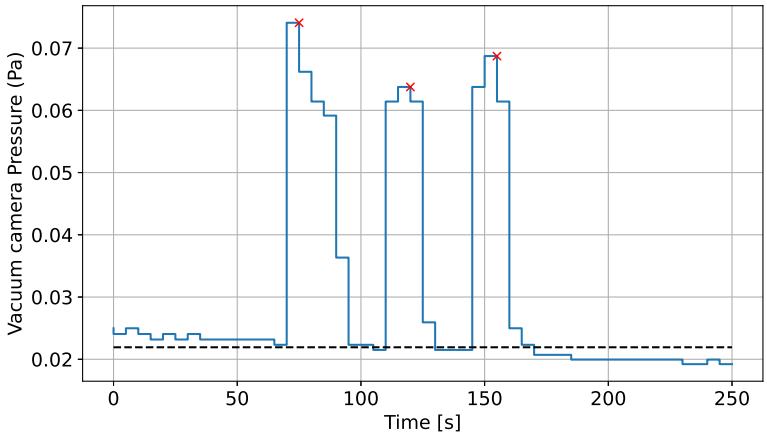


Figure 7.19: Approach to points of interest. The Figure shows the maximum pressure points measured by the chamber, and the average internal pressure, represented by the dotted line. The measured pressure difference is related to the thrust that the injector can generate.

Table 7.4: Pressure release performance at vacuum conditions.

| Parameters | Value |
|---|---|
| Mean pressure released | 46.926333 [$mPa$] |
| Standard deviation of pressure | 5.158103 [$mPa$] |

generated by the latex balloon is of a magnitude similar to that estimated by equation (7.7). Then, according to [**?**], it is known that the critical pressure $p^*$ for supersonic flow in a reservoir is defined as,

$$\frac{p^*}{p_0} = \left(\frac{2}{\gamma + 1}\right)^{\frac{\gamma}{\gamma - 1}}, \tag{7.8}$$

where $p_0$ is the reservoir pressure, and $\gamma$ is the coefficient of adiabatic expansion equal to 1.4. Assuming that the absolute reservoir pressure is equal to the atmospheric pressure added to the overpressure of the latex balloon calculated in equation (7.7), the following expression is developed,

$$p^* = (44562.284 + 101315)\left(\frac{2}{1.4 + 1}\right)^{\frac{1.4}{1.4-1}} = 77069.445. \tag{7.9}$$

Since the chamber pressure is much less than the critical pressure, we can assume that the flow is released under supersonic conditions. Then the following equations can help us estimate the thrust level,

$$p_e = p^* = p_0 \left( \frac{2}{\gamma + 1} \right)^{\frac{\gamma}{\gamma - 1}} \tag{7.10}$$

$$v_e = \sqrt{\left( \frac{2\gamma}{\gamma + 1} \right) \frac{p_0}{\rho_0}} \tag{7.11}$$

$$\dot{m} = \sqrt{\gamma p_0 \rho_0} A_e \left( \frac{2}{\gamma + 1} \right)^{\frac{\gamma+1}{2(\gamma-1)}} \tag{7.12}$$

$$F = \dot{m} v_e + (p_e - p_a) A_e, \tag{7.13}$$

where $A_e = 3.141e-5$ $[m]$, $\rho_0 = 1.225$ $[kg/m^3]$, $p_a$ is the vacuum chamber pressure, and $F$ is the estimated thrust. The result is as follows,

$$\begin{aligned} p_e &= 77069.445\ [Pa] \\ v_e &= 372.734[m/s] \\ \dot{m} &= 9.092e-3\ [kg/s] \\ F &= 5.810\ [N]. \end{aligned}$$

These preliminary data show a significant difference in the orders of magnitude of the thrusts in ambient conditions with alcohol with respect to the vacuum condition with air. This may be due to the fact that perhaps the elastic pressure generated by the latex balloon was diminished by the leaks of the acrylic container, and also due to a possible leak of the reservoir pressure $p_0$.

These last calculations raise an important requirement for future tests, where it is necessary to improve the measurement of the thrust in the vacuum chamber. However, despite the fact that the estimate is overestimated, this work presents a successful vacuum test using an automobile injector.

# Bibliography


[1] A. A. Siddiqi, *Beyond Earth: a chronicle of deep space exploration, 1958-2016*, second edition ed., ser. NASA SP. Washington, DC: National Aeronautics and Space Administration, Office of Communications, NASA History Division, 2018, no. 2018-4041.

[2] D. Kajon, F. Masson, T. Wagner, and D. Welberg, "Development of an Attitude Control and Propellant Settling System for the aA5ME Upper Stage," *In Proceedings of the Space Propulsion Conference, Cologne, Germany*, no. 19–22, p. 9, May 2014.

[3] F. Maggi, A. Bandera, L. Galfetti, L. T. De Luca, and T. L. Jackson, "Efficient solid rocket propulsion for access to space," *Acta Astronautica*, vol. 66, no. 11-12, pp. 1563–1573, Jun. 2010. [Online]. Available: https://linkinghub.elsevier.com/retrieve/pii/S0094576509004986

[4] A. Okninski, "Solid rocket propulsion technology for de-orbiting spacecraft," *Chinese Journal of Aeronautics*, vol. 35, no. 3, pp. 128–154, 2022. [Online]. Available: https://www.sciencedirect.com/science/article/pii/S1000936121003319

[5] H. Burkhardt, M. Sippel, G. Krülle, R. Janovsky, M. Kassebom, H. Lübberstedt, O. Romberg, and B. Fritsche, "Evaluation of propulsion systems for satellite end-of-life de-orbiting," in *38th AIAA/ASME/SAE/ASEE Joint Propulsion Conference & Exhibit*, 2002, p. 4208.

[6] D. G. Chavers, "NASA Lander Technologies Project Status," in *AIAA SPACE 2016*. Long Beach, California: American Institute of Aeronautics and Astronautics, Sep. 2016. [Online]. Available: http://arc.aiaa.org/doi/10.2514/6.2016-5221

[7] A. J. Spear, "Low cost approach to Mars Pathfinder and small landers," *Acta Astronautica*, vol. 35, pp. 345–354, 1995. [Online]. Available: https://linkinghub.elsevier.com/retrieve/pii/0094576594002006

[8] D. W. Way, R. W. Powell, A. Chen, A. D. Steltzner, A. M. S. Martin, P. D. Burkhart, and G. F. Mendeck, "Mars Science Laboratory: Entry, Descent, and Landing System Performance," in *2007 IEEE Aerospace Conference*, Mar. 2007, pp. 1–19, iSSN: 1095-323X.

[9] "ESA - Exploration of the Moon - ESA Strategy for Science at the Moon." (Date accessed: 2024-05-08). [Online]. Available: https://exploration.esa.int/s/WmMyaoW

[10] "NASA's lunar exploration program overview." (Date accessed: 2024-05-08). [Online]. Available: https://www.nasa.gov/sites/default/files/atoms/files/artemis_plan-20200921.pdf

[11] G. Jamanca-Lino, "Space Resources Engineering: Ilmenite Deposits for Oxygen Production on the Moon," *American Journal of Mining and Metallurgy*, vol. 6, no. 1, pp. 6–11, Jan. 2022, number: 1 Publisher: Science and Education Publishing. [Online]. Available: http://pubs.sciepub.com/ajmm/6/1/2/index.html

[12] A. Johnstone, "Cubesat design specification." (Date accessed: 2024-05-08). [Online]. Available: https://www.cubesat.org/cubesatinfo

[13] E. Obreque and M. Díaz, "An Effort to Use a Solid Propellant Engine Arrangement in the Moon Soft Landing Problem," *Aerospace*, vol. 9, no. 10, p. 540, Oct. 2022, number: 10 Publisher: Multidisciplinary Digital Publishing Institute. [Online]. Available: https://www.mdpi.com/2226-4310/9/10/540

[14] Z. Sun, Y. Jia, and H. Zhang, "Technological advancements and promotion roles of Chang'e-3 lunar probe mission," *Science China Technological Sciences*, vol. 56, no. 11, pp. 2702–2708, Nov. 2013. [Online]. Available: http://link.springer.com/10.1007/s11431-013-5377-0

[15] Q. Wang and J. Liu, "A Chang'e-4 mission concept and vision of future Chinese lunar exploration activities," *Acta Astronautica*, vol. 127, pp. 678–683, Oct. 2016. [Online]. Available: http://www.sciencedirect.com/science/article/pii/S0094576515302770

[16] M. Leslie, "A Chinese Lander Explores the Far Side of the Moon," *Engineering*, vol. 5, no. 4, pp. 598–599, Aug. 2019. [Online]. Available: http://www.sciencedirect.com/science/article/pii/S2095809919307830

[17] J. Liu, X. Ren, W. Yan, C. Li, H. Zhang, Y. Jia, X. Zeng, W. Chen, X. Gao, D. Liu, X. Tan, X. Zhang, T. Ni, H. Zhang, W. Zuo, Y. Su, and W. Wen, "Descent trajectory reconstruction and landing site positioning of Chang'E-4 on the lunar farside," *Nature Communications*, vol. 10, no. 1, p. 4229, Sep. 2019, number: 1 Publisher: Nature Publishing Group. [Online]. Available: https://www.nature.com/articles/s41467-019-12278-3

[18] Y. Zheng, M. Yang, X. Deng, S. Jin, J. Peng, Y. Su, Z. Gu, L. Chen, Y. Pang, and N. Zhang, "Analysis of Chang'e-5 lunar core drilling process," *Chinese Journal of Aeronautics*, Feb. 2022. [Online]. Available: https://www.sciencedirect.com/science/article/pii/S1000936122000231

[19] M. V. Djachkova, M. L. Litvak, I. G. Mitrofanov, and A. B. Sanin, "Selection of Luna-25 landing sites in the South Polar Region of the Moon," *Solar System Research*, vol. 51, no. 3, pp. 185–195, May 2017. [Online]. Available: https://doi.org/10.1134/S0038094617030029

[20] G. Fujii, K. Kawatsu, Y. Daimon, K. Michigami, K. Kushiki, S. Sawai, and S. Sakai, "Verification of the Transient Behavior of the SLIM Propulsion

System (Smart Lander for Investigating Moon)," in *AIAA Propulsion and Energy 2021 Forum*. American Institute of Aeronautics and Astronautics, _eprint: https://arc.aiaa.org/doi/pdf/10.2514/6.2021-3582. [Online]. Available: https://arc.aiaa.org/doi/abs/10.2514/6.2021-3582

[21] A. Lee, T. Ely, R. Sostaric, A. Strahan, J. Riedel, M. Ingham, J. Wincentsen, and S. Sarani, "Preliminary Design of the Guidance, Navigation, and Control System of The Altair Lunar Lander," in *AIAA Guidance, Navigation, and Control Conference*. American Institute of Aeronautics and Astronautics, Aug. 2010. [Online]. Available: https://arc.aiaa.org/doi/10.2514/6.2010-7717

[22] R. D. Braun and R. M. Manning, "Mars Exploration Entry, Descent, and Landing Challenges," *Journal of Spacecraft and Rockets*, pp. 310–323, 2007.

[23] H. Zhang, J. Li, Z. Wang, and Y. Guan, "Guidance Navigation and Control for Chang'E-5 Powered Descent," *Space: Science & Technology*, vol. 2021, pp. 1–15, Jul. 2021. [Online]. Available: https://spj.sciencemag.org/journals/space/2021/9823609/

[24] P. V. Kazmerchuk and A. E. Shirshakov, "The Luna-25 Spacecraft: Return to the Moon," *Solar System Research*, vol. 55, no. 6, pp. 496–508, Nov. 2021. [Online]. Available: https://doi.org/10.1134/S0038094621060058

[25] A. P. Tallaksen, A. D. Horchler, C. Boirum, D. Arnett, H. L. Jones, E. Fang, E. Amoroso, L. Chomas, L. Papincak, O. B. Sapunkov, and W. L. Whittaker, "CubeRovers for Lunar Exploration," vol. 2041, p. 5060, Oct. 2017, conference Name: 2017 Annual Meeting of the Lunar Exploration Analysis Group. [Online]. Available: http://adsabs.harvard.edu/abs/2017LPICo2041.5060T

[26] H. Kalita and J. Thangavelautham, "Lunar CubeSat Lander to Explore Mare Tranquilitatis pit," in *AIAA Scitech 2020 Forum*. American Institute of Aeronautics and Astronautics, Jan. 2020. [Online]. Available: https://arc.aiaa.org/doi/10.2514/6.2020-2163

[27] A. Dinardi and M. Persson, "High Performance Green Propulsion (HPGP): A Flight-Proven Capability and Cost Game-Changer for Small and Secondary Satellites," *Small Satellite Conference*, Aug. 2012. [Online]. Available: https://digitalcommons.usu.edu/smallsat/2012/all2012/27

[28] H. Kalita, A. Gholap, and J. Thangavelautham, "Dynamics and Control of a Hopping Robot for Extreme Environment Exploration on the Moon and Mars," *IEEE Aerospace Conference Proceedings*, Dec. 2019.

[29] T. Hashimoto, T. Yamada, M. Otsuki, T. Yoshimitsu, A. Tomiki, W. Torii, H. Toyota, J. Kikuchi, N. Morishita, Y. Kobayashi, T. Ito, H. Tanno, A. Nagamatsu, and H. Morimoto, "Nano Semihard Moon Lander: OMOTENASHI," *IEEE Aerospace and Electronic Systems Magazine*, vol. 34, no. 9, pp. 20–30, Sep. 2019. [Online]. Available: https://ieeexplore.ieee.org/document/8826664/

[30] R. Whitley, D. Davis, L. Burke, B. McCarthy, R. Power, M. McGuire, and

K. Howell, *Earth-Moon Near Rectilinear Halo and Butterfly Orbits for Lunar Surface Exploration*, ser. AAS/AIAA Astrodynamics Specialist Conference, Aug. 2018. [Online]. Available: https://engineering.purdue.edu/people/kathleen.howell.1/Publications/Conferences/2018_AAS_WhiDavBurMcCPowMcGHow.pdf

[31] J. Deca, A. Divin, C. Lue, T. Ahmadi, and M. Horányi, "Reiner Gamma albedo features reproduced by modeling solar wind standoff," *Communications Physics*, vol. 1, no. 1, pp. 1–8, Apr. 2018, number: 1 Publisher: Nature Publishing Group. [Online]. Available: https://www.nature.com/articles/s42005-018-0012-9

[32] D. C. Morrisey, "Historical perspective - Viking Mars Lander propulsion," *Journal of Propulsion and Power*, vol. 8, no. 2, pp. 320–331, Mar. 1992. [Online]. Available: https://arc.aiaa.org/doi/10.2514/3.23481

[33] G. A. Soffen and C. W. Snyder, "The First Viking Mission to Mars," *Science*, vol. 193, no. 4255, pp. 759–766, Aug. 1976, publisher: American Association for the Advancement of Science Section: Reports. [Online]. Available: https://science.sciencemag.org/content/193/4255/759

[34] K. Kondo, S. Tanaka, H. Habu, S. Tokudome, K. Hori, H. Saito, A. Itoh, M. Watanabe, and M. Esashi, "Vacuum test of a micro-solid propellant rocket array thruster," *IEICE Electronic Express*, vol. 1, pp. 222–227, Jan. 2004.

[35] K. Zhang, S. Chou, and S. Ang, "Development of a solid propellant microthruster with chamber and nozzle etched on a wafer surface," *Journal of Micromechanics and Microengineering*, vol. 14, pp. 785–792, Jun. 2004.

[36] S. Tanaka, K. Kondo, H. Habu, A. Itoh, M. Watanabe, K. Hori, and M. Esashi, "B/TI multilayer reactive igniter for micro solid rocket array thruster," in *2007 IEEE 20th International Conference on Micro Electro Mechanical Systems (MEMS)*, Jan. 2007, pp. 887–890, iSSN: 1084-6999.

[37] J. Meditch, "On the problem of optimal thrust programming for a lunar soft landing," *IEEE Transactions on Automatic Control*, vol. 9, no. 4, pp. 477–484, Oct. 1964, conference Name: IEEE Transactions on Automatic Control.

[38] W. Fleming and R. Rishel, *Deterministic and Stochastic Optimal Control*. New York, NY: Springer New York, 1975. [Online]. Available: http://link.springer.com/10.1007/978-1-4612-6380-7

[39] B. Acikmese and S. R. Ploen, "Convex Programming Approach to Powered Descent Guidance for Mars Landing," *Journal of Guidance, Control, and Dynamics*, vol. 30, no. 5, pp. 1353–1366, Sep. 2007. [Online]. Available: https://arc.aiaa.org/doi/10.2514/1.27553

[40] B. Xu, J. Sun, S. Li, and T. Cao, "Finite time sliding sector control for spacecraft atmospheric entry guidance," *Acta Astronautica*, Dec. 2018. [Online]. Available: http://www.sciencedirect.com/science/article/pii/S009457651831316X

[41] J. Zhang, J. D. Biggs, D. Ye, and Z. Sun, "Finite-time attitude set-

point tracking for thrust-vectoring spacecraft rendezvous," *Aerospace Science and Technology*, vol. 96, p. 105588, Jan. 2020. [Online]. Available: https://www.sciencedirect.com/science/article/pii/S1270963819319571

[42] X.-L. Liu, G.-R. Duan, and K.-L. Teo, "Optimal soft landing control for moon lander," *Automatica*, vol. 44, no. 4, pp. 1097–1103, Apr. 2008. [Online]. Available: http://www.sciencedirect.com/science/article/pii/S0005109807004025

[43] Z. Honghua, G. Yifeng, C. Ming, J. Li, P. Yu, Z. Xiaowen, W. Huaqiang, Y. Wei, W. Zhiwen, J. Yu, and W. Zeguo, "Guidance navigation and control for Chang'E-4 lander," *Scientia Sinica Technologica*, vol. 49, no. 12, pp. 1418–1428, 2019.

[44] H.-H. Zhang, J. Li, Y.-F. Guan, and X.-Y. Huang, "Autonomous navigation for powered descent phase of Chang'E-3 lunar lander," *Kongzhi Lilun Yu Yingyong/Control Theory and Applications*, vol. 31, pp. 1686–1694, Dec. 2014.

[45] C. Sánchez-Sánchez and D. Izzo, "Real-Time Optimal Control via Deep Neural Networks: Study on Landing Problems," *Journal of Guidance, Control, and Dynamics*, vol. 41, no. 5, pp. 1122–1135, 2018, publisher: American Institute of Aeronautics and Astronautics _eprint: https://doi.org/10.2514/1.G002357. [Online]. Available: https://doi.org/10.2514/1.G002357

[46] H. Rom, "Thrust Control of Hydrazine Rocket Motors by Means of Pulse Width Modulation," *Acta Astronautica*, vol. 26, pp. 313–316, 1992.

[47] X. Zhang, K. V. Ling, Z. Lu, X. Zhang, W. Liao, and W. S. Lim, "Piece-wise affine MPC-based attitude control for a CubeSat during orbital manoeuvres," *Aerospace Science and Technology*, vol. 118, p. 106997, Nov. 2021. [Online]. Available: https://www.sciencedirect.com/science/article/pii/S1270963821005071

[48] A. R. Klumpp, "Apollo lunar descent guidance," *Automatica*, vol. 10, no. 2, pp. 133–146, Mar. 1974. [Online]. Available: https://www.sciencedirect.com/science/article/pii/0005109874900193

[49] O. Omidvar and D. Elliott, *Neural Systems for Control*. Elsevier Science, 1997. [Online]. Available: https://books.google.cl/books?id=oLcAiySCow0C

[50] M. T. Hagan, H. B. Demuth, and O. D. Jesús, "An introduction to the use of neural networks in control systems," *International Journal of Robust and Nonlinear Control*, vol. 12, no. 11, pp. 959–985, 2002, _eprint: https://onlinelibrary.wiley.com/doi/pdf/10.1002/rnc.727. [Online]. Available: https://onlinelibrary.wiley.com/doi/abs/10.1002/rnc.727

[51] D. P. Mishra, *Fundamentals of Rocket Propulsion*. CRC Press, Jul. 2017. [Online]. Available: https://www.taylorfrancis.com/books/9781315175997

[52] M. A. Willcox, M. Q. Brewster, K. C. Tang, D. S. Stewart, and I. Kuznetsov, "Solid Rocket Motor Internal Ballistics Simulation Using Three-Dimensional Grain Burnback," *Journal of Propulsion and Power*, vol. 23, no. 3, pp. 575–584, May 2007.

[Online]. Available: https://arc.aiaa.org/doi/10.2514/1.22971

[53] P. M. Sforza, "Chapter 12 - solid propellant rocket motors," in *Theory of Aerospace Propulsion*, second edition ed., ser. Aerospace Engineering, P. M. Sforza, Ed. Butterworth-Heinemann, 2017, pp. 617–668. [Online]. Available: https://www.sciencedirect.com/science/article/pii/B9780128093269000129

[54] S. Brunton and J. Kutz, *Data-Driven Science and Engineering: Machine Learning, Dynamical Systems, and Control*. Cambridge University Press, 2019. [Online]. Available: https://books.google.cl/books?id=CYaEDwAAQBAJ

[55] M. Cerf, "Optimal injection point for launch trajectories with parametric thrust profile," *Acta Astronautica*, vol. 151, pp. 752–760, Oct. 2018. [Online]. Available: http://www.sciencedirect.com/science/article/pii/S0094576518305745

[56] J. Z. Ben-Asher, "Optimal control theory with aerospace applications," 2010. [Online]. Available: https://api.semanticscholar.org/CorpusID:60320370

[57] J. M. Longuski, J. J. Guzmán, and J. E. Prussing, *Optimal Control with Aerospace Applications*. New York, NY: Springer New York, 2014. [Online]. Available: https://link.springer.com/10.1007/978-1-4614-8945-0

[58] S. Yin, J. Wu, and P. Song, "Optimal control by deep learning techniques and its applications on epidemic models," *Journal of Mathematical Biology*, vol. 86, no. 3, p. 36, Jan. 2023. [Online]. Available: https://doi.org/10.1007/s00285-023-01873-0

[59] M. Vavrina and K. Howell, "Global low-thrust trajectory optimization through hybridization of a genetic algorithm and a direct method," in *AIAA/AAS Astrodynamics Specialist Conference and Exhibit*, 2008. [Online]. Available: https://arc.aiaa.org/doi/abs/10.2514/6.2008-6614

[60] M. Pikuliński and P. Malczyk, "Adjoint method for optimal control of multibody systems in the hamiltonian setting," *Mechanism and Machine Theory*, vol. 166, p. 104473, 2021. [Online]. Available: https://www.sciencedirect.com/science/article/pii/S0094114X21002317

[61] R. Bellman, "Dynamic programming," *Science*, vol. 153, no. 3731, pp. 34–37, 1966.

[62] H. Kaufman, "The mathematical theory of optimal processes, by l. s. pontryagin, v. g. boltyanskii, r. v. gamkrelidze, and e. f. mishchenko. authorized translation from the russian. translator: K. n. trirogoff, editor: L.. w. neustadt. interscience publishers (division of john wiley and sons, inc. , new york) 1962. viii 360 pages." *Canadian Mathematical Bulletin*, vol. 7, no. 3, p. 500–500, 1964.

[63] D. G. Hull, *Optimal Control Theory for Applications*, ser. Mechanical Engineering Series, F. F. Ling, Ed. New York, NY: Springer New York, 2003. [Online]. Available: http://link.springer.com/10.1007/978-1-4757-4180-3

[64] M. Hestenes, *Calculus of Variations and Optimal Control Theory*, ser. Applied

mathematics series. Wiley, 1966. [Online]. Available: https://books.google.cl/books?id=aQ5RAAAAMAAJ

[65] C. Marrison and R. Stengel, "Robust control system design using random search and genetic algorithms," *IEEE Transactions on Automatic Control*, vol. 42, no. 6, pp. 835–839, Jun. 1997.

[66] A. Herreros, E. Baeyens, and J. R. Perán, "MRCD: a genetic algorithm for multiobjective robust control design," *Engineering Applications of Artificial Intelligence*, vol. 15, no. 3, pp. 285–301, Jun. 2002. [Online]. Available: https://www.sciencedirect.com/science/article/pii/S0952197602000362

[67] Y. Gao, J. Wang, S. Gao, and Y. Cheng, "An Integrated Robust Design and Robust Control Strategy Using the Genetic Algorithm," *IEEE Transactions on Industrial Informatics*, vol. 17, no. 12, pp. 8378–8386, Dec. 2021.

[68] I. Sekaj, "Genetic Algorithm Based Controller Design," *IFAC Proceedings Volumes*, vol. 36, no. 18, pp. 125–128, Sep. 2003. [Online]. Available: https://www.sciencedirect.com/science/article/pii/S1474667017346566

[69] V. Kachitvichyanukul, "Comparison of Three Evolutionary Algorithms: GA, PSO, and DE," *Industrial Engineering and Management Systems*, vol. 11, no. 3, pp. 215–223, 2012, publisher: Korean Institute of Industrial Engineers. [Online]. Available: http://www.koreascience.or.kr/article/JAKO201229664764585.page

[70] T. A. Khan, S. H. Ling, and A. S. Mohan, "Advanced particle swarm optimization algorithm with improved velocity update strategy," in *2018 IEEE International Conference on Systems, Man, and Cybernetics (SMC)*, 2018, pp. 3944–3949.

[71] X. Zhu and H. Wang, "A new inertia weight control strategy for particle swarm optimization," *AIP Conference Proceedings*, vol. 1955, no. 1, p. 040095, 04 2018. [Online]. Available: https://doi.org/10.1063/1.5033759

[72] L. Blackmore, "Autonomous precision landing of space rockets," *The Bridge, National Academy of Engineering*, vol. 46, no. 4, pp. 15–20, Jan. 2016. [Online]. Available: https://www.nae.edu/File.aspx?id=164381

[73] S. Li, X. Jiang, and T. Tao, "Guidance Summary and Assessment of the Chang'e-3 Powered Descent and Landing," *Journal of Spacecraft and Rockets*, vol. 53, Nov. 2015.

[74] G. P. Sutton, *Rocket Propulsion Elements, Ninth Edition*. John Wiley & Sons (US), 2017, google-Books-ID: gS9gswEACAAJ.

[75] A. Reilley, "OpenMotor, GitHub Repository." (Date accessed: 2022-06-30), Jun. 2022. [Online]. Available: https://github.com/reilleya/openMotor

[76] C. Cheng, R. Wei, and F. Bao, "An Efficient Method for Non-uniform Solid Rocket Motor Grain Burnback Simulation," in *2020 11th International Conference on Mechanical and Aerospace Engineering (ICMAE)*, Jul. 2020, pp. 63–67.

[77] V. Carrara and H. K. Kuga, "Torque and Speed Control Loops of a Reaction Wheel." (Date accessed: 2024-05-08), 2013, p. 10. [Online]. Available: https://icoev.org/proceedings2013/661_paper0.pdf

[78] J. R. Wertz, Ed., *Spacecraft Attitude Determination and Control*, ser. Astrophysics and Space Science Library. Dordrecht: Springer Netherlands, 1978, vol. 73. [Online]. Available: http://link.springer.com/10.1007/978-94-009-9907-7

[79] L. Blackmore, B. Açikmeşe, and D. P. Scharf, "Minimum-Landing-Error Powered-Descent Guidance for Mars Landing Using Convex Optimization," *Journal of Guidance, Control, and Dynamics*, vol. 33, no. 4, pp. 1161–1171, Jul. 2010. [Online]. Available: https://arc.aiaa.org/doi/10.2514/1.47202

[80] J. Z. Ben-Asher, *Optimal control theory with aerospace applications*, ser. AIAA education series. Reston, VA: American Institute of Aeronautics and Astronautics, 2010, oCLC: ocn459208376.

[81] M. Jamshidi, R. A. Krohling, L. d. S. Coelho, and P. J. Fleming, *Robust Control Systems with Genetic Algorithms*. Boca Raton: CRC Press, Jan. 2017.

[82] S. D. Stein, "Benefits of the Star Grain Configuration for a Sounding Rocket," p. 11.

[83] Y. Inatani and H. Habu, "SS-520 Nano Satellite Launcher and its Flight Result," *Proceedings of the AIAA/USU Conference on Small Satellites, SSC18-IX-03*, p. 6. [Online]. Available: https://digitalcommons.usu.edu/cgi/viewcontent.cgi?article=4120&context=smallsat

[84] N. Wingborg, "GRAIL: Green Solid Propellants for Launchers," p. 9 pages, 2017, artwork Size: 9 pages Medium: PDF Publisher: Proceedings of the 7th European Conference for Aeronautics and Space Sciences. Milano, Italy, 3-6 july 2017. [Online]. Available: https://www.eucass.eu/doi/EUCASS2017-560.pdf

[85] G. d. Silva, S. C. Rufino, and K. Iha, "Green Propellants: Oxidizers," *Journal of Aerospace Technology and Management*, vol. 5, pp. 139–144, Jun. 2013, publisher: Departamento de Ciência e Tecnologia Aeroespacial. [Online]. Available: http://www.scielo.br/j/jatm/a/mKwbtgCb5nCkDQxLCTwrkVj/abstract/?lang=en

[86] Y. Zhang, Y. Guo, G. Ma, and B. Wie, "Fixed-time pinpoint mars landing using two sliding-surface autonomous guidance," *Acta Astronautica*, vol. 159, pp. 547–563, Jun. 2019. [Online]. Available: http://www.sciencedirect.com/science/article/pii/S0094576517304496

[87] K. Kosanovich, A. Gurumoorthy, E. Sinzinger, and M. Piovoso, "Improving the extrapolation capability of neural networks," in *Proceedings of the 1996 IEEE International Symposium on Intelligent Control*, Sep. 1996, pp. 390–395, iSSN: 2158-9860.

[88] M. Werner, A. Junginger, P. Hennig, and G. Martius, "Uncertainty in equation learning," in *Proceedings of the Genetic and Evolutionary Computation Conference Companion*. Boston Massachusetts: ACM, Jul. 2022, pp. 2298–2305. [Online].

Available: https://dl.acm.org/doi/10.1145/3520304.3533964

[89] Y. K. Adde, Alemayehu, G. Lulseged, Y. Adde, L. Alemayehu, and G. Solomon, "Design of a solid rocket propulsion system," *International Journal of Aeronautical Science and Aerospace Research*, pp. 224–229, 07 2020.

[90] M. B. Çelik, B. Ozdalyan, M. B. Çelik, and B. Ozdalyan, "Gasoline Direct Injection," in *Fuel Injection*. IntechOpen, Aug. 2010. [Online]. Available: https://www.intechopen.com/chapters/11336

# Annex: Extended results

## Entry simulation

Optimization results at the entry stage. Point P1 corresponds to the ignition point. P2 is the diameter in centimeters (constant). P3 is the length of the motor (constant).

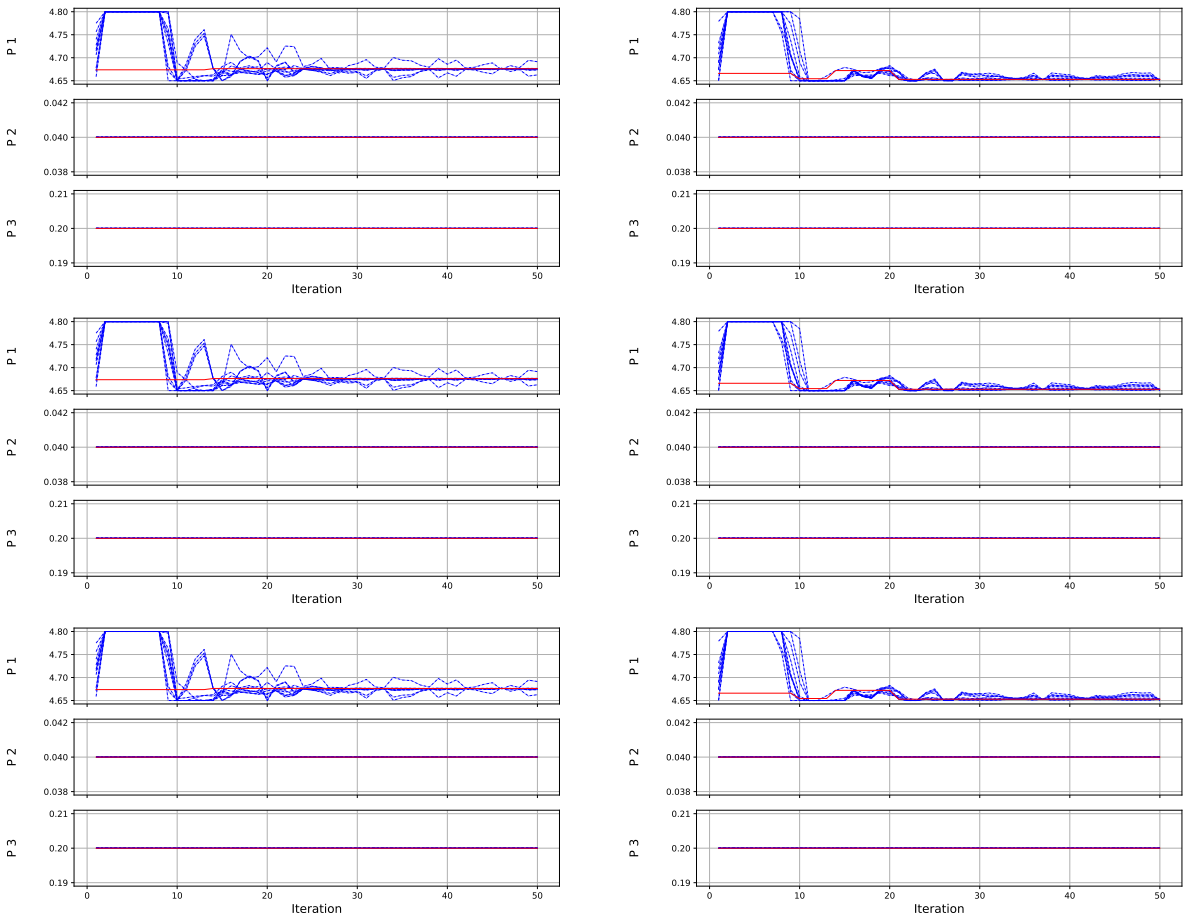


Figure A1: Solution of the optimization problem of the equation (5.7). The blue lines show the positions of each particle in the algorithm and the red line is the global best solution. Part 1/2.

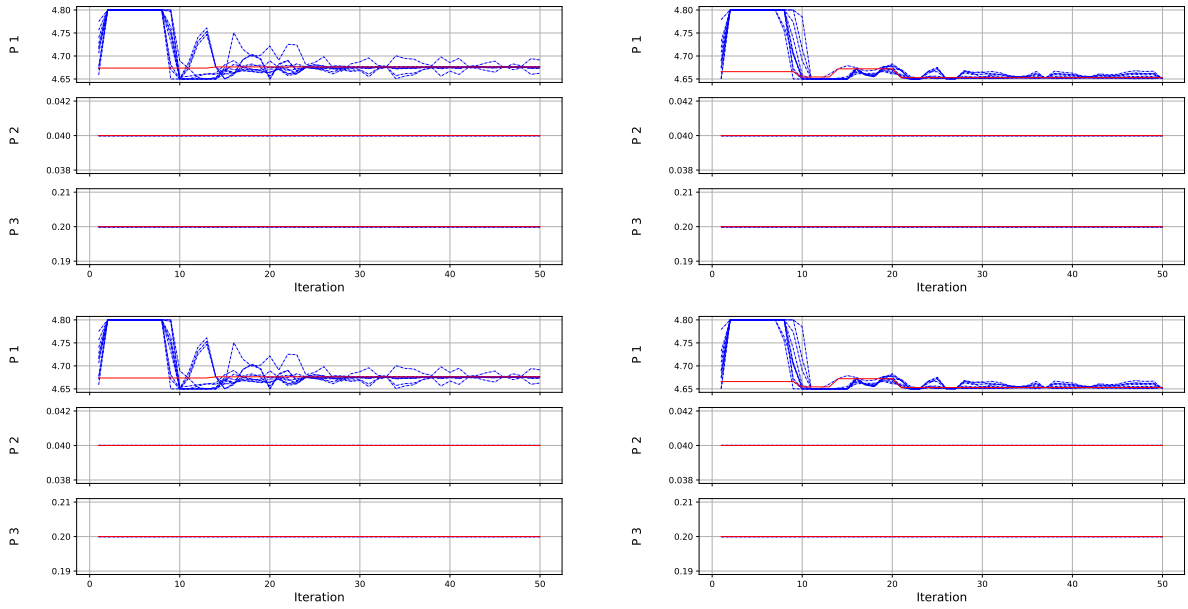


Figure A2: Solution of the optimization problem of the equation (5.7). The blue lines show the positions of each particle in the algorithm and the red line is the global best solution. Part 2/2.

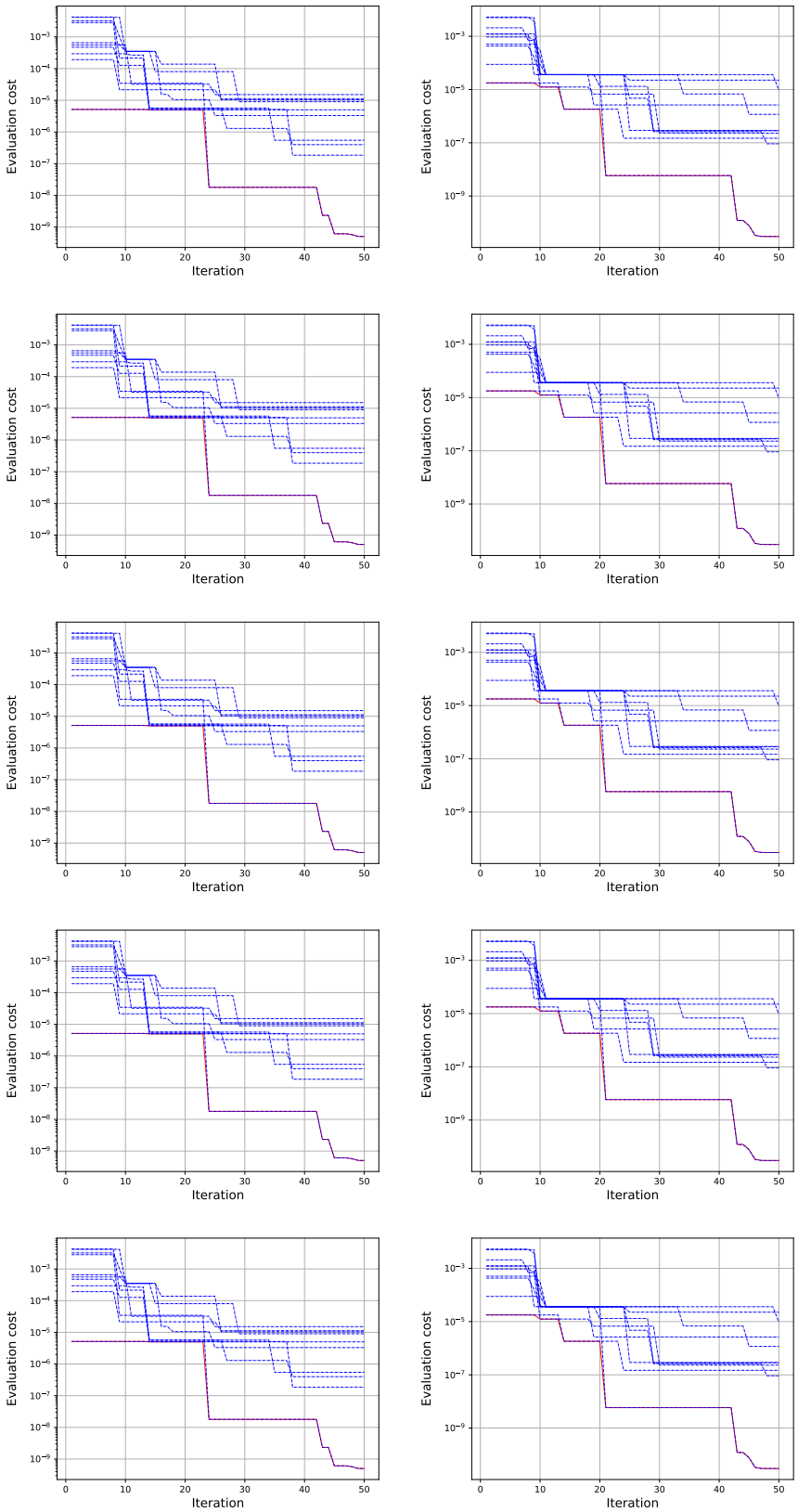


Figure A3: Evaluation of the cost function of the optimization problem of the equation (5.7). The blue lines show the individual evaluation of each particle and the red linear is the best cost evaluation.

**Entry simulation: Torque**

*Torque due to mounting angle error:*

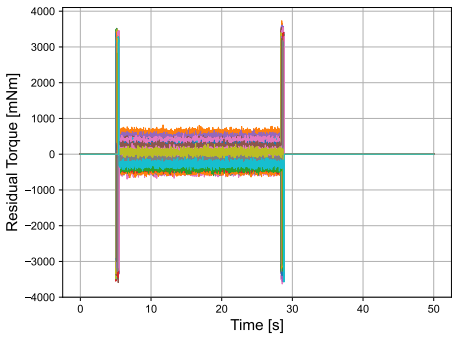


Figure A4: Torque due to mounting angle error

*Torque due to mounting position error:*

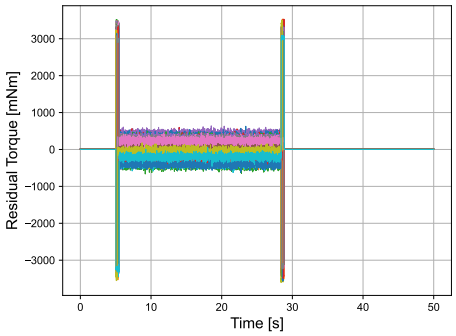


Figure A5: Torque due to mounting position error

*Torque due to dead time:*

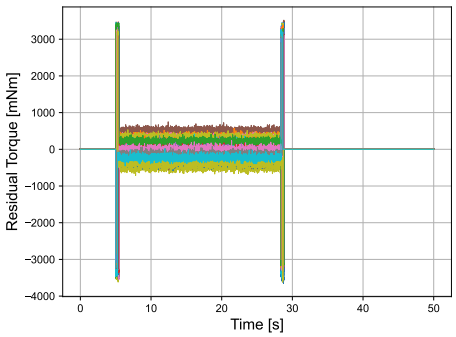


Figure A6: Torque due to dead time

*Torque due to $I_{sp}$ bias:*

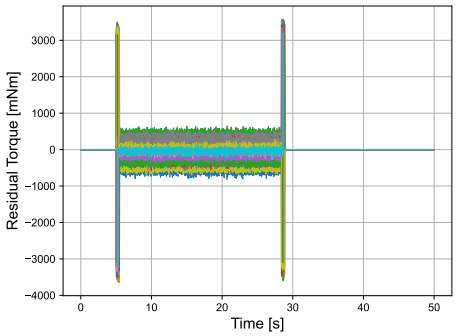


Figure A7: Torque due to $I_{sp}$ bias

*Torque due to $I_{sp}$ noise:*

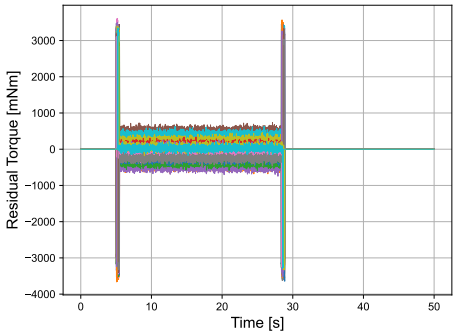


Figure A8: Torque due to $I_{sp}$ noise

*Torque due to all:*

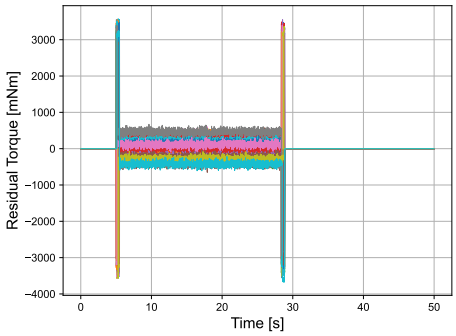


Figure A9: Torque due to all uncertainties

# Entry and Descent simulation

Optimization results at the entry and descent stage with $K_n$. Point P1 corresponds to the ignition point. P2 is the diameter in centimeters. P3 is the length of the motor. P4 is the $K_n$ ratio.

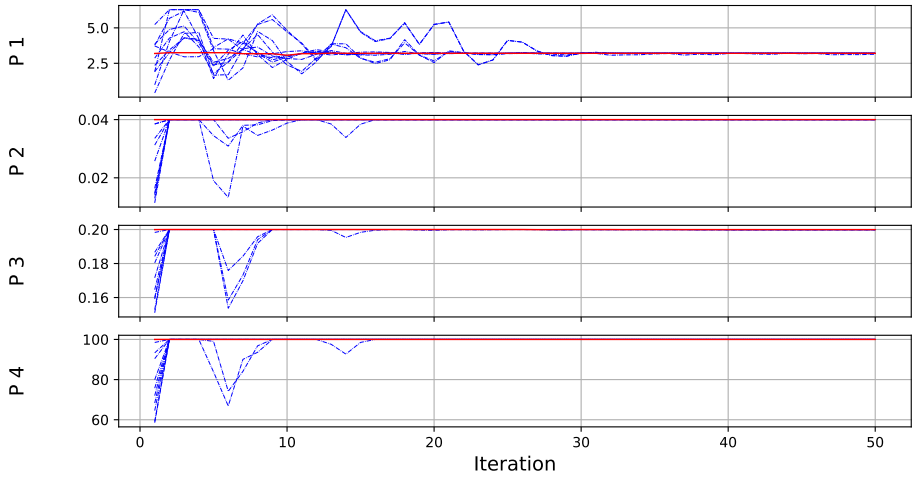


Figure A10: Solution of the optimization problem of the equation (5.7) with $K_n$. The blue lines show the positions of each particle in the algorithm and the red line is the global best solution.

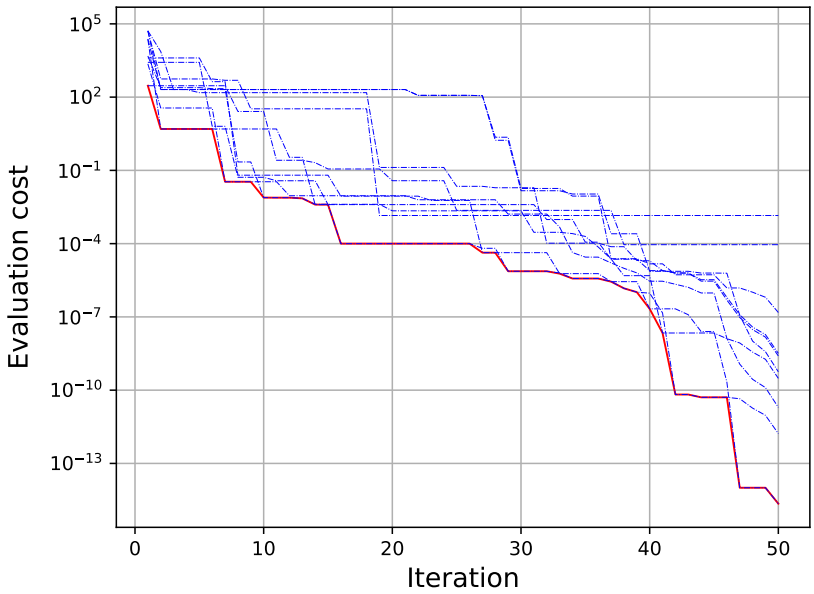


Figure A11: Evaluation of the cost function of the optimization problem of the equation (5.7) with $K_n$. The blue lines show the positions of each particle in the algorithm and the red line is the global best solution.

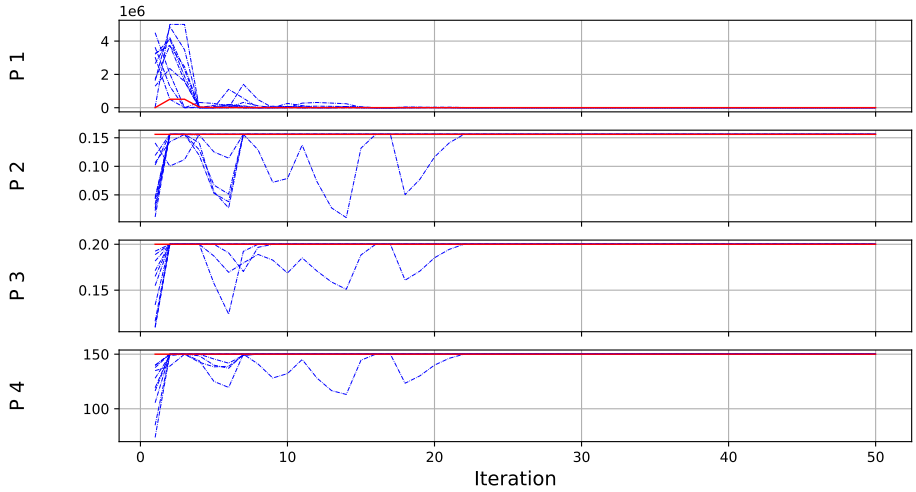


Figure A12: Solution of the optimization problem of the equation (5.9) with $K_n$. The blue lines show the positions of each particle in the algorithm and the red line is the global best solution.

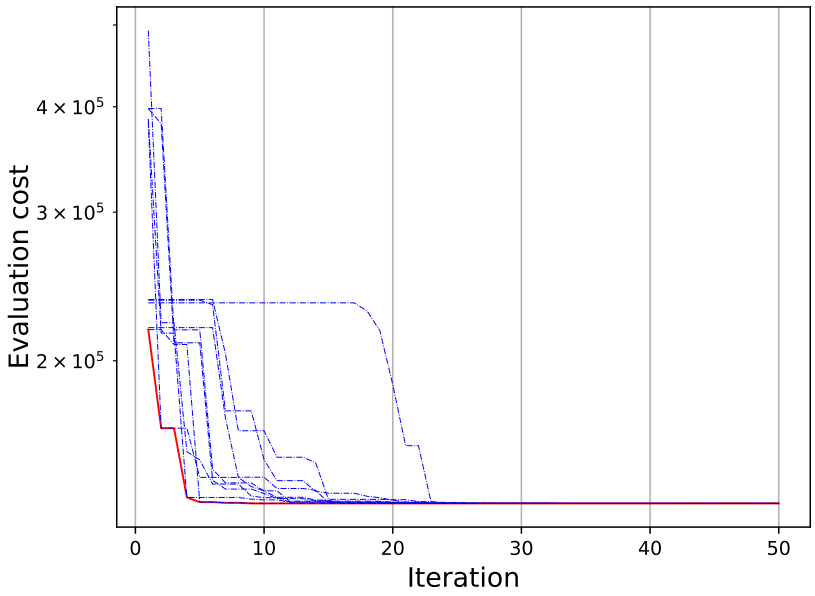


Figure A13: Evaluation of the cost function of the optimization problem of the equation (5.9) with $K_n$. The blue lines show the positions of each particle in the algorithm and the red line is the global best solution.